

6-19-2012

Exploring Thermal and Mechanical Properties of Selected Transition Elements under Extreme Conditions: Experiments at High Pressures and High Temperatures

Rostislav Hrubik

Florida International University, rhrub001@fiu.edu

DOI: 10.25148/etd.FI12080619

Follow this and additional works at: <https://digitalcommons.fiu.edu/etd>

Recommended Citation

Hrubik, Rostislav, "Exploring Thermal and Mechanical Properties of Selected Transition Elements under Extreme Conditions: Experiments at High Pressures and High Temperatures" (2012). *FIU Electronic Theses and Dissertations*. 696.
<https://digitalcommons.fiu.edu/etd/696>

This work is brought to you for free and open access by the University Graduate School at FIU Digital Commons. It has been accepted for inclusion in FIU Electronic Theses and Dissertations by an authorized administrator of FIU Digital Commons. For more information, please contact dcc@fiu.edu.

FLORIDA INTERNATIONAL UNIVERSITY

Miami, Florida

EXPLORING THERMAL AND MECHANICAL PROPERTIES OF
SELECTED TRANSITION ELEMENTS UNDER EXTREME CONDITIONS:
EXPERIMENTS AT HIGH PRESSURES AND HIGH TEMPERATURES

A dissertation submitted in partial fulfillment of the

requirements for the degree of

DOCTOR OF PHILOSOPHY

in

MATERIALS SCIENCE AND ENGINEERING

by

Rostislav Hrubciak

2012

To: Dean Amir Mirmiran
College of Engineering and Computing

This dissertation, written by Rostislav Hrubciak, and entitled Exploring thermal and mechanical properties of selected elements and compounds under extreme conditions: Experiments at high pressures and high temperatures having been approved in respect to style and intellectual content, is referred to you for judgment.

We have read this dissertation and recommend that it be approved.

Jiuhua G. Chen

Kinzy Jones

Gautam Sen

Guoyin Shen

Surendra K. Saxena, Major Professor

Date of Defense: June 19, 2012

The dissertation of Rostislav Hrubciak is approved.

Dean Amir Mirmiran
College of Arts and Sciences

Dean Lakshmi N. Reddi
University Graduate School

Florida International University, 2012

© Copyright 2012 by Rostislav Hrubíak

All rights reserved.

DEDICATION

I dedicate this thesis to my teachers.

ACKNOWLEDGMENTS

I wish to thank the members of my committee for their support and patience.

ABSTRACT OF THE DISSERTATION

EXPLORING THERMAL AND MECHANICAL PROPERTIES OF
SELECTED TRANSITION ELEMENTS UNDER EXTREME CONDITIONS:
EXPERIMENTS AT HIGH PRESSURES AND HIGH TEMPERATURES

by

Rostislav Hrubíak

Florida International University, 2012

Miami, Florida

Professor Surendra K. Saxena, Major Professor

Transition metals (Ti, Zr, Hf, Mo, W, V, Nb, Ta, Pd, Pt, Cu, Ag, and Au) are essential building units of many materials and have important industrial applications. Therefore, it is important to understand their thermal and physical behavior when they are subjected to extreme conditions of pressure and temperature. This dissertation presents:

- An improved experimental technique to use lasers for the measurement of thermal conductivity of materials under conditions of very high pressure (P , up to 50 GPa) and temperature (T up to 2500 K).
- An experimental study of the phase relationship and physical properties of selected transition metals, which revealed new and unexpected physical effects of thermal conductivity in Zr, and Hf under high P - T .
- New phase diagrams created for Hf, Ti and Zr from experimental data.
- P - T dependence of the lattice parameters in α -hafnium. Contrary to prior reports, the α - ω phase transition in hafnium has a negative dT/dP slope.

- New data on thermodynamic and physical properties of several transition metals and their respective high P - T phase diagrams.
- First complete thermodynamic database for solid phases of 13 common transition metals was created. This database has:
 - All the thermochemical data on these elements in their standard state (mostly available and compiled).
 - All the equations of state (EoS) formulated from pressure-volume-temperature data (measured as a part of this study and from literature).
 - Complete thermodynamic data for selected elements from standard to extreme conditions.

The thermodynamic database provided by this study can be used with available thermodynamic software to calculate all thermophysical properties and phase diagrams at high P - T conditions. For readers who do not have access to this software, tabulated values of all thermodynamic and volume data for the 13 metals at high P - T are included in the APPENDIX. In the APPENDIX, a description of several other high-pressure studies of selected oxide systems is also included.

Thermophysical properties (C_p , H , S , G) of the high P - T ω -phase of Ti, Zr and Hf were determined during the optimization of the EoS parameters and are presented in this study for the first time. These results should have important implications in understanding hexagonal-close-packed to simple-hexagonal phase transitions in transition metals and other materials.

TABLE OF CONTENTS

CHAPTER	PAGE
INTRODUCTION	1
1. Thermodynamically consistent EoS and phase diagrams of selected metals at extreme conditions	4
1.01 Introduction.....	5
1.02 High P - T phase transitions and P - V - T equation of state of α -hafnium: Synchrotron X-ray diffraction study	12
1.03 Thermodynamically consistent EoS and phase diagrams of Ti, Zr and Hf....	32
1.04 Thermodynamics of several elements at high pressure	56
2. Exploring thermal conductivity of metals at extreme conditions.....	76
2.01 Introduction.....	77
2.02 Experimental methods and system design.....	95
2.03 Measuring heat flow and mapping phase transitions in Hf at high P - T	112
2.04 Thermal conductivity of Zr at high pressure and temperature.....	120
CONCLUSION.....	130
APPENDICES	133
LIST OF REFERENCES.....	181
VITA	203

LIST OF FIGURES

FIGURE	PAGE
1.1. Basic principle of the diamond anvil cell	14
1.2. Schematic of Mao-Bell type DAC pressing system	15
1.3. Diagram of a laser heated diamond anvil cel.....	16
1.4. Schematic of sample foil loading in a DAC	16
1.5. Sample loaded into a DAC	17
1.6. Ruby fluorescence shift vs. pressure.....	18
1.7. P - T range surveyed in APS run 1	21
1.8. c/a ratio of α -hafnium (hcp) unit cell.....	23
1.9. 2-D x-ray diffraction patterns of Hf in several P - T regimes.....	24
1.10. Integrated x-ray diffraction patterns of Hf in several P - T regimes.....	25
1.11. P - V relation of α -phase hafnium at room temperature	26
1.12. Heat capacity of α -phase hafnium as functions of temperature.....	28
1.13. P - V - T EoS molar volume calculation errors	29
1.14. Comparison of literature reported data on thermal expansion of Hf.	29
1.15. Group IVB transition metals, γ_0 and δ_0	30
1.16. Schematic phase diagram of Zr and Hf at high P - T	34
1.17. Geometries for the diamond-cell x-ray experiments.	36
1.18. Resistive heating in a DAC.....	38
1.19. Platinum pressure measurement validation	40
1.20. Integrated intensity vs. 2θ plots.	41
1.21. Volume measurements for α -Hf at high P - T	43

1.22. Observed volume thermal expansion in Hf.	45
1.23. Pre vs. post heating molar volume of hafnium.	49
1.24. Calculated phase diagrams.....	52
1.25. <i>c/a</i> ratio.	54
1.26. Calculated volume and bulk modulus from this work for V, Nb, and Ta.....	60
1.27. Calculated volume and bulk modulus for Mo and W.....	60
1.28. Calculated cold compression and Hugoniot curves for V, Nb, and Ta.....	61
1.29. Calculated cold compression and Hugoniot curves for Mo and W.....	62
1.30. Calculated isotherm for various elements.....	62
1.31. Comparison of calculated isotherms of Mo.....	63
1.32. Calculated and experimental volume and bulk modulus for Pd and Pt.....	67
1.33. Calculated cold compression and Hugoniot curves for Pd and Pt.....	68
1.34. Comparison of Calculated isotherms of Cu, Au, Pt.....	69
1.35. Calculated volume and bulk modulus for Cu, Ag, and Au.....	71
1.36. Calculated cold compression and Hugoniot curves for Cu, Ag, and Au.....	72
2.1. Finite-element calculation.....	83
2.2. Modeling geometry for LH-DAC heat flow calculations.....	84
2.3. Modeling heat transport in LH-DAC in 2-D with axial symmetry.....	85
2.4. Typical calculated temperature distribution in a LH-DAC.....	87
2.5. Effect of thermal conductivity on heat flow in LH-DAC.....	91
2.6. Comparison of calculated temperature gradients for Pt and Zr.....	92
2.7. Calculated power vs. temperature.....	93
2.8. Laser heating system in CeSMEC, schematic.....	98

2.9. Laser-heating system UI	99
2.10. Plank equation fitting.....	102
2.11. Accuracy of temperature measurement	103
2.12. Temperature vs. Laser power plateau	105
2.13. Uncertainties in radiometric temperature measurement	106
2.14. High pressure melting curve of Fe.....	107
2.15. Reverse side temperature measurement.....	110
2.16. Temperature vs. laser power.....	116
2.17. P - T map of laser heating features in hafnium.....	118
2.18. Side-by-side sample DAC loading schematic.....	122
2.19. Temperature gradients vs. laser power	123
2.20. Time resolved visual comparison of heat distribution.....	125
2.21. Measuring the width of the temperature profiles	126
2.22. Heating platinum and zirconium in different insulation media.....	127
2.23. Measured temperature gradients for Pt and Zr.....	129
2.24. Numerical model fit.....	129
A-I.1. Diffraction patterns and indexing of CaVO_3 and SrVO_3	141
A-I.2. Rietveld refinement of SrVO_3	142
A-I.3. Compression of SrVO_3 and CaVO_3	143
A-II.1. SEM picture of ZnO nanopowder after SPVD process	149
A-II.2. Normalized ambient-pressure luminescence spectra of ZnO	152
A-II.3. X-Ray diffraction for ZnO bulk crystal as a function of pressure	153
A-II.4. The pressure dependence of the volume for ZnO	154

A-II.5. Normalized PL spectra of ZnO as a function of pressure at $T = 11$ K	158
A-II.6. Pressure dependencies of PL for ZnO samples at $T = 11$ K	159

LIST OF TABLES

TABLE	PAGE
1.1. Structures and high pressure phase transitions of several transition metals	8
1.2. EoS parameters for α -Hf	27
1.3. $B_0, B_0', \gamma_0 \delta_0$ parameters of Group IVB transition metals.....	30
1.4. EoS parameters for the thirteen transition elements.	75
2.1. Heat flow equations	86
2.2. Variable thermal transport variables	88
2.3. Temperature measurement calibration.....	103
A-I.1. Structures of SrVO ₃ and CaVO ₃	138
A-II.2. Structures of SrVO ₃ and CaVO ₃ , theoretical calculation.....	140
A-II.1. B_0, B_0' and V_0 for bulk and nanopowder ZnO at 298K.....	155
A-III.1. Tables of thermophysical properties: Group IVB transition metals	162

LIST OF SYMBOLS

d	distance between lattice planes
hkl	Miller indices
B_0	isothermal bulk modulus at ambient conditions
B_0'	pressure derivative of B_0
P	pressure
T	temperature
V	volume
V_0	volume at ambient conditions
ρ	density
ρ_0	density at ambient conditions
γ	Grüneisen parameter
δ	Anderson-Grüneisen parameter
θ	x-ray scattering angle
θ_D	Debye temperature
λ	wavelength
k	thermal conductivity
D	thermal diffusivity
hcp	hexagonally-close-packed
bcc	body-centered-cubic
fcc	face-centered-cubic
ω	simple hexagonal structure, Space Group: P6/mmm

INTRODUCTION

There are two parts of this dissertation. Part I includes a description of an experimental investigation of high-pressure/high-temperature phase diagram and thermal equation of state (*EoS*) for Group IVB metals using the diamond anvil cell (DAC) and *in situ* synchrotron x-ray diffraction. These transition metals are essential building units of many materials and have important industrial applications. Therefore, it is important to understand their thermal and physical behavior when they are subjected to extreme conditions of pressure and temperature. Interest in transition metals at extreme conditions, especially hafnium, has resurged recently because of its use in rods to control fission reactions in nuclear power stations around the world. Part I describes a study to measure volumes (*V*) and map phase transitions of Group IVB transition metals at simultaneous high-pressure and high-temperature to obtain a *P-V-T EoS* for each of their high-pressure/high-temperature phases. This part also describes a comparison of high-pressure and high-temperature properties of Group IVB transition metals to those of several other transition metals, for which high-pressure and high-temperature experimental data has been extensively collected from existing literature.

Part II of this dissertation contains a description of the development and application of laser-heating methods for diamond anvil cell (DAC) for the measurement of heat transport properties of transition metals at very high pressures and temperatures. The DAC laser-heating system has an improved ability to measure two-dimensional temperature distributions across laser-heated samples with a very high spatial resolution. Measured temperature profiles were combined with a finite element (*FE*) heat flow

model to inversely calculate heat transport properties of the specimens under examination.

There are two appendices given. APPENDIX I contains the description of a high pressure study of two transition metal oxides (CaVO_3 and SrVO_3) which normally crystalize in the ABO_3 perovskite structure. These well-known structures exhibit many interesting properties with a large range of industrial applications. Perovskites can be widely applied because depending on their electronic structure, they can be dielectric, ferroelectric, semiconducting, superconducting (Yamanaka, 2004), and among other qualities, can have excellent oxygen ion mobility at elevated temperatures (Hsu et al., 2006). Crystal structure which gives rise to the great variety of physical properties of perovskites can change with pressure, temperature and chemical composition. Phase transitions in perovskite associated with change of pressure are still a subject of investigation. In APPENDIX I, there is a description of a study of structure and phase stability of CaVO_3 and SrVO_3 perovskites neither of which has been previously studied under high pressure.

In APPENDIX II, the application of high-pressure experiments to study zinc oxide compound which has gained substantial interest in recent years is described. ZnO is an attractive material for future developments in optoelectronic, spintronic, and sensor applications. The structural properties of ZnO crystals under hydrostatic pressure have been studied for many years (H. Liu et al. 2005; Karzel et al. 1996; Gerward and J.S. Olsen 1995; Desgreniers 1998; Recio et al. 1998; Decremps, J. Zhang, and Liebermann 2000; Decremps et al. 2003; Mori et al. 2004; Ahuja et al. 1998; J.E. Jaffe and A.C. Hess 1993; John E Jaffe et al. 2000). Established values of bulk moduli for both phases are

quite scattered and vary from about 135 GPa to about 180 GPa for wurtzite phase and from 132 to about 230 GPa for rocksalt phase. One of the possible reasons for such large scattering of the values of bulk moduli could be associated with the quality of the sample material. Appendix II contains a comparison of the elastic properties under high hydrostatic pressure of very high quality bulk ZnO crystals with those of ZnO nanocrystals.

1. Thermodynamically consistent EoS and phase diagrams of selected metals
at extreme conditions

1.01 Introduction

Elements are essential building units of all substances. It is quite important to understand their thermal and mechanical behavior when they are subjected to extreme conditions. A thermodynamic database was created for 13 common transition metals which has:

- The thermochemical data on these elements in their standard state (mostly available and compiled)
- The equations of state (EoS) formulated pressure-volume-temperature data (some from literature, others measured in study)
- Thermodynamic data for selected elements from standard to extreme conditions
- Phase diagrams from thermodynamic equilibrium calculations consistent with experiments

There are not many examples of obtaining complete thermodynamic data for high P - T systems in literature. A most recent example is the work on iron of Komabayashi and Fei (Komabayashi and Fei, 2010).

Thermodynamic treatment: CALPHAD method

To construct the phase diagram thermodynamically one needs to retrieve the thermodynamic data on each of the phases from the experimental equilibrium data in the system one is studying. To calculate this diagram from equilibrium thermodynamics, one would need the Gibbs free energy as a function of pressure on each of the possible phases. Moreover, to perform useful thermodynamic calculations at high P - T one needs not only the phase boundaries but also the volume data as a function of P and T , which can be obtained by X-ray diffraction.

Gibbs energy at high P and T of each phase has two components. First is the Gibbs energy at 1 bar and T to be obtained from thermochemical data tables, which do exist for most elements (except for phases that may exist stably only at high pressures e.g. the *hcp* Fe, ω -Ti, Zr, Hf, etc.) and the second the Gibbs energy component of the pressure part which is to be obtained from an EoS (Equation of State) determined from PVT measurements. To perform thermodynamic calculations at extreme high pressures and high temperatures (Fabrichnaya et al., 2004), it is necessary to fit the available experimental data to consistent thermodynamic models. The CALPHAD (Lukas et al., 2007) methodology has been very successful in coupling of thermochemistry and phase equilibria in multicomponent systems at ambient pressure. However, up to now there have been only a few attempts to include pressure effects on condensed phases in CALPHAD calculations (Fried and M., 2000; Brosh et al., 2007). Ideally using the so-called “explicit Gibbs free energy EoS” (Fried and M., 2000) which is the formulation of the Gibbs free energy directly as a function of temperature and pressure instead of separate volumetric databases, would be the best solution. The explicit Gibbs free energy formalism can be extended to high pressure and written as:

$$G(P, T) = G(P_0, T) + \int_{P_0}^P V(P', T) dP' \quad \text{EQ. 1-1}$$

where $G(P_0, T)$ is function of the temperature dependence of Gibbs free energy along the reference isobar (usually 1 atm). It should be noted that $G(P_0, T)$ is not a simple tabulation of experimental data anymore, since it is necessary to extrapolate beyond the measured range for many calculations (Brosh et al., 2008)

$$\text{The calculation of the integral in } G(P, T) = G(P_0, T) + \int_{P_0}^P V(P', T) dP' \quad \text{EQ.}$$

1-1 requires an EoS to describe the relationships among thermodynamic variables of the system. Birch–Murnaghan EoS (Guillermot and Fernandez Guillermot, 1985; Vinet et al., 1986; Saxena and Zhang, 1990; Saxena, 1996) Vinet EoS (Vinet et al., 1989) and the Jacobs–Oonk EoS (Jacobs et al., 2000; Lu, Selleb, et al., 2005) are some EoS used in CALPHAD. However, up to now their application at high pressures may be considered unsuccessful, because the existing models often give manifestly wrong predictions of high-pressure thermophysical properties. For example, negative heat capacities at high pressure are calculated for MgO and iron (Lu, Selleb, et al., 2005).

Mie–Grüneisen EoS is one of the widely used solutions to incorporate the high pressure behavior in the CALPHAD to calculate the integral in $G(P, T) = G(P_0, T) + \int_{P_0}^P V(P', T) dP'$ EQ. 1-1 (Anderson, 1995; Stixrude and Lithgow-Bertelloni, 2005; Sha and Cohen, 2010). In the SGTE database (Scientific Group Thermodynamic Europe) reappearance of solid phases above melting temperature is avoided by decreasing the heat capacity of the solid and ultimately it converges to a fixed value. But above the melting point of solid, which is beyond the experimental measurable range, extrapolation is uncontrolled and it can never be compared with experimental results (Vinet et al., 1989). Since there is no standard theoretical approach to constructing such an approximation, it is inherently problematic and the results are inconsistent. Thus, simultaneous use of CALPHAD modeling with Mie–Grüneisen (MG) equation always leads to unphysical predictions of negative isobaric heat capacity at high pressures. It is shown (Brosh et al., 2007) that at high-pressure, the quasi-harmonic model together with

the MG EoS exhibits physically acceptable behavior, much better than the unphysical prediction that was obtained when the MG EoS is used together with the SGTE database.

Brosh et. al. (Brosh et al., 2005, 2007, 2008, 2009) proposed a new formulation for incorporation of high pressure in CALPHAD terminology and replaced the Birch - Murnaghan EoS by Mie–Grüneisen. I describe their model briefly in the following sections and use it to study the high pressure behavior of the 14 elements from the group IB, VB, VIB and VIIIB of the periodic table.

Table 1.1. Summary of structures and high pressure phase transitions of several transition metals

	Structure at 1 atm, 298 K	high pressure phase transitions at 298 K
Group IVB		
	Ti <i>hcp</i>	to omega at 9 GPa; to distorted <i>bcc</i> at 116 GPa
	Zr <i>hcp</i>	to omega at 4 GPa; to <i>bcc</i> at 33 GPa
	Hf <i>hcp</i>	to omega at 45 GPa (only at non-hydrostatic conditions); to <i>bcc</i> at 57 GPa
Group VB		
	V <i>bcc</i>	to rhombohedral at 65 GPa
	Nb <i>bcc</i>	<i>bcc</i> stable up to 134 GPa
	Ta <i>bcc</i>	<i>bcc</i> stable up to 170 GPa
Group VIB		
	Cr <i>bcc</i>	
	Mo <i>bcc</i>	<i>bcc</i> stable up to 416 GPa
	W <i>bcc</i>	<i>bcc</i> stable up to at least 378 GPa (predicted stable up to 1250 GPa)
Group VIIIB		
	Pt <i>fcc</i>	stable to very high pressure
	Pd <i>fcc</i>	stable to very high pressure
Group IB		
	Cu <i>fcc</i>	Stable at high pressure, at least 100 GPa
	Ag <i>fcc</i>	Stable at high pressure, at least 100 GPa
	Au <i>fcc</i>	Stable at high pressure, predicted stable to at least 240 GPa - 2 TPa

While this type of work has been the object of major research in metallurgical and other industries, no such efforts have been made to create a thermodynamic database on elements except for some elements such as iron which is needed to estimate properties of Earth's core.

Most elements have been researched thoroughly for the phase transitions from a pressure of 1 bar to extreme pressures at 298.15 K (McMahon & Nelmes, 2006; Degtyareva, 2010) but the high temperature-high pressure volume data are rare.

EoS formulation

For the convenience of processing thermodynamic data and because of the incompatibility of the Mie-Gruneisen EoS with the heat capacity formulation in the metallurgical database [see (Brosh et al., 2007) discussion], I use the approach as outlined below.

The EoS was first proposed by Brosh et al. (2007) and has been used by Karbasi et al. and Hrubciak et al. (2011; 2012) to obtain thermodynamically consistent P - V - T equations of state for several metals. In this formulation, volume should be written as the sum of the cold compression volume and the thermal volume. In this way the Gibbs free energy in the desired state of temperature and pressure can be written based on the addition of Gibbs free energy associated with integration of cold compression from the reference pressure to the extreme pressure, then the isobaric integration of the heat capacity up to the desired temperature and finally, by integrating backwards over pressure at the desired temperature, to attain the target thermodynamic state. The total Gibbs free energy can be written as:

$$G(T, P) = G_c(P) + G^{OH}(T, P) - [G^{OH}(T, P_0) - G(T, P_0)] \cdot I(P) \quad \text{EQ. 1-2}$$

where the first term is the increase of Gibbs free energy due to cold compression from P_0 to P and is determined by molar volume (V_0), the bulk modulus (B_0), and its first pressure derivative (B_0'), taken at zero pressure and at the reference temperature of 300 K. G^{OH} is the increase of Gibbs free energy due to integration of the heat capacity at very high pressure and can be written as:

$$G^{OH}(T,P) = 3NRT \cdot \ln \left[1 - \exp \left(-\frac{\theta(P)}{T} \right) \right], \quad \text{EQ. 1-3}$$

where N is the number of atoms per unit of molecular formula and θ is the pressure dependent Einstein temperature and can be written as:

$$\theta = \theta_0 \cdot \exp \left\{ \frac{\gamma_0}{1 + \delta_0} \left[\Gamma_2(b_0, X_2^T) - \Gamma_2(b_0, 1) \right] \right\}, \quad \text{EQ. 1-4}$$

while $\Gamma_2(b_0, X_2^T) - \Gamma_2(b_0, 1) = \frac{1 + \delta_0}{B_0} \int_0^P (X_2^T)^3 dP'$ and

$$X_2^T = \left[1 - \frac{1}{3b_0 - 1} + \frac{1}{3b_0 - 1} \cdot \left(1 + \frac{2}{3} \frac{3b_0 - 1}{1 + \delta_0} \frac{P}{B_0} \right)^{\frac{1}{2}} \right]^{-1}.$$

θ_0 , γ_0 and δ_0 model parameters are Einstein temperature, Grüneisen parameter and Anderson-Grüneisen parameter respectively. b_0 is the EoS adjustable parameter and usually is 1. The last term in EQ. 1-2 accounts for the backward integration. $I(P)$ is a monotonically decreasing and dimensionless interpolation function with the limiting values $I(0)=1$ and $I(\infty)=0$, and expressed as:

$$I(P) = \frac{1}{1 + b_1} \cdot \left\{ b_1 + \left[1 + 2 \cdot b_1 \cdot \left(1 + \delta_1 \right) \frac{P}{B_0} \right]^{\frac{1}{2}} \right\} \cdot \exp \left\{ \frac{1}{b_1} - \frac{1}{b_1} \left[1 + 2 \cdot b_1 \cdot \left(1 + \delta_1 \right) \frac{P}{B_0} \right]^{\frac{1}{2}} \right\} \quad \text{EQ. 1-5}$$

where δ_1 and b_1 are additional adjustable parameters of the EoS. The total value of thermal volume is the sum of V^{QH} , the change of volume due to isobaric expansion, and

interpolation volume due to change of Gibbs free energy expressed in the square-bracketed term of EQ. 1-3.

1.02 High P-T phase transitions and P-V-T equation of state of α -hafnium: Synchrotron X-ray diffraction study

I measured the volume of hafnium at several pressures up to 67 GPa and at temperatures between 300 to 780 K. using a resistively heated diamond anvil cell (DAC) with synchrotron X-Ray diffraction at the Advanced Photon Source. The measured data allows us to determine the P - V - T equation of state (EoS) of hafnium. The previously described (Xia et al., 1990) phase transition from hcp (α) to simple hexagonal (ω) phase at 38 GPa at room temperature was not observed even up to 51GPa. The ω phase was only observed at elevated temperatures. Our measurements have also improved the experimental constraint on the high P - T phase boundary between the ω phase and high pressure bcc (β) phase of hafnium. Isothermal room temperature bulk modulus and its pressure derivative for the α -phase of hafnium were measured to be $B_0 = 112.9 \pm 0.5$ GPa and $B_0' = 3.29 \pm 0.05$ respectively. P - V - T data for the α -phase of hafnium was used to obtain a fit to a thermodynamic P - V - T equation of state based on model by Brosh et al. (2007)

Introduction

Hafnium has a hexagonal-close packed (α -phase) structure typical of Group IV transition metals (Ti, Zr). At ambient pressure (P), hafnium transforms from a room-temperature α to a body-centered cubic (β -phase) structure at temperatures (T) above 2030 K. Upon increasing the pressure at room-temperature, hafnium is reported to undergo a sequence of $\alpha \rightarrow \omega$ (simple hexagonal) $\rightarrow \beta$ phase transitions, which is also typical of other group IV metals (Xia et al., 1990). Although it is generally considered

that hafnium would follow the general α - ω - β high P - T phase diagram consistent with many other metals with *hcp* structure at ambient P - T conditions (Xia et al., 1990; Joshi et al., 2002) the phase transitions for Hf have never been experimentally studied. I undertook this study of hafnium at high pressure and temperature to produce data with which I could construct the phase diagram and the equation of state for the metal. Previous equation of state (EoS) measurements of hafnium have only been carried out at room temperature. In this study I performed measurements of volume (V) of hafnium at simultaneous high pressure and high temperature to obtain a P - V - T EoS for the α -phase of hafnium. The thermophysical parameters obtained from the P - V - T EoS are fundamental properties of the material, which could be used to calculate the thermodynamic properties of α -Hf at high pressure and high temperature.

Experiment methods

Diamond anvil cell technique

High-pressure and high-temperature experiments have been used to study the physical properties of materials for almost 90 years (Bridgman, 1923). Research involving high pressure greatly accelerated after the 1950's owing to the invention and rapid development of the diamond anvil cell (DAC) technique. Today, the power of the high-pressure and high-temperature experiments is demonstrated by the fact that even after centuries of study of pure elements, high-pressure and high-temperature techniques are still actively used to provide data on their physical properties.

The diamond anvil cell technique has been widely used to study the behavior of materials under very high pressures. A brief history and various analytical techniques used with a diamond anvil cell have been summarized by Jayaraman (Jayaraman, 1986).

Diamond is known as the hardest solid; therefore, using diamond as the choice material for the pressing anvils in a mechanical press device allows for the generation of the highest experimentally achievable pressures. A small sample of material is placed between the two opposing diamond anvils and is held in place using a gasket (Figure 1.1).

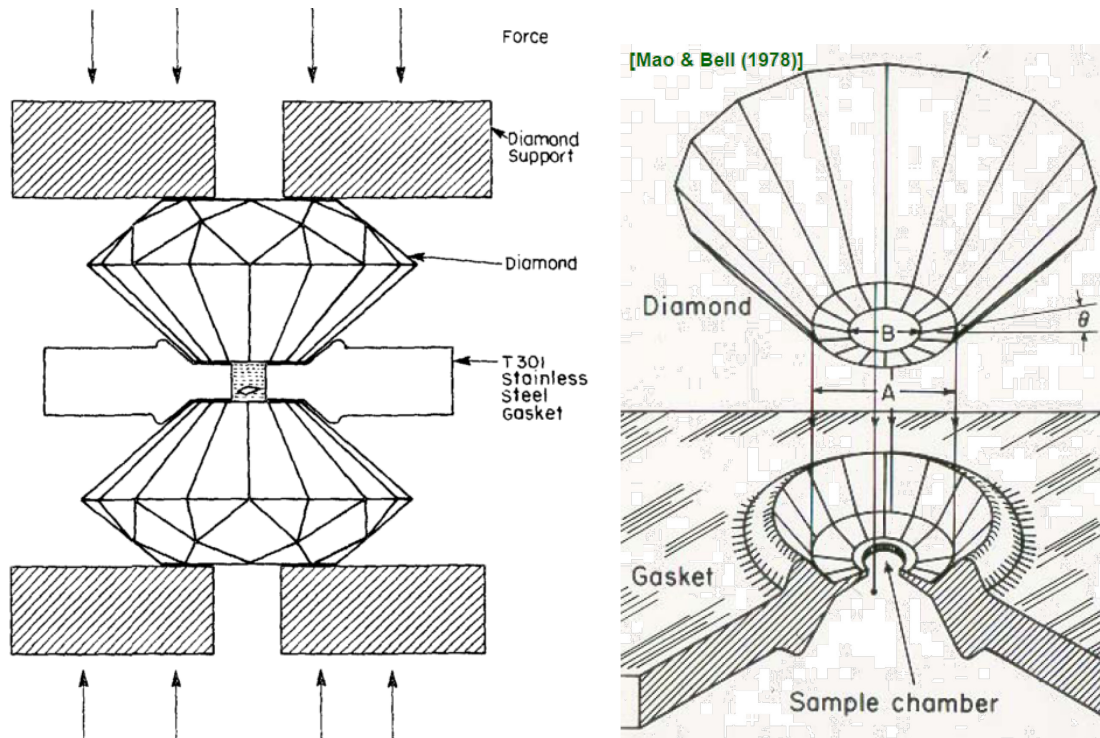


Figure 1.1. Basic principle of the diamond anvil cell (Jayaraman, 1986)

Typically, high pressure is created when axial force is applied from opposing sides using any variation of a typical Mao-Bell type piston-cylinder assembly which holds the diamonds and the gasket, as shown in Figure 1.2.

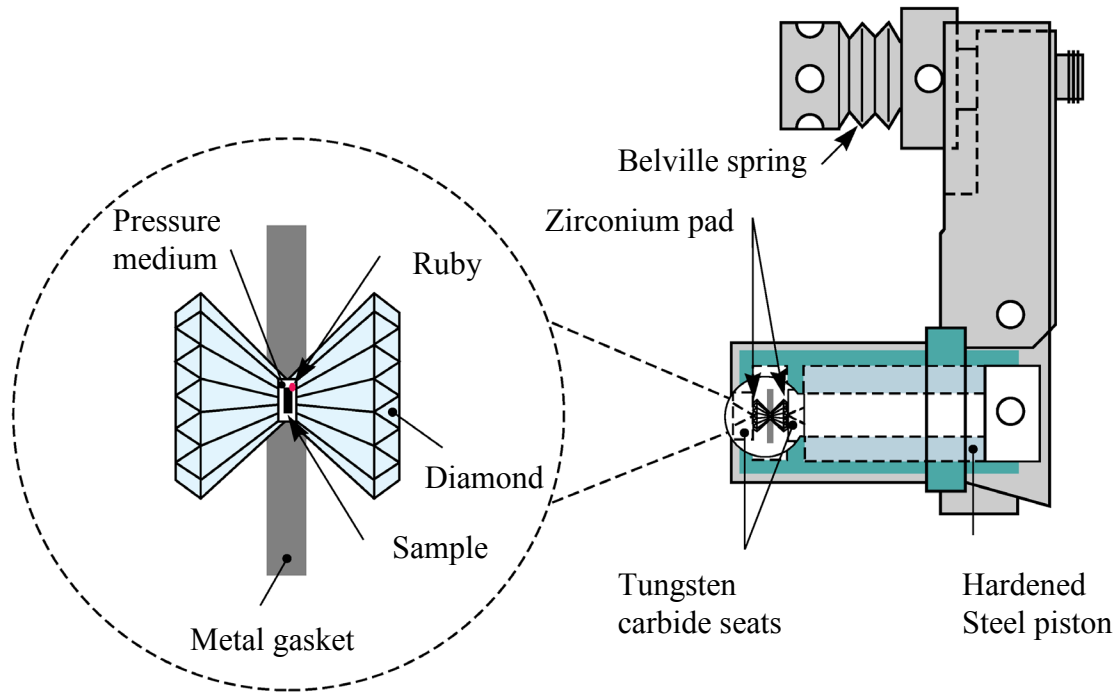


Figure 1.2. Schematic of Mao-Bell type DAC pressing system

Laser heated diamond anvil cell

Ultra-high static pressures achieved using the DAC combined with a laser-heating technique (Shen et al., 2001) or using high temperature electrical heating can create sustained conditions of hundreds of gigapascal (GPa) of pressure (P) and several thousand Kelvin (K) of temperature (T) (see Figure 1.3, Figure 1.4 and Figure 1.5 for a schematic overview of laser heated DAC technique). In this study, the DAC and several high-temperature techniques are used to study, phase diagrams and equations of state and phase transitions of several transition metals at conditions of ultra-high temperatures and pressures.

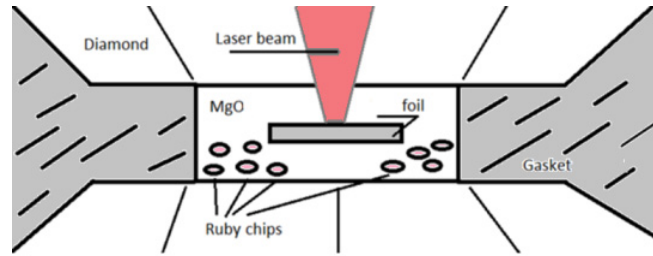


Figure 1.3. Diagram of a laser heated diamond anvil cell. Due to the fact that diamonds are transparent, it is possible to focus a high-power laser onto the pressurized sample and statically heat the sample to ultra-high temperatures.

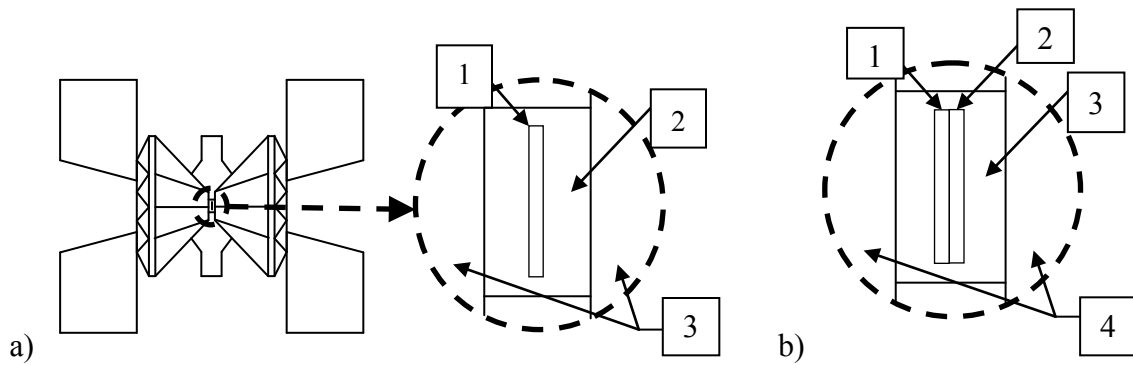


Figure 1.4. a) Schematic of sample foil loading for laser heating in a DAC. 1-sample foil, 2-insulation medium, 3-diamonds. b) Schematic of a double foil sample and internal standard loading for EoS measurement with laser heating and *in-situ* x-ray diffraction. A thin foil of the sample material is sandwiched together with a thin foil of a pressure marker material for example Platinum. (1-sample foil, 2-pressure marker foil, 3-insulation medium, 4 diamonds)

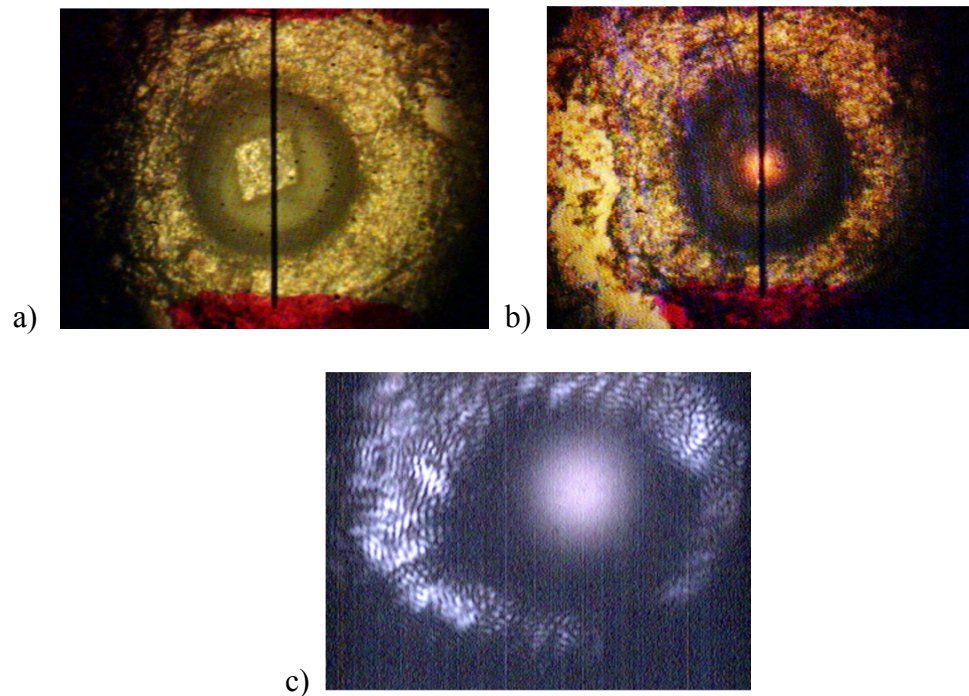


Figure 1.5. Sample loaded into a DAC
 a) typical sample foil loaded into a DAC; b) orange thermal glow seen on laser irradiated sample surface; c) reverse side IR-camera image

Determining the pressure in a diamond anvil cell

Since diamond is optically transparent, spectroscopic techniques can be carried out on the compressed samples in-situ. Optical transparency of the diamonds has enabled a powerful *in-situ* pressure measurement technique to be developed by Mao & Bell (Mao and Bell, 1978) and later (Mao et al., 1986). The pressure dependence of fluorescence from the ruby ($\text{Al}_2\text{O}_3:\text{Cr}$) R-line has been precisely calibrated at various pressures up to 1 megabar (Mbar) by Mao et al. and is commonly used as a pressure scale in DAC experiments (Figure 1.6). A small crystal of ruby ($\sim 5\mu\text{m}$ diam.) is generally placed side by side with the sample and the wavelength of its R-line is measured. An almost linear relationship is used for calculating the pressure from the measured wavelength of the ruby R-line:

$$P = A/B\{[1 + (\Delta\lambda/\lambda_0)]^B - 1\}$$

where P is the pressure in Mbar, λ is the wavelength of the ruby R line, $A = 19.04$, and $B = 7.665$ (Mao et al., 1978).

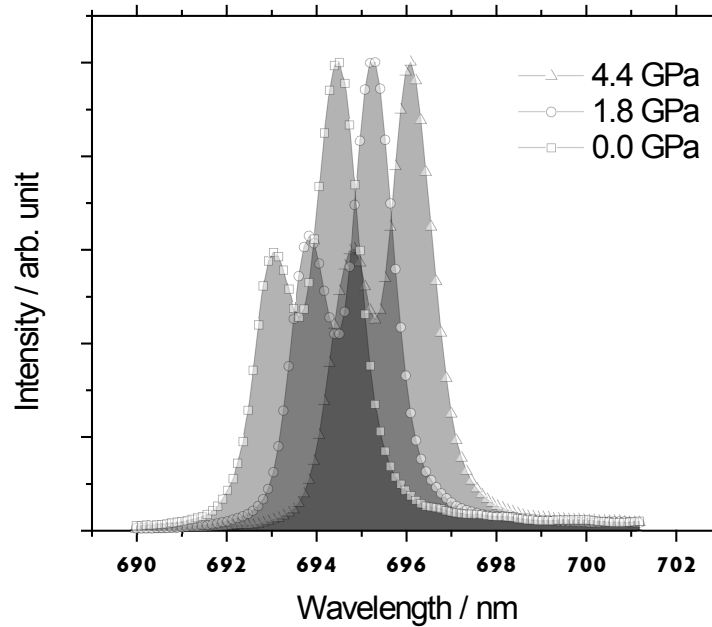


Figure 1.6. Ruby fluorescence shift vs. pressure

Pressure in a DAC can also be determined using x-ray diffraction from a pressure marker material loaded alongside the sample. Pressure-temperature-volume (P - V - T) equations of state (EoS) of several common materials (e.g. MgO, Pt, Au, Ag, Cu, Pd, Mo) have been measured by others at various high pressures and high temperatures. Loading one or more of these materials alongside with the studied sample and measuring their lattice parameters *in-situ* using x-ray diffraction allows one to determine the actual pressure in the DAC (Jamieson et al., 1982; Fei et al., 2007).

Experiment

Commercially obtained hafnium metal powder of 99.5% purity, 325 mesh (Sigma Aldrich) was ground with mortar and pestle to decrease the grain size to less than ~ 5 -10 microns. X-ray diffraction measurements of hafnium under pressures of up to 67 GPa and temperatures in the range between room temperature and 780 K were conducted on the beamline IDB-16 ($\lambda = 0.3981\text{\AA}$) of the Advanced Photon Source (APS) at Argonne National Laboratory. Diffracted x-rays were collected between Bragg angles of $2\theta=5^\circ$ and $2\theta=25^\circ$ using a MAR3450 imaging detector. Measurements at high pressure were carried out using the DAC of symmetrical type with diamonds 300 μm diameter culet. The gasket used in the DAC was made out of 302-type stainless steel and indented to thickness of $\sim 40\mu\text{m}$ and a hole for the sample was drilled with a diameter of 100 μm . Platinum was used as an internal pressure standard and the DAC pressure was controlled remotely using a compressed gas membrane. Neon gas was used as a quasi-hydrostatic pressure transmitting medium. Neon loading into the DAC was done using the high pressure gas loading system in GSE-CARS. In one compression run, NaCl was used instead of neon because of technical difficulties associated with gas loading. The heating was done using a whole-cell external resistive heater provided by HPCAT and the temperature was measured using a thermocouple placed in contact with one of the diamonds. Due to the whole-cell heater design the temperature variations within the volume containing the thermocouple and the sample are taken to be negligible; errors in absolute temperature measurement are estimated to be not more than ~ 5 K. Sample to detector distance and other diffraction geometry parameters were calibrated using a CeO_2 standard. 2D angle-dispersive diffraction images were processed using the software

FIT2D (Hammersley, 2009) to generate the intensity versus two-theta diffraction patterns. Each diffraction peak was indexed and fitted with a pseudo-Voigt function to determine its d -spacing. To determine the a and c lattice parameters of α -phase of hafnium, d -spacings of diffraction peaks (100), (002), (101) and (102) were fitted using least-squares to a hexagonal (space group: $P63/mmc$) lattice. Pressures were calculated based on P - V - T equation of state of platinum by Jamieson et al. (Jamieson et al., 1982). Two platinum diffraction lines, (111) and (200) were used for determination of pressure.

Results and discussion

Hafnium metal was first compressed to a nominal pressure which is required to seal the neon pressure medium between the diamonds and the gasket. The temperature was increased in steps to a given point, followed by a pressure increase in several steps. Subsequently the temperature was decreased in steps back to room temperature and the pressure was increased again in several steps. Two heating \rightarrow compression \rightarrow cooling \rightarrow compression cycles were completed. A plot with a spread of our experimental P - V - T data points is shown in Figure 1.7.

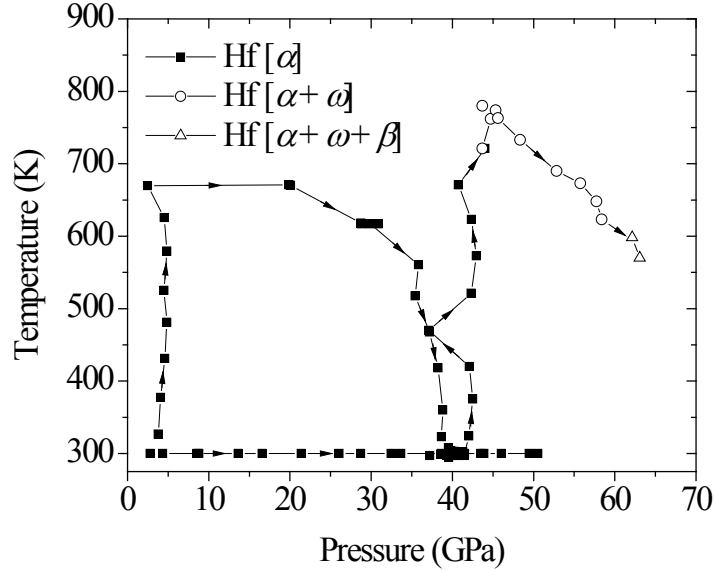


Figure 1.7. P - T range surveyed in APS run 1. (Hrubiak et al., 2012)

High pressure phases of hafnium

Analysis of the obtained x-ray patterns shows that hafnium has two phase transitions in the studied P - T range. Previously reported $\alpha \rightarrow \omega$ phase transition (Xia, Parthasarathy, et al., 1990) was not observed at room temperature in the pressure range studied (up to 51 GPa). According to Xia et al. hydrostaticity, the $\alpha \rightarrow \omega$ phase transition in hafnium occurs at 35 GPa under room temperature compression. Hafnium metal used in our experiment is of similar purity to that used by Xia et al. (Xia et al.: 99.6% purity, our experiment: 99.5% purity) therefore the discrepancy between $\alpha \rightarrow \omega$ phase transition measurements of Xia et al. and our experiment is not due to the differences in sample purity. Compression experiments by Xia et al. were done without any pressure transmitting media therefore their observation may be attributed to large non-hydrostaticity. The effects of non-hydrostaticity on the $\alpha \rightarrow \omega$ phase transition pressure of other group-IV metals have been reported before (Errandonea et al., 2005; Pérez-Prado

and Zhilyaev, 2009). It is generally accepted that in Ti, Zr and many alloys, $\alpha \rightarrow \omega$ phase transition is of a pressure activated martensitic type, not involving any long diffusion paths. The kinetics of $\alpha \rightarrow \omega$ transition are slow due to a slow ω -phase nucleation rate and non-hydrostatic stress is known as one possible driving force for speeding up such transitions (Sikka et al., 1982). The $\alpha \rightarrow \omega$ phase transition was only observed in our x-ray diffraction patterns of compressed hafnium at elevated temperature (Figure 1.7). Moreover, the ω -phase was always seen to be present together with the original α -phase. The fact that the $\alpha \rightarrow \omega$ transition was only observed in hafnium at high temperature could be due to several effects. One of the effects of temperature could be that raising the temperature increases the kinetics of $\alpha \rightarrow \omega$ transition by speeding up the nucleation rate of the ω crystallites, or alternatively by lowering the equilibrium size of stable ω nuclei (Sikka et al., 1982). An alternate explanation could be that the $\alpha \leftrightarrow \omega$ phase equilibrium pressure is actually lowered at higher temperatures. Several previous reports show an increase in the c/a lattice parameter ratio in α -phase titanium with increasing pressure before (Errandonea et al., 2005), and others suggest that the effect of increasing of the c/a ratio could be an artifact of non-hydrostatic compression (Zhang et al., 2008). However, in some cases the change of the c/a ratio in an *hcp* lattice may actually be an indication of pressure induced change in electronic structure (Clendenen and Drickamer, 1964). Effects of pressure on lattice parameters of transition metals have been investigated for a long time, including in titanium (Errandonea et al., 2005) which is usually a test case for studies of $\alpha \rightarrow \omega$ transitions. In our observation at room temperature, the c/a ratio increases from an ambient pressure value of ~ 1.58 to ~ 1.61 at a higher pressure Figure

1.8. The c/a ratio increase in compressed hafnium is similar to those previously reported for titanium (Errandonea et al., 2005; Zhang et al., 2008).

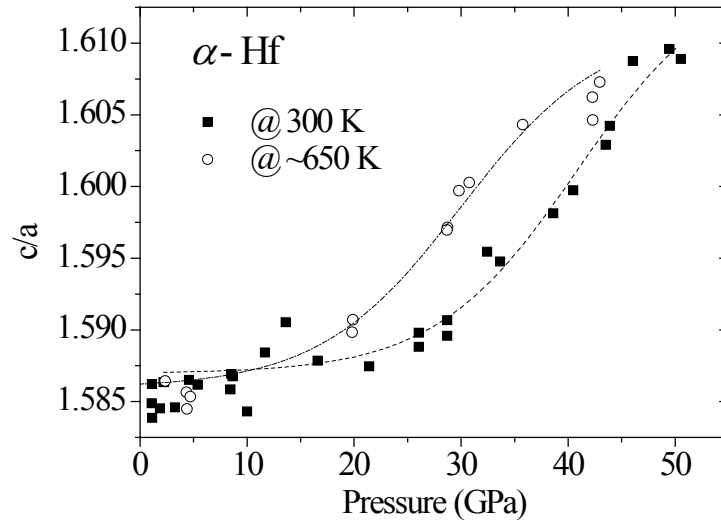


Figure 1.8. Variation of c/a ratio of α -hafnium (hcp) unit cell with increasing pressure at two different temperatures. (Hrubiak et al., 2012)

As can be seen in Figure 1.8, the increase of the c/a ratio is not linear but resembles a diffuse step from ~ 1.58 to ~ 1.61 at a certain crossover pressure. Unexpectedly, at a higher temperature the c/a ratio is seen to change over from its lower value to the higher value at a lower pressure. This observation suggests that the relative compressibility of a and c axes in α -hafnium is temperature dependent which could explain the lowering of the observed $\alpha \rightarrow \omega$ phase transition pressure at high temperatures.

At even higher pressures, the x-ray diffraction patterns show a predominant presence of a β phase of hafnium with very small amounts of residual ω and α phases. The ω phase of hafnium remained stable in all region of the P - T range studied. It was always present with other phases, either with α phase or with both α and β phases. In

summary, x-ray diffraction patterns collected at P - T range of our experiment show three distinct phase regions. Region I: α phase only (Figure 1.10c); region II: α and ω phases are observed (Figure 1.10b); region III: β , ω and α phases are observed, with β as the most predominant (Figure 1.10a).

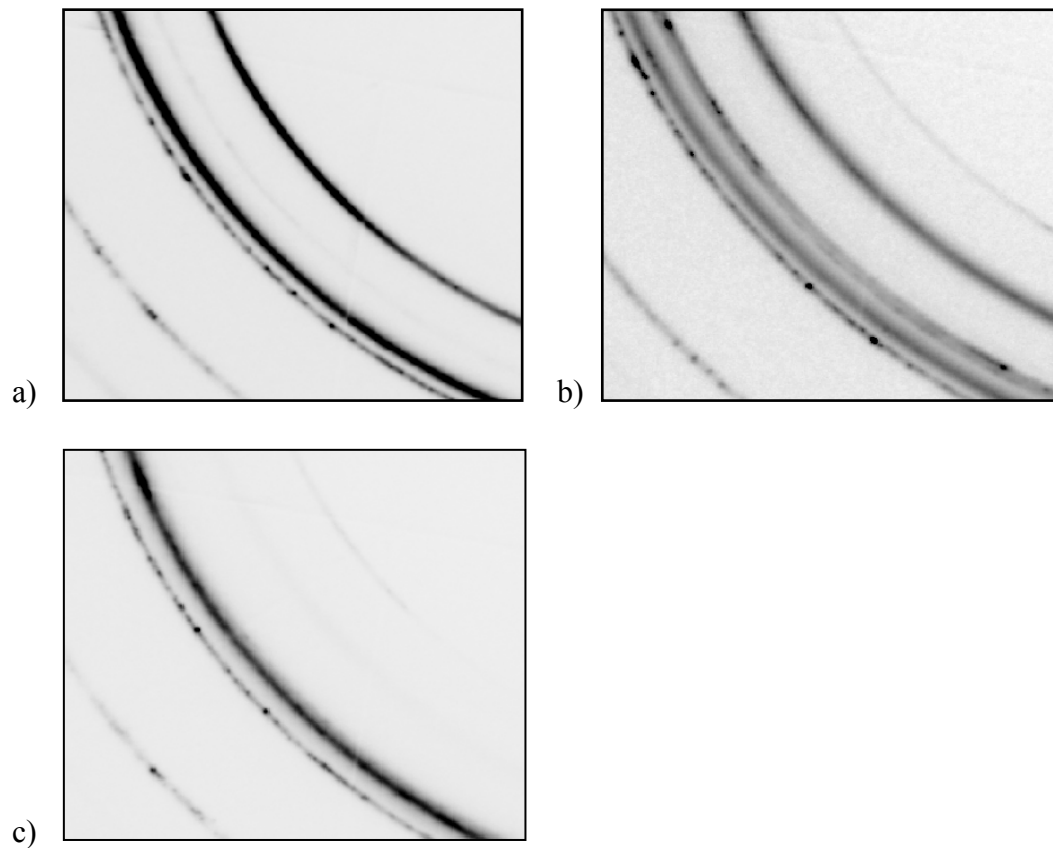


Figure 1.9. Representative x-ray diffraction patterns of hafnium collected during resistive heating in APS. a) Hf *hcp* phase, $P = 22$ Gpa, $T = 670$ K; b) Hf *hcp* + ω phases, $P = 45$ Gpa, $T = 774$ K; c) Hf *bcc* phase, $P = 63$ Gpa, $T = 570$ K

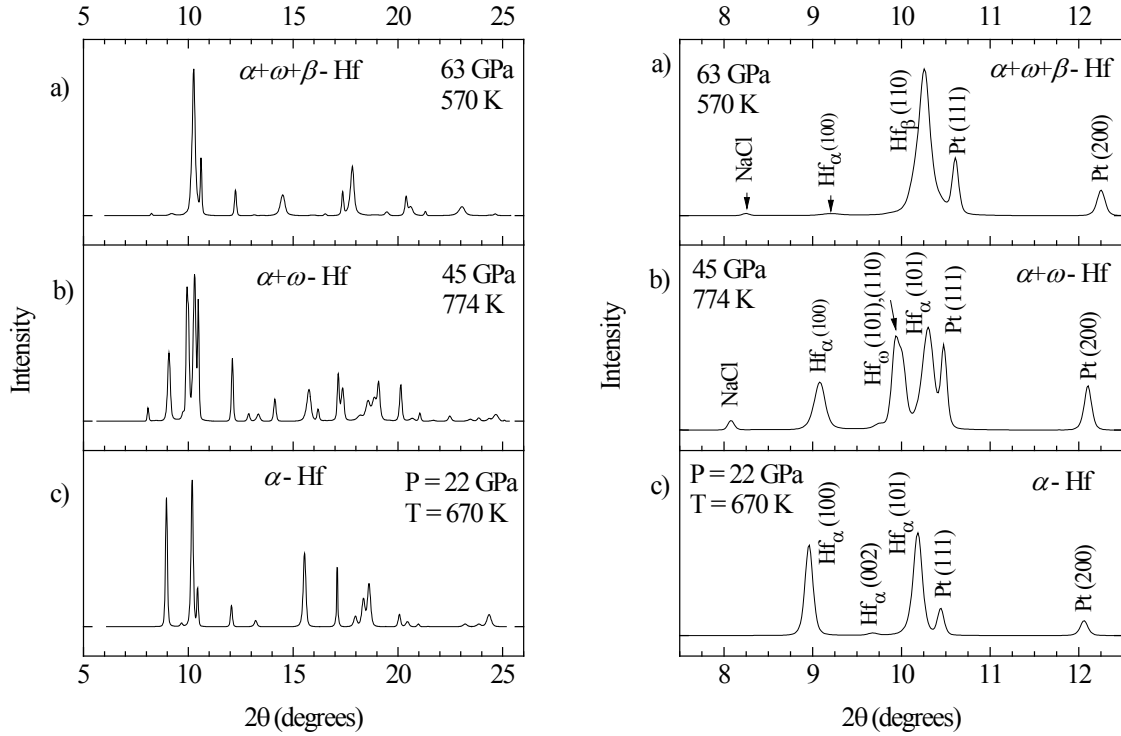


Figure 1.10. Representative area-integrated x-ray diffraction patterns of Hf in several P - T regimes (Hrubiak et al., 2012)

Isothermal equation of state of α -phase hafnium

The pressure (P) - volume (V) relation for solids at room temperature can be described by a third order Birch-Murnaghan equation:

$$P = 3/2B_0[V/V_0]^{-7/3} - (V/V_0)^{-5/3} \{1 + 3/4(B_0' - 4)[(V/V_0)^{-2/3} - 1]\} \quad \text{EQ. 1-6}$$

B_0 and B_0' are the zero pressure bulk modulus and the first pressure derivative of the bulk modulus at zero pressure, respectively. V and V_0 are the volumes at a given high pressure and at zero pressure, respectively. The least squares fit of our experimental data for the α -phase to EQ. 1-6 gives $B_0 = 112.9 \pm 0.5$, $B_0' = 3.29 \pm 0.05$ (Figure 1.11).

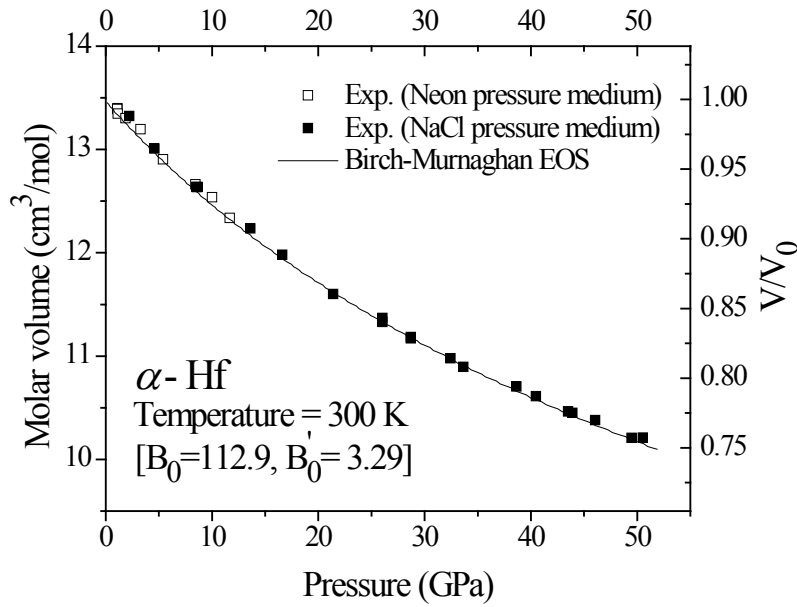


Figure 1.11. Pressure-volume relation of α -phase hafnium at room temperature (Hrubiak et al., 2012)

P-V-T equation of state of the α -phase hafnium

High pressure and high temperature EoS could be used to better understand the thermophysical behavior of α -Hf in extreme conditions. Several studies (Jacobs et al., 2000; Lu et al., 2005a) have shown that, the well-known Birch-Murnaghan EoS gives a wrong prediction of thermophysical properties at high pressure and high temperature, like negative heat capacity and thermal expansion. Thus, CALPHAD compatible EoS (as described in the previous section) was used in this study.

I used *Optimization* module of the *FactSage 6.2* thermodynamic software (Bale et al., 2009) as the tool for determining the multi-parameter *EoS* of α -hafnium. *P-V-T* experimental data from the current study as well as ambient pressure thermal expansion data from the literature (Adenstedt, 1952; Touloukian et al., 1979) were used as the sources of experimental data for determining the EoS parameters. The software *Optisage*

was used to optimize all the parameters to minimize the error between experimental value and calculated data. The bulk modulus (B_0) and its derivative (B_0') at 300 K were calculated with the Birch – Murnaghan equation (EQ. 1-6). Optimized *EoS* parameters can be used as the input for *ChemSage* (Eriksson and Hack, 1990) or *FactSage* (Bale et al., 2009) thermodynamic software to calculate all thermodynamic properties at high *P-T* conditions. All the parameters needed to be assessed together with the optimized values and their calculated error for α -phase hafnium are listed in Table 1.2.

Table 1.2. CALPHAD EoS parameters for α -Hf (Hrubiak et al., 2012)

Z	V_0 (cm ³ /mol)	B_0 (GPa)	B_0'	θ_0	γ_0	δ_0	b_0	δ_1	b_1
72	13.432 ± 0.015	112.9 ± 0.5	3.29 ± 0.05	300	0.231 ± 0.015	0.76 ± 0.07	1	9.50 ± 0.58	0.65 ± 0.09

Fitting to the Brosh model EoS involves thermodynamic variables such as entropy and heat capacity whose temperature dependence must vary in a physically consistent way under high pressure, i.e. the values for heat capacity must not anomalously become negative at very high pressures as is the case with other EoS models (Brosh et al., 2007; Karbasi, Saxena & Hrubiak, 2011). In order to check whether our EoS fit is physically consistent, pressure and temperature dependence entropy and heat capacity of α -phase hafnium were calculated at several pressures using the fitted EoS. As can be seen in Figure 1.12a and Figure 1.12b respectively, heat capacity (C_p) increases monotonically with pressure and entropy (S) decreases. Clearly, the behavior of C_p and S that is predicted by the EoS model does not show any anomalous negative deviation at high temperatures.

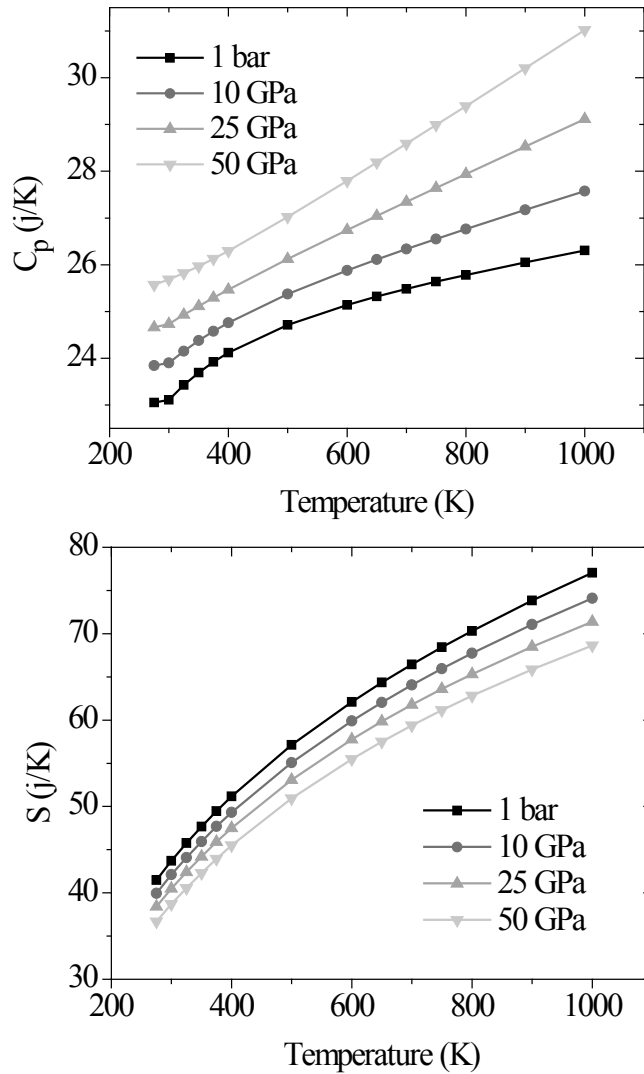


Figure 1.12. a) Heat capacity of α -phase hafnium as functions of temperature at several pressures calculated from P - V - T EoS; b) Entropy of α -phase hafnium as functions of temperature at several pressures calculated from P - V - T EoS (Hrubiak et al., 2012)

The consistency of this calculated thermophysical data is encouraging because it could potentially be used to better understand the P - T phase diagram of hafnium and mechanisms of its phase transitions in future studies. This P - V - T EoS reproduces the experimental molar volumes of the α -phase hafnium at all P - T points with $\sim 1\%$ error

(Figure 1.13) and fits well with the literature reported data on ambient pressure thermal expansion (Figure 1.14).

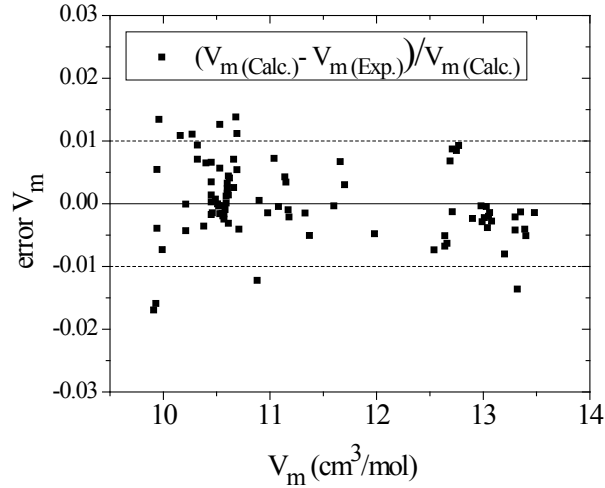


Figure 1.13. P - V - T EoS molar volume calculation errors for the entire P - T range of our experiment. (Hrubiak et al., 2012)

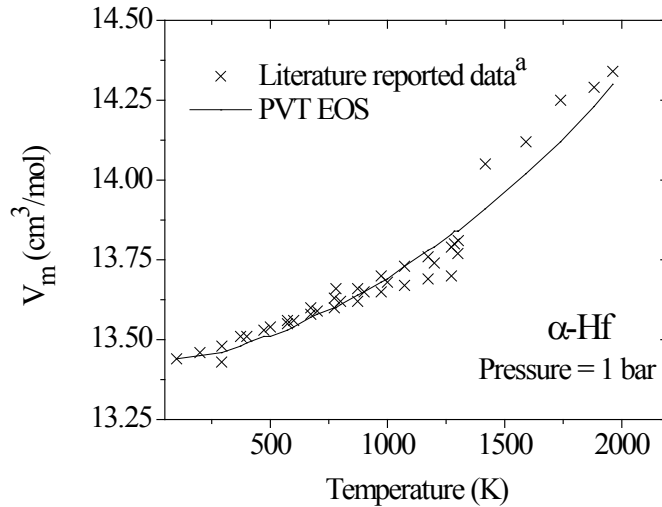


Figure 1.14. Comparison of literature reported data on thermal expansion of hafnium and data calculated using our P - V - T EoS.

Literature data on thermal expansion of hafnium was included in our P - V - T EoS determination. (Hrubiak et al., 2012) Superscript a: Data points were compiled from several literature sources (Adenstedt, 1952; Baldwin, 1954; Golutvin and Maslennikova, 1970; Touloukian et al., 1979a)

The overall accuracy of the EoS prediction mostly depends on the accuracy of the input experimental data. With about 5% experimental error in original experimental data, the calculated thermophysical properties as compared to those from literature are well within the error margin.

Additionally, for a comparison with the common Mie-Grüneisen model, the calculated Grüneisen and Anderson-Grüneisen parameters (i.e. γ_0 and δ_0) for α -Hf are consistent with the experimental data of other elements of Group IVB, as shown in Table 1.3 and Figure 1.15. The values of the Grüneisen parameters are seen to decrease linearly with the atomic number. Similar behavior has been reported in other transition metals (Rao, 1974).

Table 1.3. Bulk modulus (B_0), and derivative bulk modulus (B_0'), Grüneisen (γ_0) and Anderson-Grüneisen (δ_0) parameters of Group IVB transition metals (Figure 1.15) (Hrubiak et al., 2012)

	B_0 (GPa)	B_0'	γ_0	δ_0	Ref.
Ti	114(3)	4.0 (fixed)	1.28, 1.18	2.21	7,19
Zr	93(2)	3.1-4.0	0.83, 0.71	1.56	19,20
Hf	112.9±0.5	3.29±0.05	0.231±0.015	0.76±0.07	<i>This Work</i>

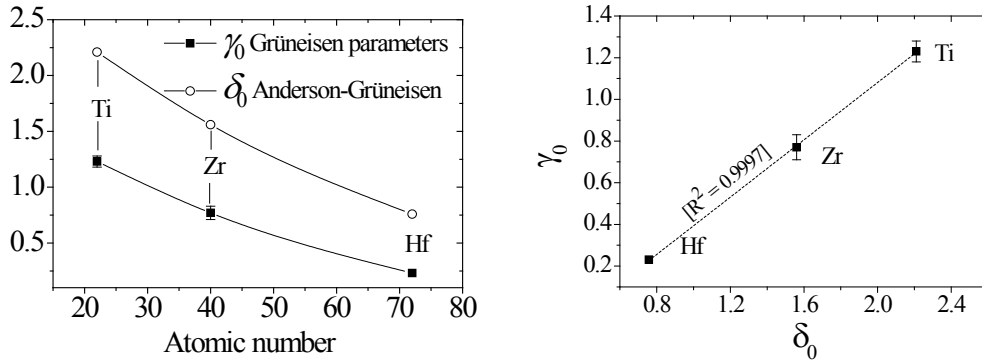


Figure 1.15. Left: For Group IVB transition metals, γ_0 and δ_0 are seen to decrease with increasing atomic number of element. Right: The relationship between γ_0 and δ_0 is nearly $\delta_0 = 2 \gamma_0$, which is consistent with previously reported trend (Rao, 1974) (Hrubiak et al., 2012)

Conclusion

In summary, this study explored the high pressure and temperature behavior of hafnium by *in situ* x-ray diffraction experiments at pressures up to 61 GPa and temperatures up to 780 K. It was observed that the $\alpha \rightarrow \omega$ phase transition only occurs at high temperature and pressure and the $\omega \rightarrow \beta$ phase transition at still higher pressure. Observations have also shown an unexpected temperature dependence of the c/a unit cell parameter ratio in α -phase. I conclude that there is a correlation between the c/a ratio changeover from ~ 1.58 to ~ 1.61 in the α -phase hafnium and the P - T conditions required for the occurrence of the $\alpha \rightarrow \omega$ phase transition. My subsequent study, described in the following section, confirms this conclusion. A P - V - T equation of state for the α -phase was derived by combining data on the volume measurements at high temperature and pressure obtained in this study as well as volume data from existing literature on thermal expansion at 1 bar.

The EoS results from this study helped in the understanding of the thermodynamics of hafnium at high pressures and temperatures. As will be shown in the next sections, the results from this study aided me in theoretical modeling of transition metals and understanding of their phase transitions under high P - T conditions. The EoS results obtained here are used in the following sections of this thesis to determine thermodynamic parameters of all phases of hafnium at high ranges of P - T conditions and to create a thermodynamically consistent phase diagram.

1.03 Thermodynamically consistent EoS and phase diagrams of Ti, Zr and Hf

I measured the volumes (V) of titanium, zirconium and hafnium at several pressures (P) up to 50 GPa and at temperatures (T) between 300 to 2000 K using a laser-heated diamond anvil cell (DAC) with synchrotron X-Ray diffraction at the Advanced Photon Source (APS) and resistively-heated DAC with synchrotron X-Ray diffraction at the Cornell High Energy Synchrotron Source (CHESS). The measured data combined with previously reported experimental data allows me to determine thermodynamically assessed P - V - T equations of state (EoS) of α , β and ω phases of titanium, zirconium and hafnium using an EoS model by Brosh et al. Experimentally measured volume data in combination with literature data on thermodynamic properties of titanium, zirconium and hafnium at a pressure of 1 bar have been used to assess high P - T phase diagrams for these metals. Thermodynamic calculations based on the acquired volume data, and measured temperature dependence of relative compressibilities of a and c lattice parameters in α -hafnium suggest that in contrast to titanium and zirconium, the hcp (α) to simple hexagonal (ω) phase equilibrium line in hafnium has a slope $dT/dP < 0$.

A database containing all assessed high P - T thermodynamic properties of titanium, zirconium and hafnium as a collection of tabulated values is included in the APPENDIX.

Introduction

Group IVB elements: Ti, Zr, Hf

The hexagonally close packed (hcp) metals [i.e. titanium, zirconium, hafnium] are especially interesting to study because they undergo electronic phase transitions at fairly modest pressures. As is well known, increasing pressure mediates the transfer of

electrons from the s to the d band in transition metals. The Group IVB transition metals have a partially filled d band which easily gets filled up by the increase of pressure. Increasing the occupancy of the d band in transition metals like Ti, Zr, and Hf makes these transition elements more electronically similar to transition metals from the middle columns of the periodic table (i.e. Groups VB and VBI) prompting a transformation to a bcc structure which is common among those transition metals (Xia et al., 1990; Vohra and Spencer, 2001; Akahama et al., 2002). Ti, Zr, and Hf can exist in several different phases depending on the P - T conditions; therefore, accurate P - V - T data for each of the high P - T phases is required in order to create a complete EoS for these metals. At ambient pressure Ti, Zr, and Hf transform from a room-temperature α (hcp) to a (β -phase) (bcc) structure at temperatures above 1155K, 1135K, and 2030K respectively. And upon increasing the pressure at room-temperature, Ti, Zr and Hf undergo a sequence of $\alpha \rightarrow \omega$ (simple hexagonal) $\rightarrow \beta$ phase transitions (distorted bcc in case of Ti) (Xia, Parthasarathy, et al., 1990; Vohra and Spencer, 2001), where the ω phase is an intermediate phase between the α (hcp) and β (bcc) phases (Xia et al., 1990; Joshi et al., 2002), see Figure 1.16.

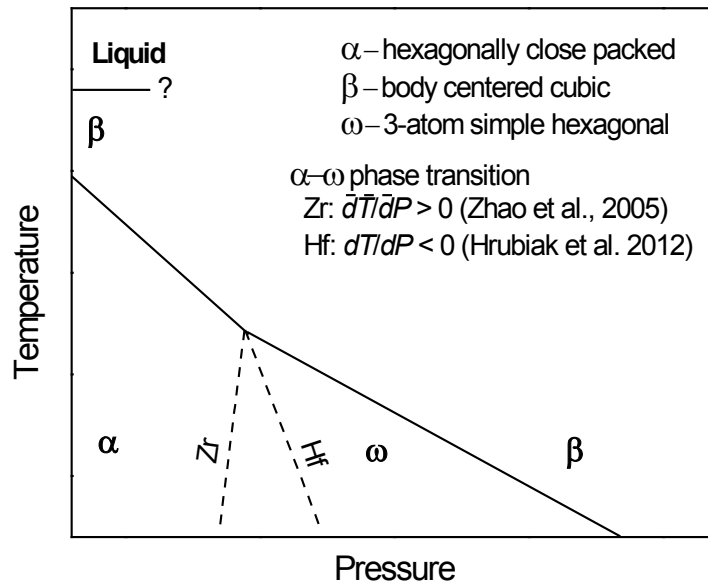


Figure 1.16. Schematic phase diagram of Zr and Hf at high P - T . The plot is only to show the similarity between the topology of pure Zr and Hf respective phase diagrams, the temperature and pressure scales are not the same for Zr and Hf. Zr and Hf were expected to follow a similar P - T topology of their respective α - β - ω phase equilibria. I suggested in the previous section that the $\alpha - \omega$ phase transition in hafnium has a slope $dT/dP < 0$ (shown as dashed line, labeled Hf) in contrast to the case with zirconium for which the $\alpha - \omega$ phase transition has been studied at high P - T by Zhao et al. (Zhao et al., 2005) and was determined to have slope $dT/dP > 0$ (shown as dashed line labeled Zr). Melting temperatures at high pressures have not been determined for either Zr or Hf.

It is currently not known whether the high temperature bcc phases and the high pressure bcc phases for hafnium are connected on the phase diagram or are possibly separated by some hitherto unknown intermediate phases. Creation of comprehensive equations of state for Ti, Zr, and Hf is hindered by the lack of experimental measurements of volumes and precise measurements of phase transition boundaries under simultaneous high pressure and high temperature conditions. A systematic experimental measurement of molar volumes and phase transition boundaries at simultaneously high

temperature and high pressure conditions is required in order to compile a comprehensive thermodynamic database and a P - V - T equation of state for these metals. Volumes of *hcp* (α) phases of Ti and Zr have been extensively measured at various high pressure and temperature conditions and have been compiled from several recent sources. Some data is available on volumes of the ω and β phases of Ti and Zr however there is some discrepancy between different sources about the placement of the phase diagram boundaries between these phases at very high pressures and temperatures (Rao and Menon, 1973; Xia, Duclos, et al., 1990; Greeff, 2005; Zhang et al., 2005; Zhang, Zhao, et al., 2008; Zhao et al., 2005; Lu, Selleby, et al., 2005b; Pecker et al., 2005; Liu, Li, et al., 2008; Tian, Sun, Yang, et al., 2008; Tian, Sun, Zhang, et al., 2008; Pérez-Prado and Zhilyaev, 2009; Speirs, n.d.). Several conflicting sources have reported a discovery of novel ultra-high pressure phases in Ti, however there have not been any attempts to determine their high temperature properties (Vohra and Spencer, 2001). Melting curve of Ti has been measured in a DAC (Errandonea, Schwager, et al., 2001a) up to 80 GPa. High pressure melting curves of Zr and Hf at high pressure have so far not been reported.

Non-hydrostatic compression in a diamond anvil cell

Typical experiments to measure volumes and determine the *EoS* of materials at ultra-high pressures rely on the use of some type of a diamond anvil cell (DAC). Diffraction experiments in a DAC can be done using either an axial or a radial geometry. In an axial geometry, which is by far the most common technique, (Singh, 1993) the x-ray beam is parallel to the direction of load. In the radial geometry, the x-ray beam can be positioned perpendicular to the load direction (Figure 1.17).

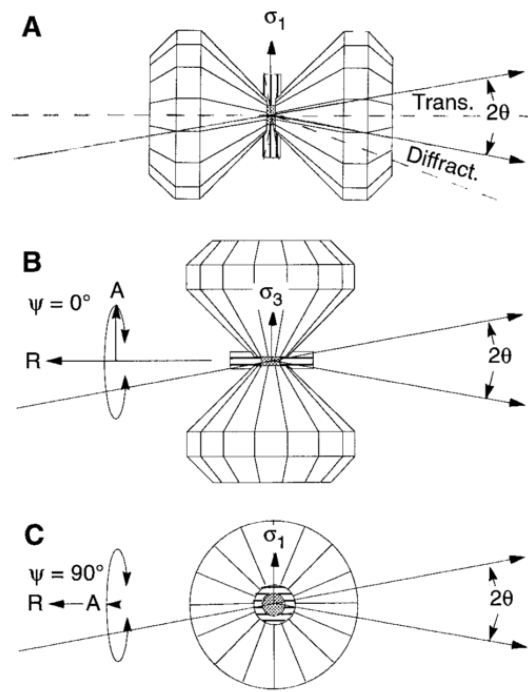


Figure 1.17. Three geometries for the diamond-cell x-ray experiments. (A) Conventional (axial) geometry for x-ray diffraction and transmission. (B) Radial diffraction geometry with $\Psi=0^\circ$ and (C) radial diffraction geometry, $\Psi=90^\circ$. A, axial direction; Image by Hemley et al. (Hemley et al., 1997)

One of the very important problems in accurate measurement of EoS in a diamond anvil cell is the fact that stress which a sample experiences in a DAC is never truly hydrostatic which can result in large errors (Singh and Kenichi, 2001), especially in hexagonal metals (Weinberger et al., 2008). It is known that by using the radial geometry and the anisotropic elasticity theory, it is possible to obtain accurate measurements of hydrostatic lattice constants even in experiments with non-hydrostatic loading (Singh, 1993; Singh and Balasingh, 1994).

Summary of lattice strain theory developed by Singh was summarized into a single equation by Uchida et al. (Uchida et al., 1996). In fact systematic studies on different materials compressed in a DAC have shown that in order to minimize errors of

pressure determination which arise from non-hydrostatic stress when using a material with a negative elasticity anisotropy factor (S) (Singh, 1993) one should compute pressure from (200) or (400) lines and when using a pressure marker with a positive S one should compute pressure from (111) or (222) lines (Funamori et al., 1994). Lattice strain theory has been applied to high pressure of earth materials FeO and Iron estimation of elastic moduli (Singh et al., 1998) using radial diffraction. Among other studies utilizing the lattice strain theory, Duffy et al. measured elasticity, shear strength and equation of state of molybdenum and gold from x-ray diffraction up to 24 GPa (Duffy et al., 1999). Most measured room temperature P - V data for elements reported in literature have been obtained using typical axial-diffraction geometry DACs and could contain systematic errors due to non-hydrostatic compression effects. Since thermal EoS measurements rely on accurate assumption of room temperature P - V data, the accuracy of the hitherto reported thermal EoS' for many elements should be re-assessed.

Experiment

X-ray diffraction measurements with in-situ laser heating under pressures of up to ~50 GPa and temperatures in the range between room temperature and 2600K were conducted on the beamline IDB-16 ($\lambda = 0.3981\text{\AA}$) of the Advanced Photon Source (APS) at Argonne National Laboratory. Diffracted x-rays were collected between Bragg angles of $2\theta=5^\circ$ and $2\theta=25^\circ$ using a MAR3450 imaging detector. Angle-dispersive X-ray diffraction of Zr was also measured at room temperature from 1 bar up to 65 GPa using a Mo-source X-ray diffractometer (Bruker ASX) in CeSMEC. X-ray diffraction measurements with resistive heating of the DAC on Hf were also conducted using a MAR3450 imaging detector on B2 beamline ($\lambda = 0.485\text{\AA}$) at Cornell High Energy

Synchrotron Source (CHESS). The sample, a commercially obtained hafnium metal foil of 99.97% purity with nominal 3% Zr was loaded into a DAC of symmetrical type with diamonds 400 μ m diameter culet. The gasket used in the DAC was made out of 302-type stainless steel and indented to thickness of \sim 40 μ m and a hole for the sample was drilled with a diameter of 100 μ m. Platinum was used as an internal pressure standard. For a sample loading schematic refer to Figure 1.4. MgO powder, dried at 1000 $^{\circ}$ C, was used as the pressure transmitting and insulation medium. The laser heating was done using the double sided laser heating system in APS and the temperature was measured using a non-contact radiometric technique (Shen et al., 2001; Meng et al., 2006a). Resistive heating of Hf was carried out at CHESS using a modified graphite heating technique. During resistive heating the temperature was measured using a thermocouple which was indented together with the gasket and was in contact with the culet of the diamond.

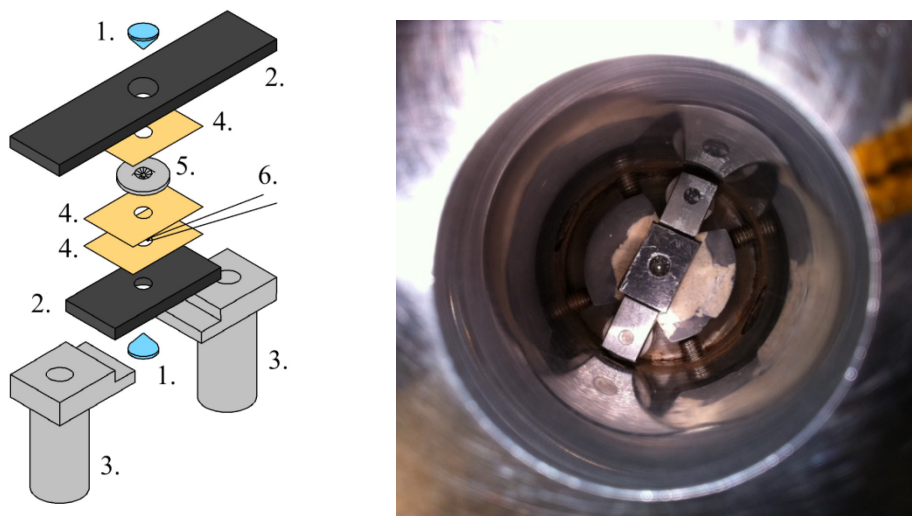


Figure 1.18. Resistive heating schematic. Resistive heating was done at CHESS using a graphite heater assembly. a) expanded view of graphite heater assembly: (1 – diamond, 2 – flexible graphite strip, 3 – electrical connectors, 4 – dielectric foil, 5 – gasket, 6 – thermocouple); b) heater assembly photo

Sample to detector distance and other diffraction geometry parameters were calibrated using a CeO₂ standard. 2D angle-dispersive diffraction images were processed using the software FIT2D (Hammersley, 2009) to generate the intensity versus two-theta diffraction patterns. Each diffraction peak was indexed and fitted with a pseudo-Voigt function to determine its *d*-spacing. To determine the *a* and *c* lattice parameters of α -phase of hafnium, *d*-spacings of diffraction peaks (100), (002), (101) and (102) were fitted using least-squares to a hexagonal (space group: *P63/mmc*) lattice. Pressures were calculated based on *P-V-T* equation of state of platinum by Fei et al. (Fei et al., 2007). Two platinum diffraction lines, (111) and (200) were used for determination of pressure. A custom crystallographic calculation software package was created to automatically calculate volumes of different phases present in a diffraction pattern to facilitate the large number of volume calculations needed to process the very large amount of measured x-ray diffraction data. Volume data from most heating runs was determined using the new software algorithm. In cases where there was *hkl* peak overlap, manual fitting and volume computation was done.

As I have mentioned earlier, the experimental setup during this experiment involves ‘sandwiching’ our sample material with a pressure marker material (in this case platinum) During laser heating of different metals in a DAC there is sometimes a chance for atomic inter-diffusion of different metal species to occur. It is known that the lattice spacing of Pt and Hf is dependent upon their purity (Ellner, 2004) therefore because our pressure determination depends on the precise measurement of the lattice parameters of our internal pressure standard, any intermetallic diffusion during our laser heating experiment is not desirable. Even though platinum and *hcp* metals such as platinum and

titanium, zirconium, and hafnium generally do not interdiffuse easily, when they do, their lattice parameter can change by as much as 10% (Ellner, 2004). This much interdiffusion would completely invalidate any inference of pressure measurements made in the DAC at high temperatures during laser heating. In order to make sure that the interdiffusion in our experiments does not have a measurable effect on our pressure determination I used two independent pressure standards in this study. Before heating, pressure was independently determined using platinum and MgO. Pressure of the sample at high temperature was determined by using diffraction from platinum. In order to confirm that there was not a measurable amount of interdiffusion between our sample and the platinum pressure marker, the pressure measurements were checked after quenching.

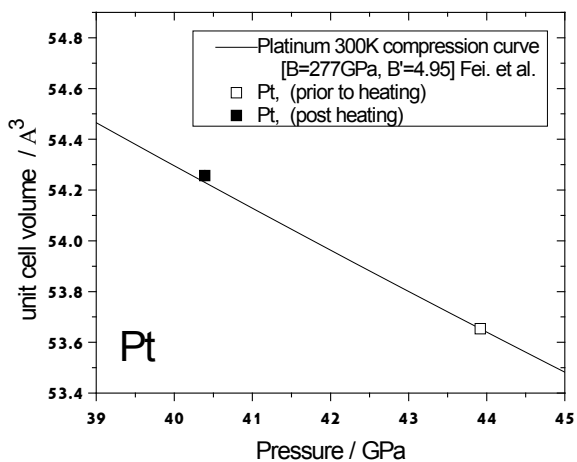


Figure 1.19. Platinum pressure measurement validation

Results and discussion

In this study, new measurements of molar volumes of titanium, zirconium and hafnium were obtained at the following pressure and temperature ranges:

Titanium: up to 35 GPa / up to ~ 2000 K – 3 pressure points

Zirconium: up to 45GPa / up to ~ 2000K – 3 pressure points

Hafnium: up to 47 GPa / up to ~ 2000K – 5 pressure points

- Approximately 20 temperature points at each pressure
- Total: more than 700 diffraction patterns collected

The 2-d intensity plot in Figure 1.20 shows a succession of integrated intensity vs. 2θ x-ray diffraction patterns collected at a succession of increasing temperature points. Each horizontal line in the 2-d intensity plot corresponds to a single x-ray diffraction pattern collected at a given temperature. Disappearance of some hkl peaks and appearance of new hkl peaks signals a structural phase transition and by stacking the collected x-ray diffraction patterns in the manner presented in Figure 1.20 one can clearly see the temperatures at the beginning and the completion of various structural phase transitions. The plots were created using the comprehensive crystallographic calculation software package designed during this study. The software allowed an organized and systematic approach to process a large set diffraction of data (i.e. automatic peak fitting and lattice refinement of different phases) coupled with measurements of temperatures, pressures and laser power (during runs where laser heating was used).

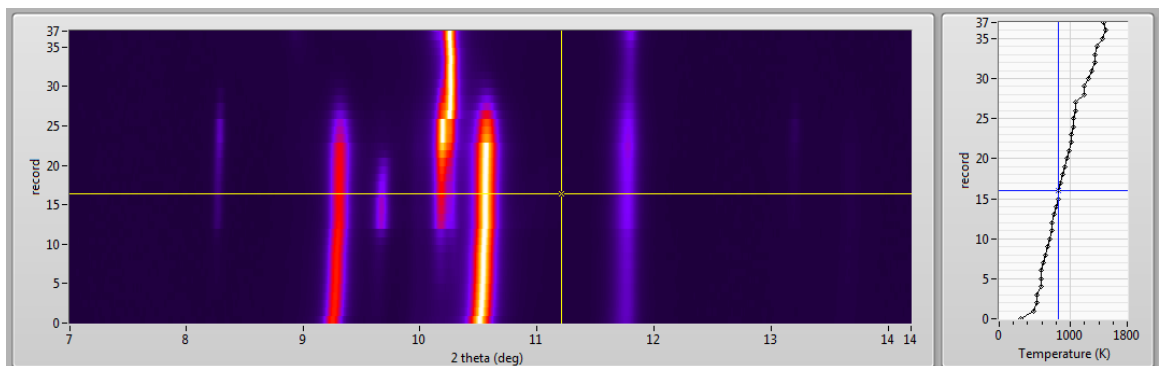


Figure 1.20. Progression of integrated intensity vs. 2θ plots with increasing temperature at a constant pressure. Right of intensity plots: transposed temperature vs. frame number plot. Pressure = 43 GPa.

The software exports spreadsheet files with calculated data on volume, individual lattice parameters, pressure, temperature, laser power.

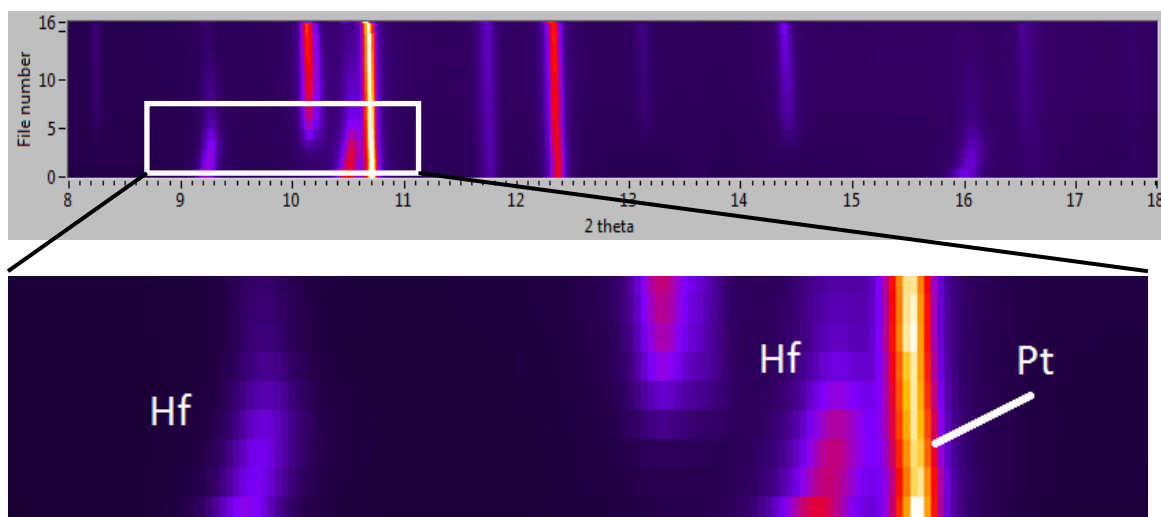
Hafnium

At high pressure of about 43 GPa, upon visual examination of the 2-d intensity plot of x-ray diffraction patterns for hafnium (Figure 1.22a), it can be seen that at low temperatures the *hkl* reflections of hafnium show unexpected temperature dependence. With increasing temperatures, hafnium *hkl* reflections shift towards higher 2- θ angles, indicating a decrease in volume, meanwhile platinum and MgO reflections shift toward lower 2- θ angles indicating an increase in volume, see Figure 1.22a (see magnified insert). During laser heating the difference in temperature between platinum and hafnium was kept under 100 K. Assuming hafnium and platinum are under the same pressure and temperature conditions this means that α -hafnium lattice has a tendency to decrease in volume with increasing temperature. Since measured volumes at each *P-T* condition are not exactly at the same pressure (see Figure 1.21) the observed negative volume change in hafnium could have been due to an increase in pressure.

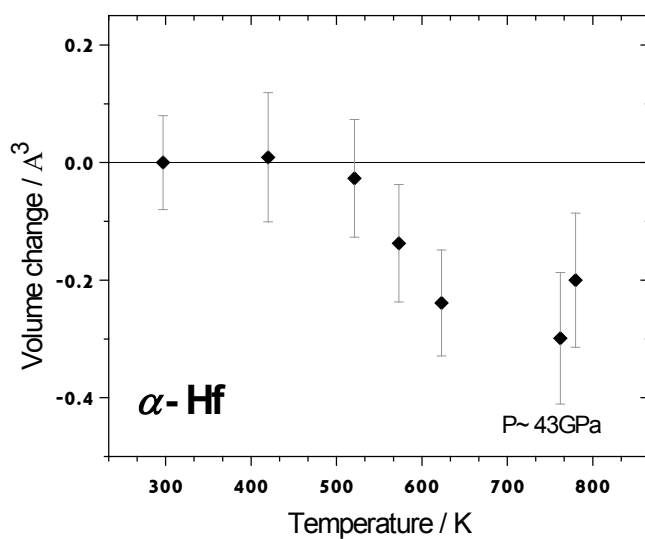
Figure 1.21. Volume measurements for α -Hf at high P - T

To solve this ambiguity, I used an internal platinum pressure marker which was heated to the same temperature and is assumed to be at the same pressure as the hafnium sample. Using the internal pressure marker, I could precisely constrain the pressure for each measured hafnium volume data point using the thermal P - V - T equation of state proposed by Fei et al. (Fei et al., 2007). Having the accurate pressure and temperature at each data point, I recalculated the volumes of hafnium at each data point to a single isobar at a pressure of the room temperature data point using a P - V equation of state determined by Hrubciak et al. (Hrubciak et al., 2012). By recalculating the volumes at each data point to a single pressure I obtained an approximate temperature dependence of volume of hafnium on temperature alone. Temperature dependence of volume of α -hafnium calculated in this way shows a negative correlation between room temperature

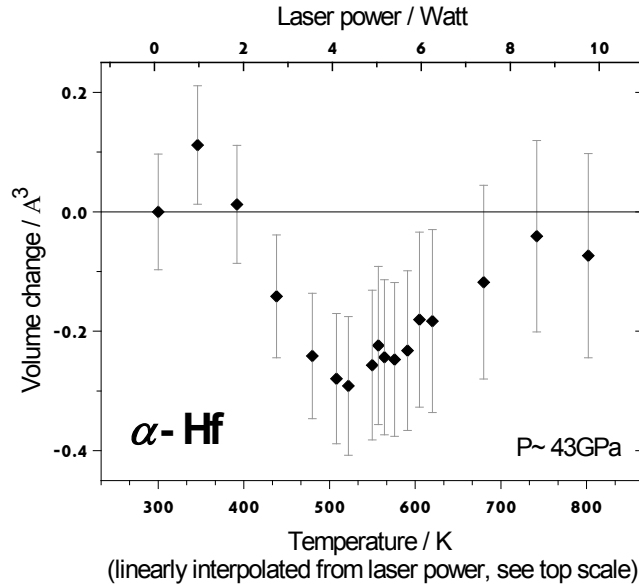
and ~600 K (Figure 1.22 b-c). This effect was observed in measurements acquired with resistive heating as well as with laser heating, Figure 1.22 b-c.



a)



b)



c)

Figure 1.22. Observed volume thermal expansion in Hf. a) 2-d intensity plots show a succession of integrated intensity vs. 2θ x-ray diffraction patterns collected at a succession of increasing temperature points. Each horizontal line in the 2-d intensity plot corresponds to a single x-ray diffraction pattern collected at a given temperature, insert shows a magnified view; b) resistively heated DAC data, α -hafnium volume change compared to volume at 300K, corrected for volume change due to pressure differences at different temperature points. c) Laser heated DAC data, α -hafnium volume change compared to volume at 300K, corrected for volume change due to pressure differences at different temperature points (During laser heating, temperature was estimated by linear interpolation from laser power).

Can there be negative thermal expansion in hexagonal metals at high pressure?

A small class of currently known materials has a thermal expansion coefficient which is negative in various temperature ranges. Commonly known negative thermal expansion (NTE) materials, the first of which had been accidentally discovered over a century ago, are compounds of two or more component elements (White, 1993). Nizhankovskii et al. (Nizhankovskii, 1994) first reported an anomalous negative thermal expansion in α -Ti along c -axis up to 170 K. However, NTE along all crystallographic directions has never been reported in pure elements at any temperature range. Liu et al.

(Liu et al., 2011) recently suggested NTE to occur in select pure elements under high pressure conditions. Volumes measured for α -hafnium in this study suggest that there is an NTE effect in Hf at high pressures (not a first order phase change but rather a continuous NTE in a single phase). Without further analysis, the results show that the volume thermal expansion coefficient is negative in α -hafnium above room temperature and up to around 600-700K under high pressure.

The anomalous negative thermal expansion at low temperatures for non-cubic single element solids has been known for quite some time (Munn, 1969). Nizhankovskii et al. (Nizhankovskii, 1994) first observed anomalous behavior of thermal expansion of *hcp* Ti at quite low temperature. First principle calculation studies (Nizhankovskii, 1994; Souvatzis et al., 2008) showed electronic topological transitions (ETT) in Ti and other non-cubic metals should lead to a singular anisotropic thermal expansion at temperature much lower than the Debye temperature. The results showed that the negative thermal expansion coefficient along the c-axis in Ti occurs roughly in a temperature range of 0 – 170 K, which is well below Debye temperature (i.e. 420 K). High pressure first principle calculation of the *hcp* Zn and Cd (Novikov, 1999) is also in agreement with their negative thermal expansion around 75 K (Munn, 1969). It was shown that an ETT can lead to a considerable softening of the shear moduli, less prominent but still noticeable anomalies in short-wavelength phonon modes, and change thermodynamic properties: heat capacity and thermal expansion. However the observed (apparent) negative thermal expansion behavior for Hf in the current study occurs above its Debye temperature of 252 K (Kittel and McEuen, 1996). Liu et al. suggest that the negative thermal expansion behavior originates from the contribution of high pressure, small volume phases with higher

entropy (Liu et al., 2011). The possibility of observation of the configuration of two phase with a Gibbs energy penalty of ΔG is proportional to $\exp(-\Delta G/RT)$. In high pressure $\Delta G/RT$ is low enough to generate significant probability to observe the lower volume configurations in the higher volume. They showed that based on the Clausius–Clapeyron equation, for solids with $\Delta V_m < 0$ and $\Delta S_m > 0$ such as Zr and Hf, negative slopes of two-phase equilibrium lines in their temperature-pressure (T - P) phase diagrams cause the negative thermal expansion behavior in high pressure and temperature.

One result of the theory is the prediction of anisotropic thermal expansion for non-cubic metals near an ETT at temperatures much lower than the Debye temperature. Expansion coefficients must in such cases be positive along one axis and negative along another (Nizhankovskii, 1994; Souvatzis et al., 2008), as was experimentally confirmed for α -Ti (Souvatzis et al., 2008) for $T < 165$ K. This might be important from the point of view of possible applications since it means that any non-cubic single-crystal metal in the immediate vicinity of an ETT should have a zero thermal expansion coefficient along some crystallographic direction at sufficiently low temperatures. Therefore new opportunities might appear in the search for new nonmagnetic Invar materials.

In one of the heating runs at 45 GPa, x-ray diffraction was collected after quenching the sample (i.e. rapidly shutting off the heating laser). In this case, the molar volume of the quenched α -phase of hafnium was considerably lower than the molar volume before heating (the pre- and post-heating pressures were not equal; volume difference due to unequal pressures was accounted for using known compressibility of α -hafnium). As can be seen in Figure 1.23, the apparent NTE in α -hafnium could be caused by a non-hydrostatic compression effect. Annealing the sample at elevated temperatures

stops the NTE effect and after a certain high temperature α -hafnium starts showing a positive volume thermal expansion. However, this explanation is suspect because even though hafnium and platinum were both loaded to the same pressure and heated to the same temperatures, only hafnium shows a contraction in volume during heating. Another apparent explanation for the observed results is the interdiffusion between platinum and hafnium. However, this explanation can be discounted because during several heating runs no platinum was used and decrease in volume of hafnium upon heating was observed nonetheless. Moreover, the apparent NTE up to 600 K was also observed in runs where neon was used as a pressure medium and resistive heating was used to reach high temperatures. Careful volume measurements using radial x-ray diffraction and determination of the non-hydrostatic stresses involved during compression of hafnium at high temperatures is probably needed to better understand whether the apparent NTE in hafnium is a real physical property of the material or an artifact of non-hydrostatic stress.

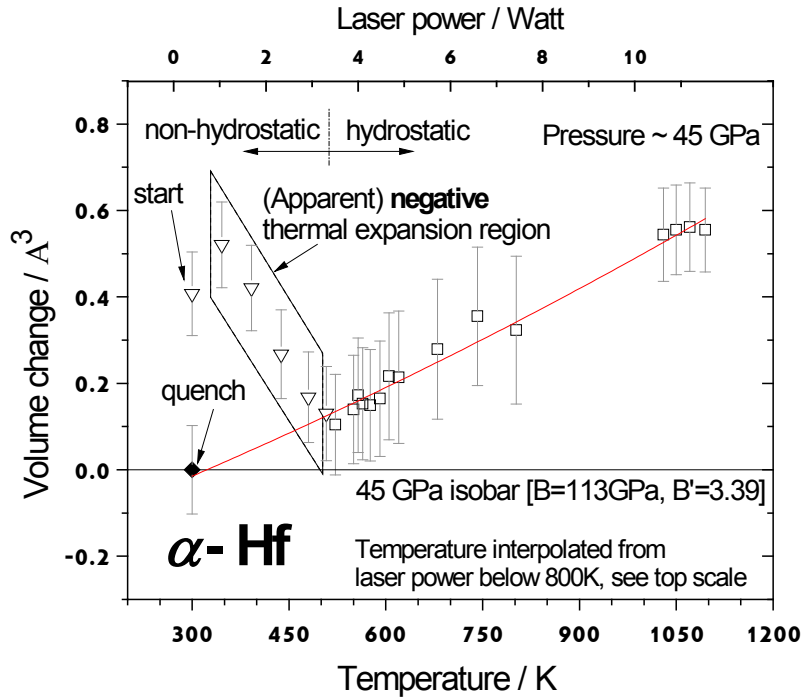


Figure 1.23. Pre vs. post heating molar volume of hafnium. Low unit cell volume of the quenched sample could be due to the fact that prior to heating, the sample is compressed non-hydrostatically.

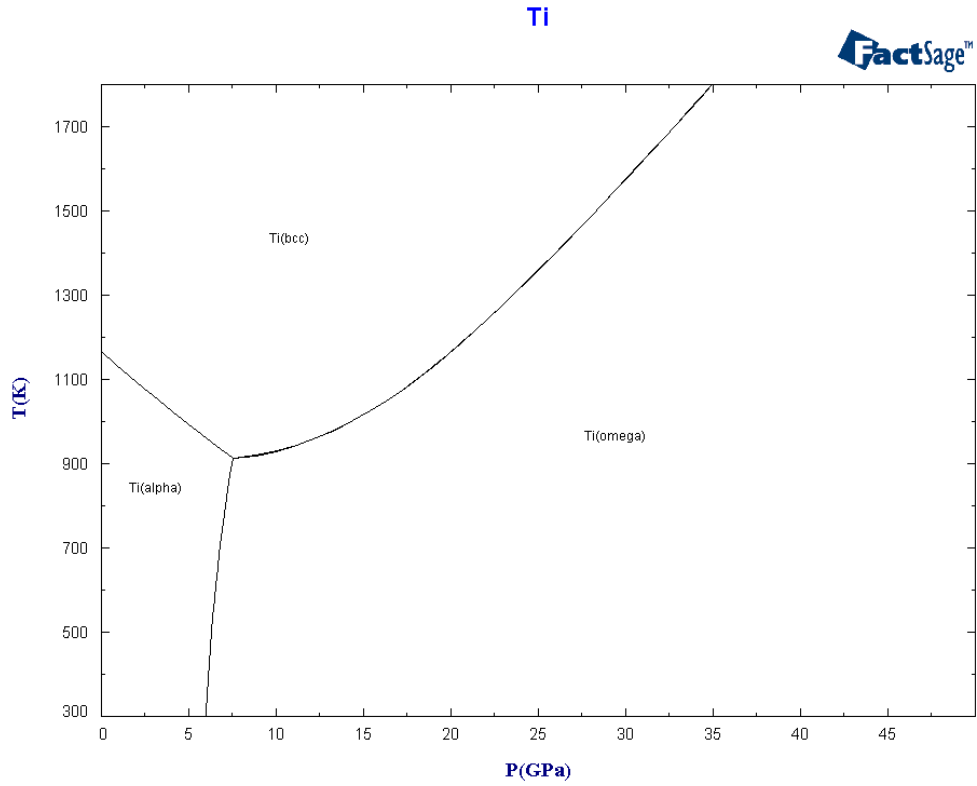
CALPHAD, Optimizer and Phase diagram calculations

As in the previous section, I used the *OptiSage* module of the *FactSage 6.2* thermodynamic software (Bale et al., 2009) as the tool for determining the multi-parameter *EoS*. *P-V-T* experimental data from the current study as well as ambient pressure thermal expansion data from the literature (Adenstedt, 1952; Touloukian et al., 1979a) were used as the sources of experimental data for determining the *EoS* parameters. In case of α -hafnium and its anomalous NTE phenomenon at high pressure, points at high temperature and volume of the quenched α -phase were given more weight in fitting of the *EoS*. The low temperature compression points were assumed to contain errors related to non-hydrostatic compression and were given low weight during fitting.

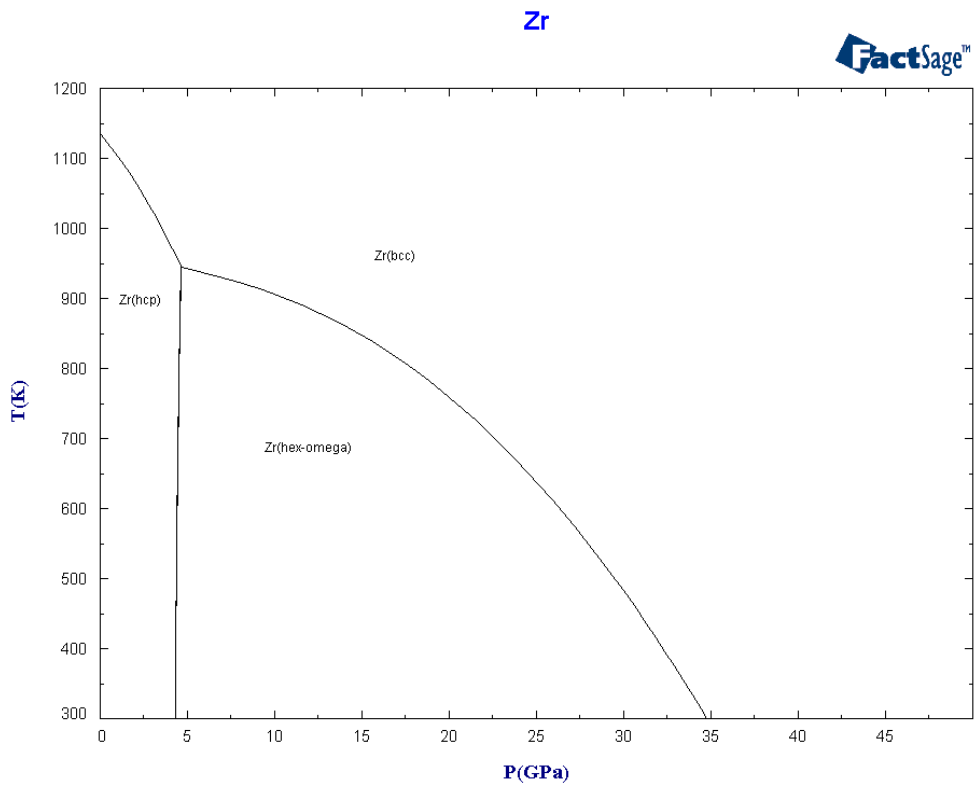
ChemSage software was used in conjunction with the EoS's determined in this study to extrapolate thermophysical properties for all solid phases of Ti, Zr and Hf at pressures up to 60 GPa and temperatures of up to 2500 K.

The software *OptiSage* was used to optimize all the parameters to minimize the error between experimental values and calculated values based on the CALPHAD compatible quasi-harmonic model described by Brosh et al. (Brosh et al., 2007). Optimized *EoS* parameters can be used as the input for *ChemSage* (Eriksson and Hack, 1990) or *FactSage* (Bale et al., 2009) thermodynamic software to calculate all thermodynamic properties at high *P-T* conditions. For readers who do not have access to either *ChemSage* or *FactSage* software, I include tabulated values of all thermodynamic and volume data for Ti, Zr and Hf at high pressures and temperatures in APPENDIX.

The calculated phase diagrams are inherently consistent with, and reproduce, the experimentally measured phase boundaries because experimental data on *P-T* conditions of phase equilibria are used as fitting variables in determining the EoS. The calculated phase diagrams for Ti, Zr and Hf up to various high *P-T* conditions are presented in Figure 1.24.



a)



b)

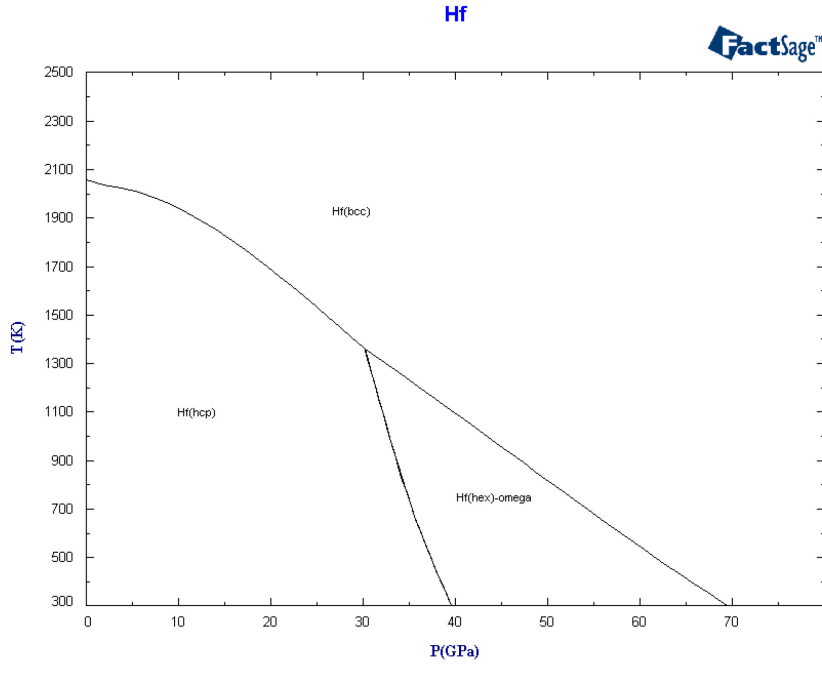
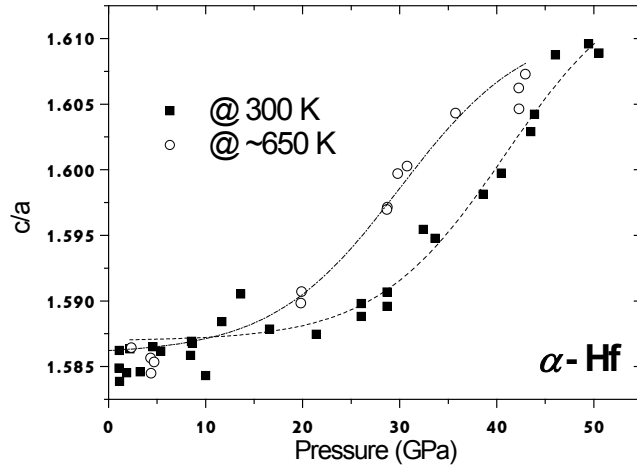


Figure 1.24. Calculated phase diagrams for a) titanium, b) zirconium, c) hafnium based on thermodynamically optimized experimental data

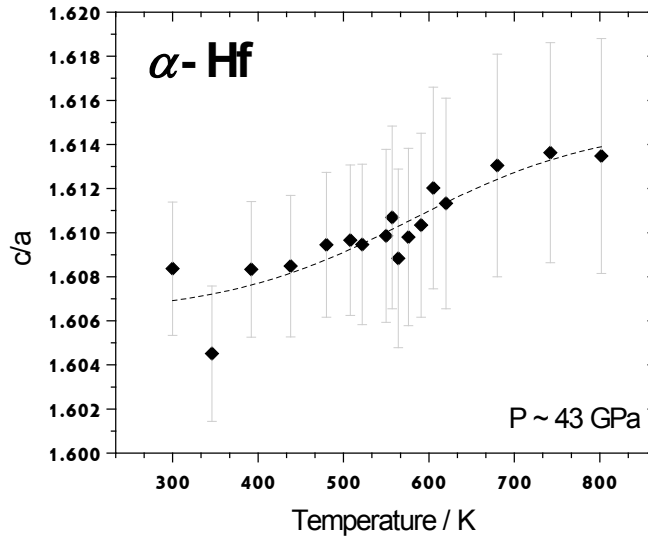
The calculated phase diagram for hafnium (Figure 1.23 c) shows an unexpected $dT/dP < 0$ topology of the $\alpha - \omega$ phase transition. The exact shape and slope of this phase transition curve was not measured experimentally and was not used during optimization of the EoS. This result comes spontaneously as an optimal calculated equilibrium which minimizes errors between the model and experimental data on molar volumes of α , β and ω phases (measured in this study) and standard thermophysical data on α and β phases of hafnium (available in literature). Thermophysical data for ω phase was not available because this phase is not stable at ambient pressure and therefore its thermophysical properties cannot be measured using standard calorimetric techniques. In fact, thermophysical properties (C_p , H , S , G) of the ω -phase of Ti, Zr and Hf were estimated during the optimization of the EoS parameters and are presented in this study for the first time. The $dT/dP < 0$ topology of the $\alpha - \omega$ phase transition is in contrast to previous

reports (Ostanin, 2000) which have proposed that the $\alpha - \omega$ phase in hafnium has $dT/dP > 0$ as in the cases of titanium and zirconium (elements in the same group in the periodic table).

The ratio c/a is a dimensionless measure of the spacing between basal planes in a hexagonal lattice. According our observations at room temperature, which were described in the previous section, the c/a ratio increases from an ambient pressure value of ~ 1.58 to ~ 1.61 at a higher pressure (Hrubiak et al., 2012). Because of this observation, I had suggested that the relative compressibility of a and c axes in α -hafnium is temperature dependent which could explain the lowering of the observed $\alpha \rightarrow \omega$ phase transition pressure at high temperatures. In this study I have measured the temperature effect on the c/a ration in α -hafnium by measuring the lattice parameters of hafnium at a single pressure and at many different points. The c/a ratio was indeed seen to increase with temperature as was predicted in my previous work.



a)



b)

Figure 1.25. a) same as Figure 1.8, shown again here for a comparison of pressure and temperature dependence of the c/a ratio in hafnium. c/a ratio increases from an ambient pressure value of ~ 1.58 to ~ 1.61 at a higher pressure (Hrubiak et al., 2012); b) the c/a ratio increase also increases with increasing of temperatures.

If the increase in the c/a ratio facilitates the α - ω phase transition in hafnium then the temperature and pressure dependence of the c/a ratio would support the independent thermodynamic calculations which suggest a negative dT/dP slope for the α - ω phase transition in hafnium.

Conclusion

Careful volume measurements using radial x-ray diffraction and determination of the non-hydrostatic stresses involved during compression of hafnium at high temperatures is probably needed to better understand whether the apparent NTE in hafnium is a real physical property of the material or an artifact of non-hydrostatic stress.

Optimized *EoS* parameters can be used as the input for *ChemSage* (Eriksson and Hack, 1990) or *FactSage* (Bale et al., 2009) thermodynamic software to calculate all thermodynamic properties at high *P-T* conditions. For readers who do not have access to either *ChemSage* or *FactSage* software, I include tabulated values of all thermodynamic and volume data for Ti, Zr and Hf at high pressures and temperatures in APPENDIX.

Unexpectedly discovered *P-T* dependence of the *c/a* ratio in α -hafnium is consistent with an independent result of thermodynamic calculations which produces a negative dT/dP slope for the α - ω phase transition in hafnium, contrary to previous reports (Ostanin, 2000).

1.04 Thermodynamics of several elements at high pressure

Introduction

CALPHAD compatible EOS based on Explicit Gibbs Free Energy concept was used to calculate the Gibbs free energy as a function of pressure and temperature for the solid state of ten important elements: V, Nb, Ta, Mo, W (Group VB and VIB), Pd, Pt (Group VIII B) and Cu, Ag and Au (Group IB). When compared to shock wave data, the modeled EoS holds well but the fit is not totally satisfactory in the ultra-high pressure range. A great advantage of this formulation is that it can be used to extrapolate thermodynamic properties such as heat capacity and entropy to very high temperatures and pressures.

Determination of EOS parameters

Cold compression parameters were calculated in the first step. Molar volume, bulk modulus and derivative bulk modulus in the reference condition were determined by the use of room temperature compression data. V_0 , B_0 and B_0' were calculated based on room temperature isostatic compression data, but shockwave data up to almost 500 GPa are presented for comparison. Einstein characteristic temperature θ_0 is the adjustable parameter of the equation and the other ambient condition parameters (i.e. γ_0 and δ_0) were calculated based on it. Brosh *et. al* (Brosh et al., 2007) used the constant value of 300 °K for simple elements and 500 °K for more complex compounds. Since the high temperature thermal expansion is influenced by some other terms like an-harmonic effect (Oganov and Dorogokupets, 2004), using the lower value of Einstein temperature eliminated the overestimation and helped to calculate more accurate parameters (Brosh, 2009). On the other hand, most of the transition metals, which are discussed here, are

diamagnetic and paramagnetic metals; hence, electronic and magnetic contributions to the specific heat in the temperature below 300 K are negligible. It was found that using the actual Einstein temperature could be more beneficial for extreme condition behavior. In this way, the Einstein temperature of the elements was calculated based on low temperature volumetric heat capacity (Girifalco, 2000). For simplicity, Debye temperature (Kittel and McEuen, 1996) or the Einstein temperature calculated from the Debye (Girifalco, 2000), can also be used as θ_0 . Gruneisen and Anderson-Gruneisen parameter are determined based on thermal expansion and bulk modulus data in the temperature slightly above the θ_0 . b_0 is assumed to be 1 for all the materials. The high temperature EOS parameters (i.e. δ_I and b_I) were calculated based on high temperature thermal expansion and bulk modulus data by simultaneously solving the equations 10 and 12. In some cases like Vanadium high temperature bulk modulus data is not available so b_I is assumed to be 1 and δ_I is adjusted by the use of the high temperature thermal expansion values. All calculated parameters are shown in table 1.

Calculated parameters are used as the input data for *ChemSage* (Eriksson and Hack, 1990) software to reproduce all thermodynamic properties.

Group VB: Vanadium, Niobium and Tantalum and Group VIB: Molybdenum and Tungsten

The body-centered cubic (*bcc*) transition metals (i.e. molybdenum (Mo), tantalum (Ta), tungsten (W), Niobium (Nb) and Vanadium (V)) are especially interesting, because they have very high melting points at ambient pressure and, in addition, at room temperature they remain in a stable *bcc* structure up to extremely high pressures (i.e. tungsten up to 378 GPa (Ruoff et al., 1990), molybdenum 416 GPa (Ruoff et al., 1990;

Cynn and Yoo, 1999), tantalum 170 GPa (Cynn and Yoo, 1999), niobium 134 GPa (Takemura and Singh, 2006) and vanadium 69 GPa (Ding et al., 2007; Verma and Modak, 2008)). Total energy calculations for W by Moriarty (Moriarty, 1992a) predict the *bcc* structure to be stable to 1250 GPa in room temperature and about 11000K at ambient pressure. These make the tungsten an appropriate target for high *P-T* study. In addition to tungsten's technological importance, strong x-ray diffraction signal, and high yield strength, it was chosen for several studies and has been widely examined in dynamic and static compression experiments.

The heat capacity (Anderson, 1936; White and Colloco, 1984; Guillermet and Fernandez Guillermet, 1985; Takahashi and Nakamura, 1996), bulk modulus (Bolef and De Klerk, 1962; Featherston and Neighbours, 1963; Lowrie and Gonas, 1967; Bolef et al., 1971; Hubbell and Brotzen, 1972; Leisure et al., 1973; Bujard et al., 1981; Saxena and Zhang, 1990; Gülseren and Cohen, 2002), molar volume and thermal expansion (Nix and MacNair, 1942; Edwards et al., 1951; Amonenko et al., 1963; Dutta and Dayal, 1963a; Ross and Hume-Rothery, 1963; Vasyutinskii et al., 1966; Westlake and Ockers, 1970; Waseda et al., 1975; Touloukian et al., 1979b; Pialoux et al., 1982; Dubrovinsky and Saxena, 1997; Wang and Reeber, 1998) of Group VB and VIB elements have been measured enormously; complete review of thermal expansion experimental data is provided by Wang et al. (Wang and Reeber, 1998) and Lu et al. (Lu and Chen, 2009). Prediction of the V_m and B_T with the proposed EoS and Dorogokupets et al. (Dorogokupets and Oganov, 2007) semi-empirical EoS as well as their experimental data are shown in Figure 1.26 and Figure 1.27. One of the important limitations of the proposed model is the overestimation of the bulk modulus at high temperatures to avoid

mechanical instability in high temperature (Brosh et al., 2007). As it can be seen the calculated B_T cross over the experimental data in high T and overestimate the modulus. On the other hand, for Mo and W and other early transition elements, the anharmonic contributions to entropy and energy are higher than Cu, Ag and Au (Guillermet and Grimvall, 1991; Wallace, 1997) . Because of this, for better prediction results explicit modeling of anharmonicity can be introduced. As it can be seen high temperature predicted data for Mo, Nb and V has about 3% error in comparison to experimental data. Volumetric experimental data of Ta has about 10% diversity in high T . While calculated data is consistent with data from Wang et al. (Wang and Reeber, 1998), it is about 1.5% lower than data from Touloukian et al. (Touloukian et al., 1979b). As mentioned before, the high temperature bulk modulus data is not available for vanadium, but it can be seen that calculated δ_1 is good enough to predict the thermal expansion data.

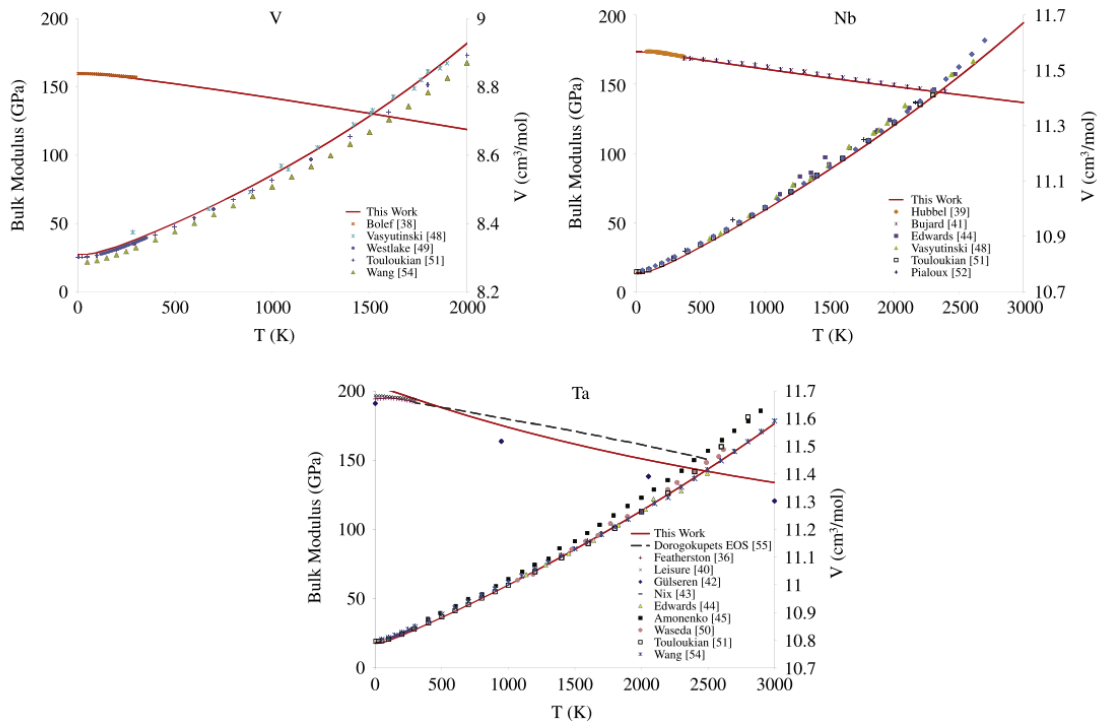


Figure 1.26. Calculated molar volume and bulk modulus from this work for V, Nb, and Ta. Calculated bulk modulus data from Dorogokupets et al. and experimental data are also shown. (Karbasi, Saxena, and Hrubiak, 2011)

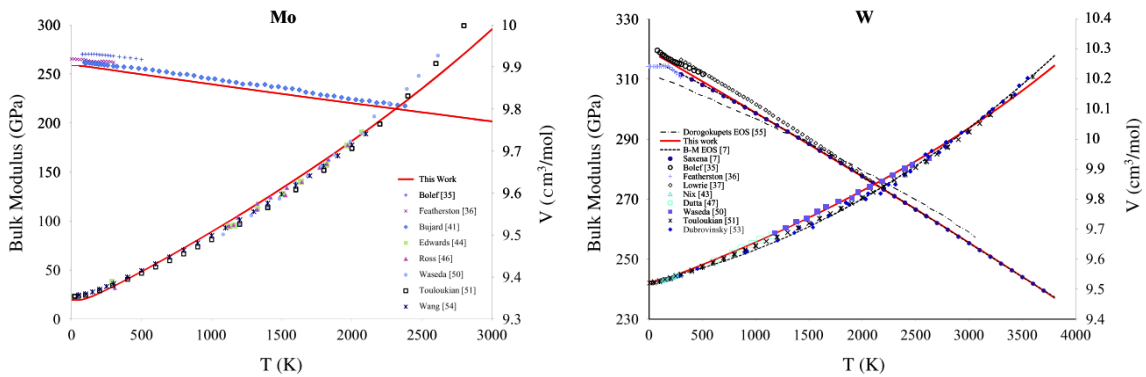


Figure 1.27. Calculated molar volume and bulk modulus from this work for Mo and W. Calculated bulk modulus data from Dorogokupets et al., molar volume and bulk modulus from the Birch-Murnaghan EoS and experimental data are also shown (Karbasi, Saxena, and Hrubiak, 2011).

Room temperature compression is shown in Figure 1.28 and Figure 1.29. As it can be seen, calculated isotherms are consistent with static compression experimental data (Mao et al., 1978; Cynn and Yoo, 1999; Dewaele et al., 2004; Nakamoto et al., 2005; Takemura and Singh, 2006). V, Nb and Ta calculated isotherms are 5-10% lower than shock wave data (McQueen and Marsh, 1960; Krupnikov et al., 1963; McQueen et al., 1970; Ming and Manghnani, 1978; Marsh, 1980; Al'tshuler et al., 1981; Mitchell and Nellis, 1981; Gathers, 1986; Hixson and Fritz, 1992; Moriarty, 1992b). It can be attributed to the nature of shock wave experiments; Holzapfel (Holzapfel, 2010b) shows that only the fitted equation without any physical meaning can express the reduced shock wave data completely.

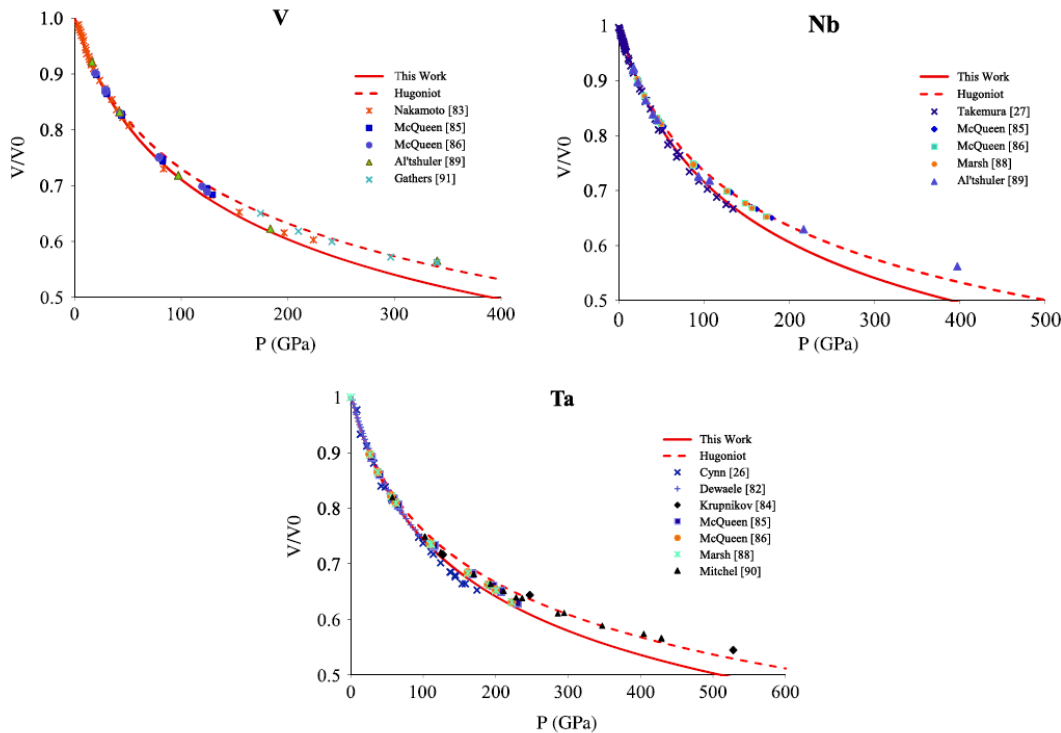


Figure 1.28. Calculated cold compression and Hugoniot curves for V, Nb, and Ta as well as their experimental data (Karbasi, Saxena, and Hrubciak, 2011).

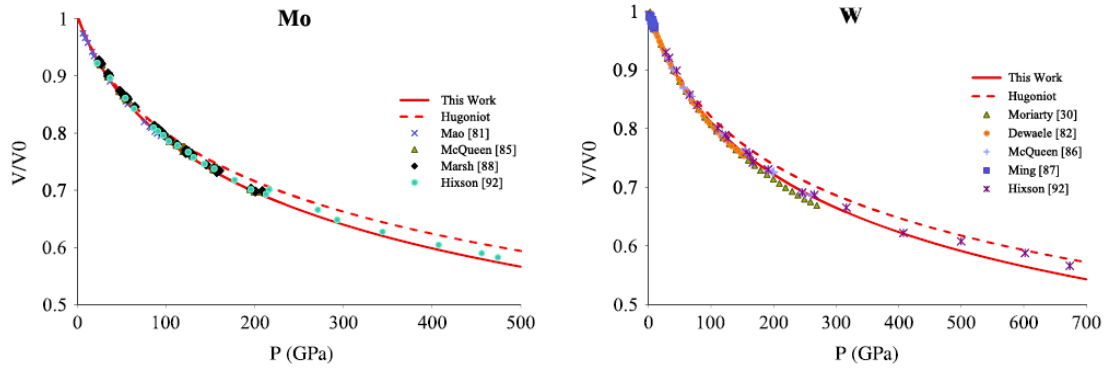


Figure 1.29. Calculated cold compression and Hugoniot curves for Mo and W as well as their experimental data (Karbasi, Saxena, and Hrubciak, 2011).

In addition to that, P - V isotherm of the Ta, Mo and W in 1000 and 3000 K, based on the proposed calculation and data from (Hixson and Fritz, 1992; Dorogokupets and Oganov, 2006) are shown in Figure 1.30. Experimental data (Miller et al., 1988; Asimow et al., 2009) of Mo in 1673 K and its calculated P - V curve is also shown in Figure 1.31. Even though proposed data overestimate the volume in high P ($P > 200$ GPa) about 1% in comparison to other EoS, calculated isotherm of Mo in 1673 K is almost identical with the experimental data.

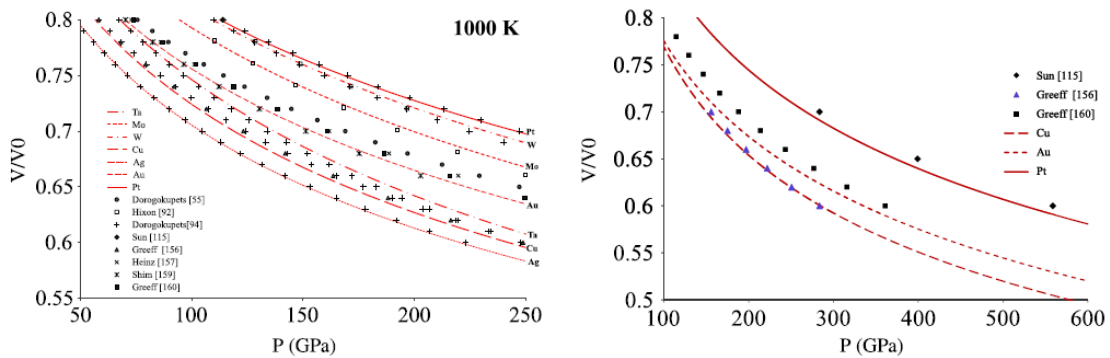


Figure 1.30. Calculated isotherm for various elements, (a) 1000K isotherm for Ta, Mo, W, Cu, Ag, Au, and Pt. (b) 5000 K isotherm for Cu, Au, and Pt. Calculated data are also presented for comparison (Karbasi, Saxena, and Hrubciak, 2011).

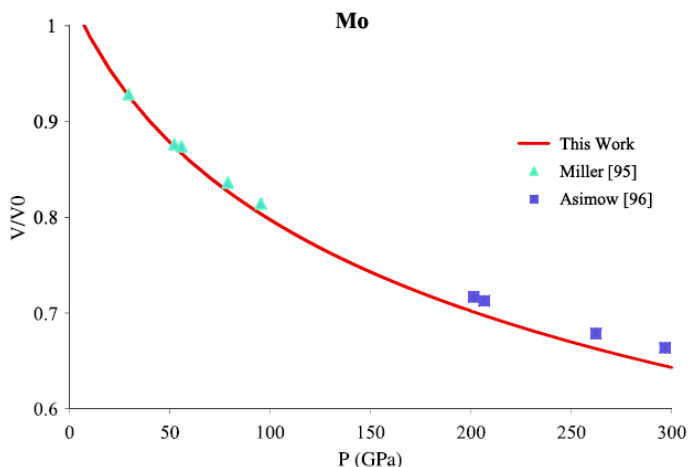


Figure 1.31. Comparison of calculated isotherms of Mo at 1674 K with experimental data (Karbasi, Saxena, and Hrubciak, 2011).

Melting

Despite a large number of experimental and theoretical efforts (Fateeva and Vereshchagin, 1971; Hixson et al., 1989; Moriarty, 1994; Errandonea, Schwager, et al., 2001b; Errandonea et al., 2003; Ross et al., 2004, 2007; Verma, 2004; Errandonea, 2004a, 2005, 2006; Cazorla et al., 2007; Cazorla, Gillan, Taioli, and Alfè, 2008; Luo and Swift, 2007; Taioli et al., 2008; Xi and Cai, 2008; Xiu-Lu, 2008; Zhang, Liu, et al., 2008; Liu, Zhang, et al., 2008; Santamaria-Perez et al., 2009), agreement on the melting behaviour of Mo, Ta, and W at high pressure has been elusive. The first shock wave experiment on high pressure melting of Mo done by Hixson et al. (Hixson et al., 1989) up to 350 GPa, followed by early work of Moriarty (Moriarty, 1994) employed a many-body total energy function to predict the high pressure melting curve of Mo. Debates about the melting curve of early transition metal (i.e. groups VA and VIA of the Periodic Table) starts with the Errandonea et al. (Errandonea, Schwager, et al., 2001b) DAC melting experiments. While Shock wave data reveal the high pressure and temperature melting

point (~ 380 GPa and ~ 1000 K), DAC shows low melting slope $dT_m/dP \approx 0$. Extrapolation of DAC data up to 350 GPa almost predict the melting temperature about 4000 K which is far below shock wave data. Mo is unique, only because it has been examined extensively because it has the smallest measured melting slope of that group, and thus provides the most severe test. Ta and W, while less fully examined by shock experiments, appear to have many of the same features as Mo. The fact that unusually low melting slopes have also been found in the early transition metals Ta, W, Cr and V indicates that the present results are a general feature of the early transition metals and not confined to Mo. Theoretical work (Moriarty, 1994; Belonoshko et al., 2004; Cazorla et al., 2007; Cazorla, Gillan, Taioli, and Alfe, 2008; Xi and Cai, 2008) based directly or indirectly on density functional theory (DFT) generally supports the shock data. While the Moriarty (Moriarty, 1994) calculation overestimate the shock wave experiment, Belonoshko et al. (Belonoshko et al., 2004) with dislocation-mediated melting model underestimate the results. Cazorla et al. (Cazorla et al., 2007; Cazorla, Gillan, Taioli, and Alfe, 2008) used the *ab initio* using the DFT with simulations of coexisting solid and liquid and calculated the melting curve, which is consistent with shock data. They found out that Mo melts in high pressure at $P \approx 380$ GPa and $T_m \approx 8650$ K, which is in a good agreement with recent experimental shock wave data (Xiu-Lu, 2008), $P \approx 3740$ GPa and $T_m \approx 7853 \pm 813$ K.

Ross et al. (Ross et al., 2004) argue that change of coordination on going from *bcc* solid to liquid leads to a change of electronic structure, and hence a change in the electron distribution between *s-p* and *d* states, and that this redistribution stabilizes the liquid and lowers T_m . Errandonea (Errandonea, 2005) argue that *ab initio* calculations neglect the rearranging of the electronic structure upon melting and this may be a possible cause for

the large melting temperatures obtained from *ab initio* calculations, since these calculations do not take into account the free-energy changes produced by alterations of the *d*-electron band. Ross et al. (Ross et al., 2004) used a semi-empirical model in which the *d*-band contribution to the total binding energy is described by the Friedel equation and showed that omission of *d*-band physics results in a large overestimation of the melting slope of *bcc* transition metals. The melting curve obtained using that model satisfactorily agrees with the vacancy model estimates and the DAC measurements (Errandonea, 2005). Santamaría-Pérez et al. (Santamaria-Perez et al., 2009) used static DAC measurements and Poisson ratios from shock experiments (Hixson et al., 1989), and proposed a new phase diagram for Mo. In this diagram the *bcc* phase extends at 3250 K to 150 GPa, the pressure at which a transition from *bcc* to a new non-crystalline phase happens, possibly close to the A15 structure. A15 is known to compete favorably with *bcc*, for the early transition elements Mo, Nb, Ta, and W (Berne et al., 1999). Above 150 GPa, the melt is a solid-liquid mixture bounded roughly by a transition region extending from 150 GPa (4100 K) to 390 GPa (~10 000 K). On the other hand, Cazorla et al. (Cazorla et al., 2007) considered all the *s-p* to *d* electron transfer effects and changes of *d* bandwidth in their simulations. They have shown that there are only minor changes of both atomic and electronic structure in going from the high-temperature *bcc* solid to the melt and transfer of electrons from *s-p* states to *d* states appears to be incompatible with the present DFT calculations. Low melting slope in Ross et al. (Ross et al., 2004) calculation could be due to the perfect crystal assumption for the high temperature solid and liquid phases. Cazorla et al. (Cazorla, Gillan, Taioli, and Alfe, 2008) also showed that *bcc* crystal structure is the most favored up to 350 GPa (~8650 K). Disagreements

with DAC measurements on Mo and other transition metals are a cause for concern. A major disagreement between DFT predictions and experimental data suggests an unexpected failure either of commonly used DFT approximations, or of apparently well-established experimental techniques.

Group VIIB: Pt and Pd

Low temperature heat capacity data of platinum and palladium are from (Crangle and Smith, 1962; Feldman and Horton, 1965; Shoemaker and Rayne, 1968; Furukawa et al., 1974; Rupp and Birringer, 1987), recommended values for the thermal expansion of Pt and Pd were gathered from (Owen and Yates, 1934; Edwards et al., 1951; Dutta and Dayal, 1963a; Rao and Rao, 1964; Schröder et al., 1972; Touloukian et al., 1979b; Kirby, 1991). High temperature elastic data is not widely available for Pt and Pd. Rayne (Rayne, 1960), Weinmann et al. (Weinmann and Steinemann, 1974) and Collard et al. (Collard and McLellan, 1992) data are used. Low temperature ($T < 100\text{K}$) bulk modulus data of palladium shows some anomaly, as shown in Figure 1.32, which can be attributed to the change with temperature of the contribution to the shear constants, resulting from the holes in the 4d band of palladium (Rayne, 1960). The results of volumetric thermal expansion and bulk modulus are shown in Figure 1.32.

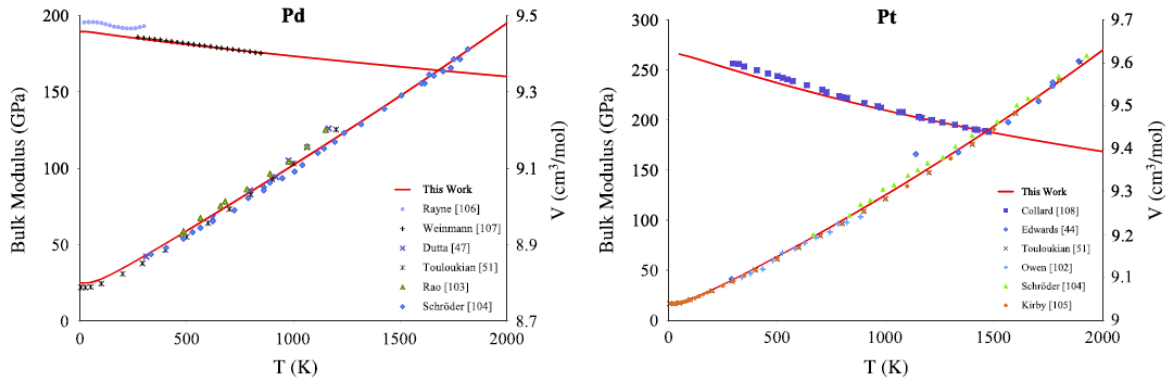


Figure 1.32. Calculated and experimental data of molar volume and bulk modulus for Pd and Pt (Karbasi, Saxena, and Hrubciak, 2011).

Platinum and Palladium have a face-centered cubic (*fcc*) crystal structure and do not have any phase changes between absolute zero and their melting points. Theoretical calculations (Ahuja et al., 1994; Jeong and Chang, 1999; Singh, 1999) and experimental results (Kavner and Jeanloz, 1998) also confirmed the stability of *fcc* crystal structure in high pressure. Although platinum is a widely used high-pressure standard due to its chemical inertness and large isothermal compressibility, there isn't a lot of attention to palladium.

First room temperature equation of state of Pt was established by reducing shock Hugoniot and *ab initio* LMTO up to 660 GPa (McQueen et al., 1970; Morgan, 1974; Holmes et al., 1989). While equation of state developed by Holmes et al. (Holmes et al., 1989) showed some discrepancy in the results, Dewaele et al. (Dewaele et al., 2004) found Holmes et al. EoS overestimating pressure by ≈ 4 GPa near 100 GPa at room temperature. Sun et al. (Sun et al., 2008) found out their room temperature isotherm is almost identical with that of Holmes et al., below 70 GPa. At high pressures ($P > 200$ GPa) Holmes et al. (Holmes et al., 1989) overestimate the results about 3%. Figure 1.33

shows the calculated cold compression and Hugoniot curves of palladium and platinum as well as the experimental results. As it can be seen, the calculated cold compression is completely identical to Dewaele et al. (Dewaele et al., 2004), but about 5% lower than high-pressure shock wave data (Morgan, 1974; Holmes et al., 1989).

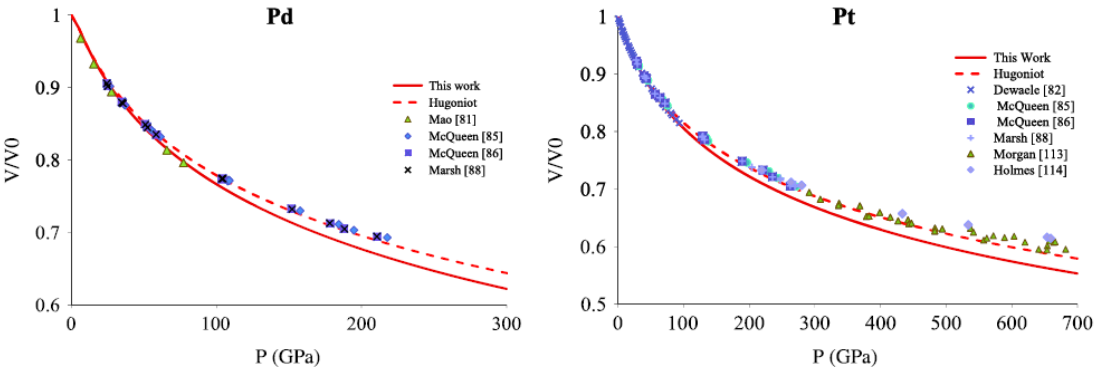


Figure 1.33. Calculated cold compression and Hugoniot curves for Pd and Pt as well as their experimental data (Karbasi, Saxena, and Hrubciak, 2011).

Besides the room-temperature isotherm, accurate thermal pressure data is needed to calibrate pressure in simultaneous high-pressure and high-temperature experiments. P_{th} can't be easily determined experimentally in the wide range of temperature and volume; so theoretical approach combined with the experimental data is the best way to construct thermal EoS for temperature-pressure calibration (Fei et al., 2004; Xiang et al., 2005; Zha et al., 2008). Comparison of the high temperature compression of platinum with experimental data and theoretical calculation is shown in Figure 1.30. The calculated data based on the proposed equation of state is identical with the density-functional theory calculation (Sun et al., 2008) and semi-empirical EoS (Dorogokupets and Oganov, 2006) up to 5000 K. In addition, the calculated 1900 K isotherm shown in Figure 1.34 is also consistent with experimental data.

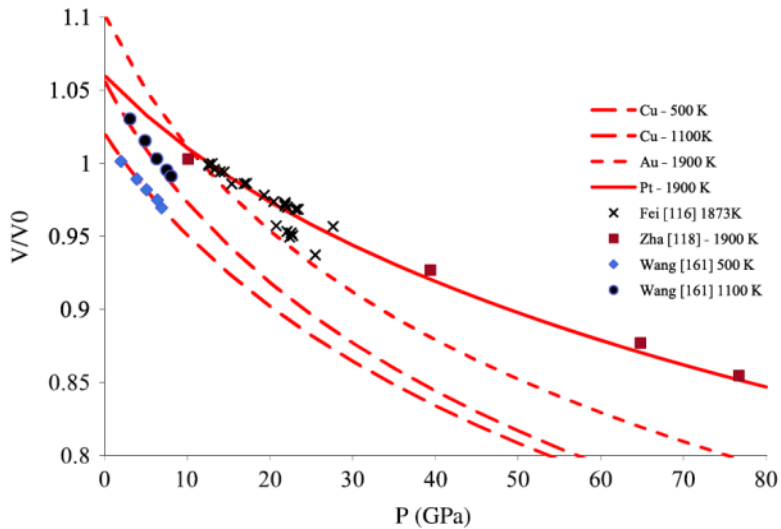


Figure 1.34. Comparison of calculated isotherms of Cu at 500 and 1100 K, Au at 1900 K, and Pt at 1900 K with experimental data (Karbasi, Saxena, and Hrubiak, 2011).

Group IB: Copper, silver and gold

Copper, silver and gold are in the same column of the periodic table; each of them possesses one *s*-orbital electron on top of a full electron shell. This similarity in electronic configuration endows these metals with similar physical properties such as remarkable electrical conductivity. The EoS parameters for Cu, Ag and Au are gathered from (Scheel, 1921; Owen and Yates, 1934; Hume-Rothery and Reynolds, 1938; Meads et al., 1941; Esser and Eusterbrock, 1941; Giaquie, WF, Meads, 1941; Nix and MacNair, 1942; Geballe and Giaquie, 1952; Overton and Gaffney, 1955; Walsh et al., 1957; Al'tshuler et al., 1958; Spreadborough and Christian, 1959; McQueen and Marsh, 1960; Simmons and Balluffi, 1960, 1962, 1963; Dutta and Dayal, 1963b; Chang and Hultgren, 1965; Chang and Himmel, 1966; Rolfe, 1966; Thiel and Kusubov, 1966; Kantola and Tokola, 1967; *Hugoniot equation of state measurements for eleven materials to five megabars*, 1968; Vermaak and Kuhlmann-Wilsdorf, 1968; Gehlen, 1969; McQueen et al., 1970; Mao et

al., 1978; Touloukian et al., 1979b; Mitchell and Nellis, 1981; White and Colloco, 1984; Rupp and Birringer, 1987; Suh et al., 1988; Collard and McLellan, 1992; Holzapfel et al., 2001; Takemura, 2001). Comparison of the experimental volumetric thermal expansion and bulk modulus in different temperature data and theoretical predictions from the proposed equation of state and semi-empirical EoS of Dorogokupets et al. (Dorogokupets and Oganov, 2007) and Debye–Grüneisen model of Lu et al. (Lu and Chen, 2009) are shown in Figure 1.35. It can be seen that the present model successfully predicts volumetric and bulk modulus data. In the case of Cu, the model proposed by Lu et al. (Lu and Chen, 2009) underestimate the volumetric data in temperature lower than 100 K but has better consistence with the experimental results in high T . Both calculated data (Dorogokupets and Oganov, 2007; Lu and Chen, 2009) have better correlation with low temperature bulk modulus experimental data, while overestimate the data in high T , where the proposed model which is proposed here has better consistency.

Cu and Au remain in a *fcc* structure up to pressures higher than 100 GPa. While Ahuja et al. (Ahuja et al., 2001) predicts the phase transformation in gold at room temperature about 240 GPa, Söderlind (Söderlind, 2002) argued that the only transformation in gold occurs at about 2 TPa. Theoretical calculation of the electronic structure of Cu (Greeff et al., 2006) also does not show any phase transformation up to quite high pressure. High-pressure crystal stability of Cu and Au make them good candidates for a high-pressure calibration standard. Several mathematical EoS have been formulated (Heinz D, 1984; Batani et al., 2000; Shim et al., 2002; Greeff and Graf, 2004; Greeff et al., 2006) to predict their P - V - T behavior.

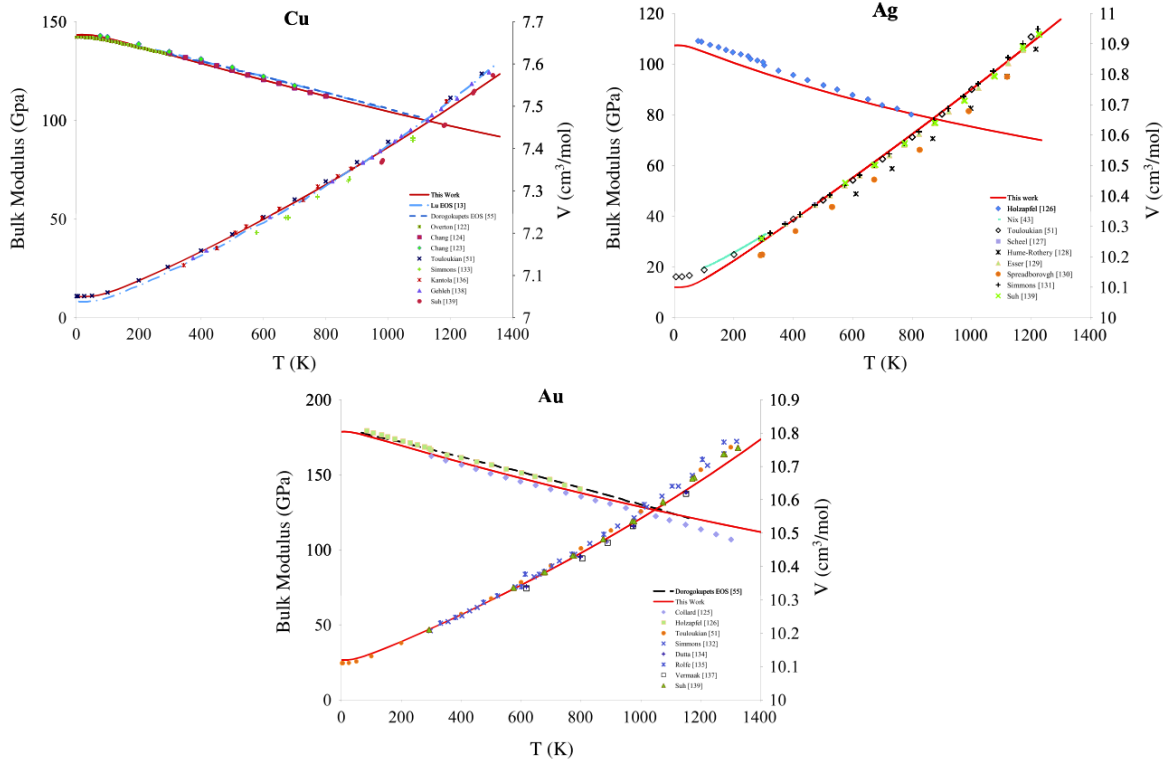


Figure 1.35. Calculated molar volume and bulk modulus from this work for Cu, Ag, and Au. Calculated bulk modulus data from Dorogokupets et al., molar volume and bulk modulus from Lu et al. EoS (Lu EoS) and experimental data are also shown (Karbasi, Saxena, and Hrubciak, 2011).

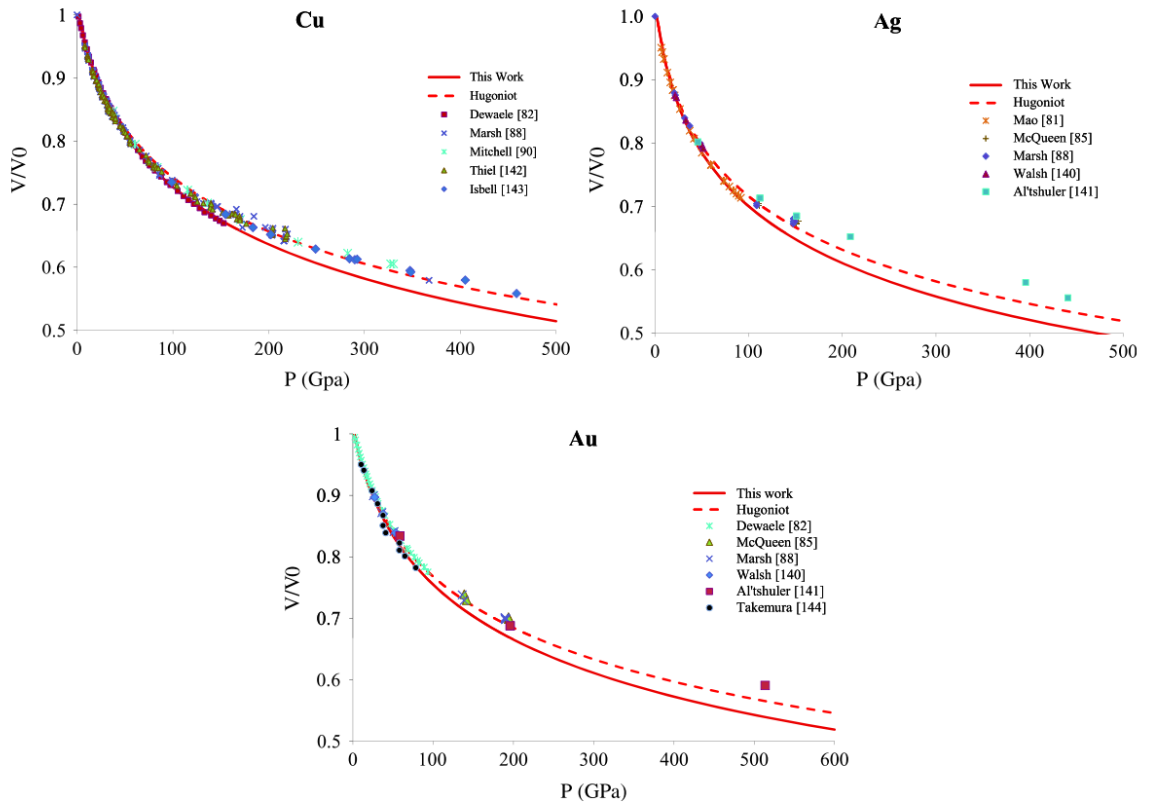


Figure 1.36. Calculated cold compression and Hugoniot curves for Cu, Ag, and Au as well as their experimental data (Karbasi, Saxena, and Hrubciak, 2011).

High P isotherms of Cu, Ag and Au for the present EoS and the other calculated and experimental data (Fei et al., 2004; Dorogokupets and Oganov, 2006, 2007; Greeff et al., 2006; Wang et al., 2009) are shown in Figure 1.35. It is clear that theoretical prediction of the present EoS is almost identical to the data of Dorogokupets et al. (Dorogokupets and Oganov, 2006, 2007) Greeff et al. (Greeff and Graf, 2004; Greeff et al., 2006) up to 5000 K and 500 GPa. The room temperature compression data up to 500 GPa is also shown in Figure 1.36, while the results are consistent up to 200 GPa. Holzapfel (Holzapfel, 2010a) recently showed that in the shock wave data of Cu, Ag and Au, typically 2–5% lower pressures are seen on almost all shock wave reduced isotherms at 200 GPa. He argued that, the shock-compressed solid just before melting may be

strongly disordered with disorder entropy similar to the entropy of melting and it can cause some discrepancy in high P data.

Melting

One of the first high pressure melting experiment of Cu, Ag and Au was done by Cohen et al. (Cohen and Kennedy, 1966) up to 4 GPa and followed by the work of Mitra et al. (Mitra et al., 1967), who extended the range to 7GPa for platinum as well as copper, gold and silver. The most recent melting experiments were done by Errandonea (Errandonea, 2010) up to 12 GPa. Electronic configuration of Cu, Ag and Au suggests that, their behavior is quite like a noble gas and follows the same trend showing a very steep melting curve. Similarities in properties of Group IB elements have led the experimental investigations to focus more on Cu as a model (Japel et al., 2005; Brand, H et al., 2006; An et al., 2008). In contrast to early transition elements (i.e. Mo, Ta and W) DAC and shock wave melting experiments are in good agreement with the theoretical calculation. However, there is a slight temperature offset between the calculated values and the experiments, due to technical difficulties of experiments and the inherent error associated with the calculations (Hung et al., 1997; Jeong and Chang, 1999; Belonoshko et al., 2000; Moriarty, 2002; Ono et al., 2008).

Several of the determined EoS parameters are shown in Table 1.4. Calculated parameters are used as the input data for Chem-Sage (Eriksson and Hack, 1990) software to reproduce all thermodynamic properties. In the case of Ti, Zr, Hf – phase diagrams containing α - ω - β phases at high P - T can also be reproduced using the determined EoS parameters. Tables with complete list of EoS parameters are included in the APPENDIX.

Table 1.4. EoS parameters for the thirteen transition elements.

	Z	H (298.15K) J/mol	S (298.15K) j/mol-K	V_m (0K, 1bar) cm ³	B_0 GPa	B_0'	Debye T K	γ_0	δ_0
Group IVB									
Ti α	22	0.00	30.759	10.619	103.39	4.00	250	0.83	0.85
Ti ω	22	2202.66	31.000	10.132	91.08	2.80	238	1.48	1.31
Ti β	22	6857.76	38.112	10.362	117.80	6.61	277	0.53	4.32
Zr α	40	0.00	38.869	14.039	98.60	3.50	250	0.71	1.45
Zr ω	40	957.43	39.269	13.865	84.01	3.44	250	1.04	3.00
Zr β	40	4814.72	43.199	13.904	84.85	2.50	250	0.71	1.45
Hf α	72	0.00	43.560	13.424	102.98	3.90	250	1.17	6.37
Hf ω	72	4315.85	45.208	13.326	106.01	3.42	250	0.91	2.27
Hf β	72	18684.21	61.104	13.666	92.64	2.54	250	1.59	5.00
Group VB									
V	23	0.00	28.936	8.310	162.00	3.50	272	1.39	4.10
Nb	41	0.00	36.464	10.770	168.80	3.30	300	1.54	3.61
Ta	73	0.00	41.471	10.790	192.00	3.69	161	1.56	8.80
Group VIB									
Cr	24								
Mo	42	0.00	28.605	9.345	243.00	4.57	274	1.71	4.09
W	74	0.00	32.660	9.525	296.00	4.40	232	1.64	4.15
Group VIIIB									
Ni	28								
Pd	46	0.00	37.823	8.879	183.00	5.28	202	2.40	2.40
Pt	78	0.00	41.631	9.040	279.00	5.03	179	2.67	10.89
Group IB									
Cu	29	0.00	33.164	7.050	133.41	4.90	230	1.78	5.97
Ag	47	0.00	42.677	10.100	99.32	5.89	164	2.64	6.08
Au	79	0.00	47.497	10.120	167.00	5.31	129	2.40	8.56

2. Exploring thermal conductivity of metals at extreme conditions

2.01 Introduction

Thermal transport properties

Thermal transport properties, the properties of a material that indicate its ability to conduct heat, are important quantities in many areas of materials science and engineering.

Thermal conductivity (k) is defined by

$$q = k\nabla T \quad \text{EQ. 2-1}$$

where q is the heat flux and ∇T is the temperature gradient. The time dependent equation for temperature in a system involving conduction of heat is

$$\nabla^2 T - (\rho C_p / k) \partial T / \partial t = 0 \quad \text{EQ. 2-2}$$

where ρ is the density, C_p is heat capacity at constant pressure (P), and t is time. For well over one hundred years researchers were occupied with this equation on two separate fronts. One is finding solutions to this equation and the other – developing ways to measure or calculate k for various materials at various temperature and pressure conditions (Ross et al., 1984).

Study of k at high pressures is interesting from a fundamental point as well as for its many cross-disciplinary applications in study of high-energy materials physics, ge-materials and any other cases where materials are subjected to very high pressures and temperatures. Fundamentally, measurements of k provide tools for testing of theories which try to predict its dependence on P and T . Many solid materials occur in different crystal structures depending on P - T conditions, and theories which predict k for different crystal structures can be tested with experimental measurements.

Thermal conductivity and thermal diffusivity (D) which are related by the expression

$$D = \frac{k}{C_P \rho} \quad \text{EQ. 2-3}$$

In electrical insulator materials, heat is mainly transported by phonons, i.e. lattice thermal conductivity (k_{lat}). In metals heat conduction occurs through phonons as well as electrons. Total thermal conductivity in metals is therefore a sum of k_{lat} and a contribution from the electronic thermal conductivity (k_{el}), $k = k_{\text{lat}} + k_{\text{el}}$. Electronic contribution for metals at high temperatures and high pressures can be estimated from its close to linear relationship to electrical resistivity (Ross et al., 1984), and lattice contributions can be extrapolated to high pressures using various vibrational models, several of which have been summarized by Hofmeister (Hofmeister, 2007). However, experimental measurements of k for materials (except for relatively few geo-materials) at simultaneous high pressures and temperatures are still virtually non-existent.

Conventional thermal conductivity measurements are obtained through a number of different techniques. All techniques to measure thermal conductivity can be into two types – contact and contactless methods. Contact methods generally involve a heat source and/or a thermocouple in direct physical contact with the sample. A temperature-varying heat source with a given frequency (e.g. resistively heated wire) is placed on one side of a specimen and temperature oscillations are recorded on the other end or at several points using a thermocouple. The single-contact method is a variation of the contact based techniques whereas the heat is supplied without physical contact with the source. However, the temperature measurements are still performed using contact thermocouples.

Experimental errors in contact based techniques tend to severely underestimate thermal conductivities due to thermal contact resistance (Hofmeister, 2007).

Most non-contact methods are derived from the Flash technique described by Parker (Parker et al., 1961). The flash technique involves a thin plate made from a sample of material, a source of heat (usually a pulse laser), and a means to measure the temperature of the sample in a time-resolved fashion (e.g. an infrared detector). The front side of the thin plate is irradiated with a short pulse of energy from a laser. The thermal energy travels through the thickness of the plate and a temperature rise is monitored on the back side of the plate. Time transient measurements of the temperature of the back side of the plate can be used to obtain the thermal diffusivity of the sample material (Parker et al., 1961). Thermal conductivity (k) can be calculated from Flash

measurements using $D = \frac{k}{C_p \rho}$ EQ. 2-3 above. Flash based techniques and other

time transient techniques (i.e. involving a heat source with power that varies over time) require that certain assumptions be made about temperature and pressure dependences of specific heat (C_p) and density (ρ) of a material in order to calculate its k , which can potentially introduce errors into the overall measurement. It is important to note that in case of high temperature and high pressure experiments, the values of C_p usually cannot be measured directly and have to be extrapolated from low temperature data (Ross et al., 1984).

Measurement of thermal transport properties of materials in a DAC

Currently, there is a renewed interest in the development of techniques for measurement of thermal conductivity (k) under very high pressure and high temperatures.

Several non-contact techniques have been attempted in the past several years with the help of recent developments in laser-heated DAC technology (Hofmeister, 2007; Beck et al., 2007; Goncharov et al. 2009; Konopkova, Lazor, Goncharov, & Struzhkin, 2011). The motivation for using a laser-heated DAC for the measurements of k at high pressures and high temperatures is obvious since this is the only technique which allows one to experimentally subject any material to stable high temperatures and high pressures; and at the same time provides an optical window for the measurement of the high-temperature properties of that material.

Types of techniques that have been used to obtain values of k in a laser-heated DAC differ on whether a steady-state laser or pulsed laser heating was used during the experiment. A thermo-reflectance technique, a variant of the non-contact time transient techniques, has recently been used by Beck & Goncharov to measure thermal diffusivity (D) of several geo-materials at very high pressures and temperatures in a DAC (Beck et al., 2007; Goncharov et al. 2009). As of today, there is still debate on the validity of measurements obtained by this technique at high temperatures due to the very small time scales involved in the measurement and difficulties in constraining the amount of radiative heat flow associated with transparent materials (Hofmeister, 2009; Beck et al., 2009). So far, this technique can only be applied to optically transparent non-metals.

Several attempts have been made to use a steady-state laser-heated DAC for measuring k in materials at high temperatures and high pressures (Panero & Jeanloz, 2001; Kavner & Nugent, 2008). Very recently, a technique based on steady state heating laser-heated DAC was used by Konopkova et al. (2011) to constrain values of k for pure iron at high pressure or up to 70 GPa and high temperature and extrapolate values of k of

iron to earth core conditions. There are several benefits and difficulties of using steady-state heating techniques for measurement of k . Steady state heating techniques can potentially provide better accuracy of measurement of k because values of C_p and ρ do not play a role in the steady state heat conduction equation and therefore no assumptions are required about variations of these properties at high pressures and high temperatures. However, compared to transient heating techniques, steady-state heating techniques are much more sensitive to exact boundary conditions (i.e. laser power, external temperatures) and sample geometry. Therefore, they require very careful sample preparation, loading, and accurate measurements of temperatures.

In later sections, I describe ways to overcome the uncertainties in boundary conditions associated with the measurement of k at high temperatures and high pressures in a steady-state laser-heated DAC. I show how to obtain information about the material's high-temperature thermal conductivity by measuring the surface temperature distribution in the area of the laser heated spot using a non-contact spectro-radiometric technique and analyzing the measurements using inverse heat transfer computations.

Heat flow in a laser heated diamond anvil cell

All methods for measuring k require some prior knowledge and prediction of heat flow within the given experimental setup. Most engineering problems require the knowledge of thermal conductivity in order to predict a temperature distribution in a given system using the heat transfer equations; and the case of obtaining an unknown value of thermal conductivity is just the inverse. A known temperature distribution is fitted to a theoretically calculated temperature distribution, thus allowing the value of thermal conductivity to be obtained.

However, before entering into inverse analysis, one must know how to solve a given heat transfer problem in the forward direction (i.e. calculate temperature distribution within the system given known physical parameters of materials and boundary conditions). Heat transfer problems with simple geometries have been solved analytically in a large number of cases (Carslaw and Jaeger, 1959); however, systems with complicated geometries and problems involving non-linear effects such as radiative heat transfer are usually treated numerically (Goldstein, 2003). Heat flow in a laser heated diamond anvil cell has been treated analytically by Panero & Jeanloz (2001a, 2001b) for the case of a transparent laser absorbing media without consideration of radiative heat transfer. Calculations by Panero & Jeanloz show the dependence of temperature distributions in a DAC on various parameters – such as, sample thickness and temperature dependence of thermal conductivity (Panero and Jeanloz, 2001a). In another report Panero & Jeanloz demonstrated that using their heat transfer model is consistent with a predicted $1/T$ behavior of thermal conductivity of perovskite at high temperatures at 45 GPa. Steady state heat transfer in a laser-heated DAC has also been studied using non-analytic approaches such as a finite-element simulation (Bodea and Jeanloz, 1989; Kiefer and Duffy, 2005); and time dependent heat transfer in a laser-heated DAC has been studied using the finite-difference method (Morishima et al., 1998).

In the present study, the laser-heated DAC has been modeled using the heat-transfer and structural analysis simulation software COMSOL (formerly FEMLAB) (Andersen et al., 2005). COMSOL software provides a visual computer aided design (CAD) type interface and allows drawing the system geometry and solving any set of

partial differential equations prescribed to the system using finite element method (FE) (Andersen et al., 2005).

Using COMSOL software it is possible to exactly model the geometry of the sample and all of the experimental conditions to which the sample is subjected such as the laser heat source, boundary conditions – conduction and radiation as well as the pressure exerted and heat conducted through diamonds. The COMSOL simulation program accepts functional expressions for thermal conductivity, emissivity of the material and the power of the irradiating laser as an input and calculates the temperature distribution in the laser-heated DAC.

A 3-D model of DAC diamonds, gasket, pressure medium and the sample can be drawn using COMSOL. After specifying the system geometry, COMSOL performs automatic FE triangle meshing (Figure 2.1a, Figure 2.3d), and accepts an input of domain properties and boundary conditions for each of the system's sub-domains and boundaries (e.g. Table 2.2).

Figure 2.2 shows a CAD cross-section representation of the axi-symmetric diamond press system – two opposing diamonds, a gasket, and insulation layers, which has been modeled in COMSOL.

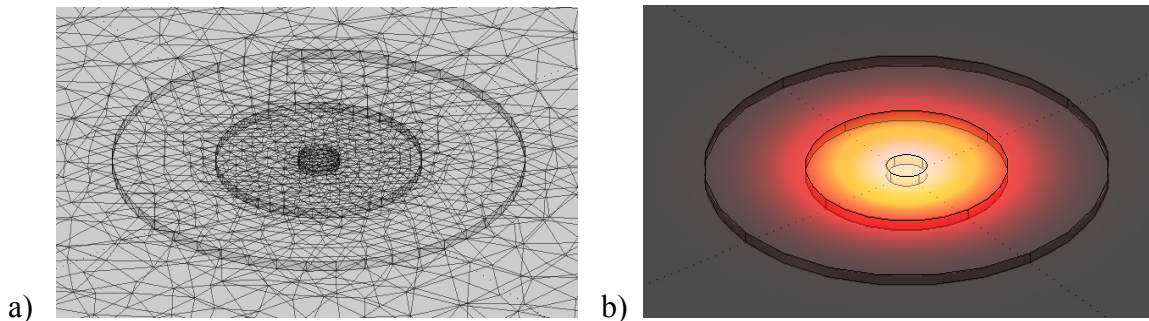


Figure 2.1. Finite-element calculation of temperature gradient of laser heated spot in 3-D.

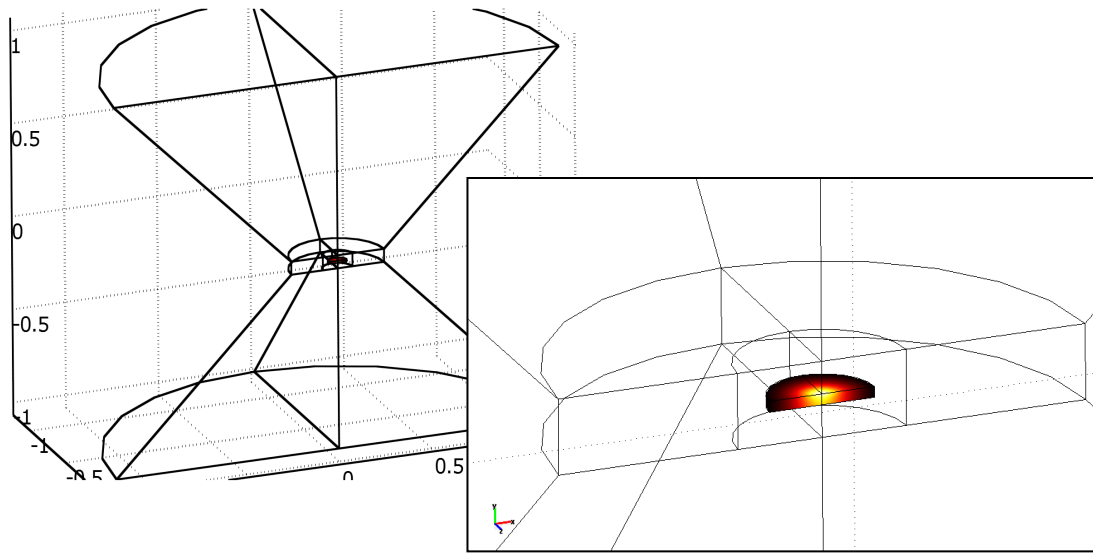
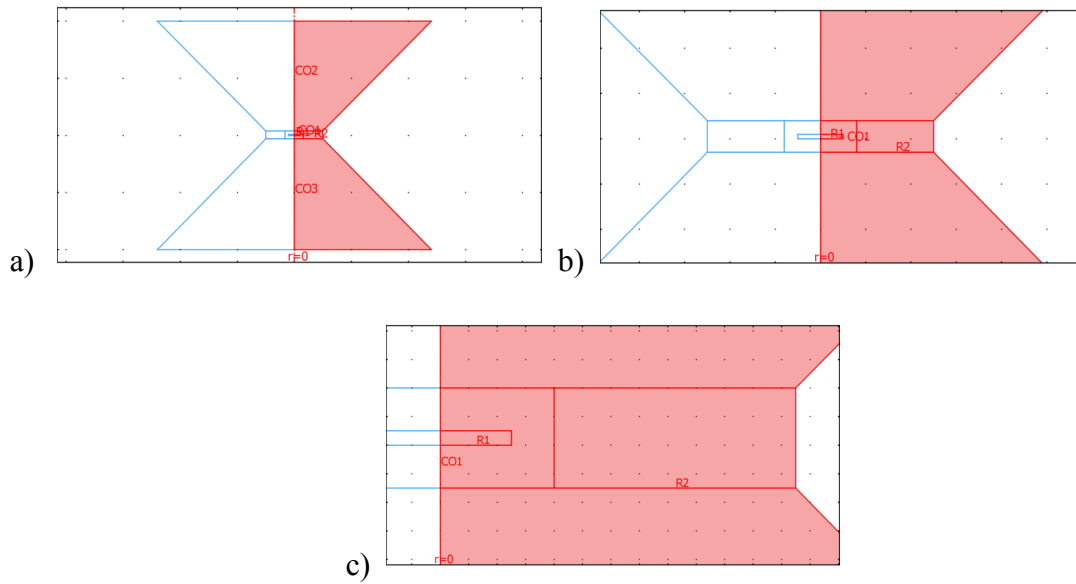


Figure 2.2. Modeling geometry for LH-DAC heat flow calculations. Diamond cell geometry is simulated in COMSOL. Employing the 2-D symmetry, the calculation speed can be increased by orders of magnitude.



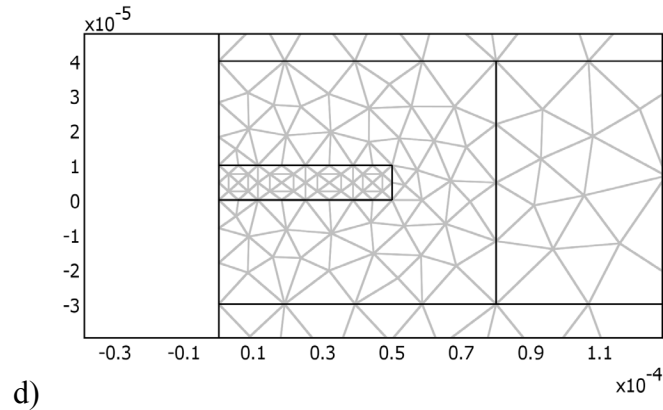


Figure 2.3. Modeling heat transport in LH-DAC in 2-D with axial symmetry. a, b, c) CAD drawn geometry of the DAC two opposing diamonds a gasket and insulation layers. Several levels of magnification are presented for clarity. d) Graphical representation of FE elements created using automatic meshing in COMSOL.

COMSOL Calculations

To reiterate what was mentioned in the previous section, the problem of obtaining thermal conductivity (k) is solved through an inverse heat flow calculation where some experimental observable is fitted to a theoretically calculated heat flow calculation. For systems with simple geometries an analytical expression can usually be derived which relates k [or thermal diffusivity (D)] to some experimental observable (e.g. temperature change over time, temperature gradients, etc.). Analytical expressions to relate k or D to experimental observables are considered too difficult to derive for systems with more complicated geometries (i.e. laser heated DAC with radiative heat flow calculations). Fortunately with currently available computing capacity of personal computers, expressions which relate k or D to experimentally measured data can be computed numerically. The standard heat flow differential equations are solved numerically (here using COMSOL) in iteration for many different values of the free variable (i.e. k , D , etc.) to calculate corresponding measurable temperature distributions. In the case of the laser

heated DAC, one is interested in calculating the variations in surface temperature distributions on the laser heated samples in a DAC depending on a multitude of variable thermal parameters (e.g. Table 2.2).

Heat flow equations are solved simultaneously at each point represented by vertices (nodes) of the triangles, Figure 2.3d. The areas immediately near the laser heated spot always have the largest temperature gradients; therefore, they require a higher density of nodes than other regions of the DAC. Use of adaptive density meshing of DAC geometry cuts down the calculation time by more than an order of magnitude. Calculations result in a temperature distribution calculated at each of the nodes in the mesh (see Figure 2.4 for typical COMSOL calculation output).

Equations involved in the finite element calculations and boundary conditions:

Table 2.1. Heat flow equations

1.	$\nabla \cdot (-k\nabla T) = Q$
2.	$T = T_0$
3.	$-\mathbf{n} \cdot (-k\nabla T) = 0$
4.	$-\mathbf{n}_u \cdot (-k_u \cdot \nabla T_u) - \mathbf{n}_d \cdot (-k_d \cdot \nabla T_d) = 0$
5.	$-\mathbf{n}_u \cdot (-k_u \cdot \nabla T_u) - \mathbf{n}_d \cdot (-k_d \cdot \nabla T_d) = q_0 + \varepsilon\sigma(T_{amb}^4 - T^4)$
6.	$q_0 = \frac{Q_{las}}{2\pi\sigma^2} \exp\left[-\frac{1}{2}\left(\frac{r}{\sigma}\right)^2\right]$
7.	$-\mathbf{n} \cdot (-k\nabla T) = h(T_{inf} - T)$

COMSOL obtains the temperature distribution by simultaneously solving the heat transfer partial differential equation at each of the nodes.

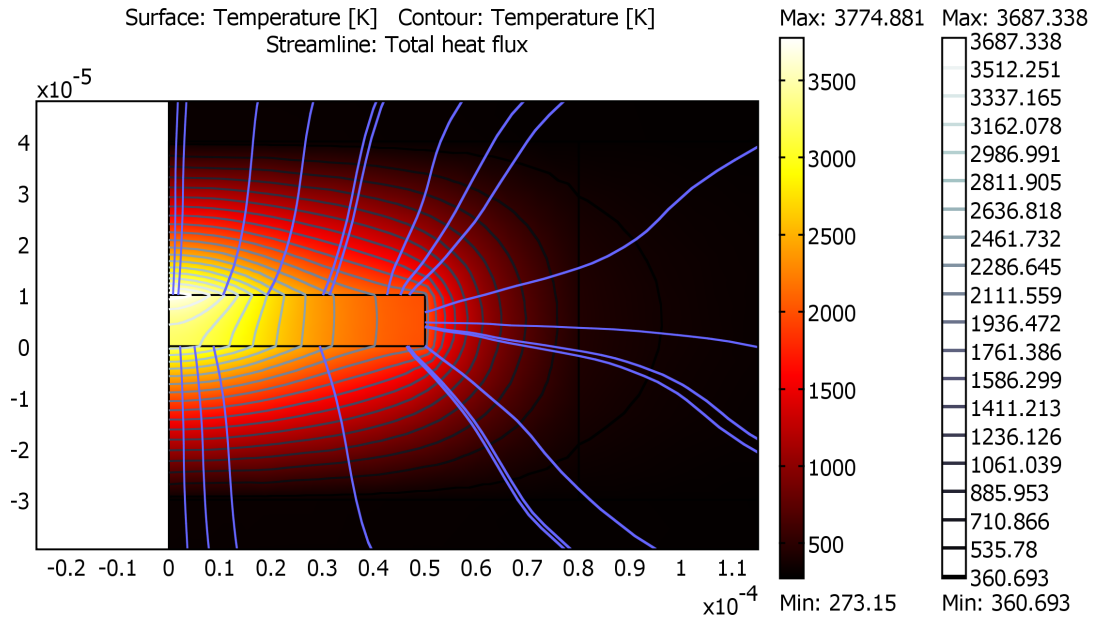


Figure 2.4. Typical calculated temperature distribution in a LH-DAC

The parameters which can be varied are: laser power, laser beam width, thermo-physical properties of sample, emissivity of sample, sample thickness (and overall geometry), dimensions of pressure chamber, thermo-physical properties of pressure medium, gasket, diamonds, surrounding temperature or boundary conditions (Table 2.2).

Table 2.2. Variable thermal transport variables

Region	Variable parameter	Value	Unit
Laser	Laser power	0.5	W
	Width of laser beam (Gaussian)	10	μm
Diamond	k of diamond	2200	W/(m K)
Insulation medium	k of insulation layer	10	W/(m K)
Gasket	k of gasket	20	W/(m K)
Sample	k of sample	76	W/(m K)
	sample surface emissivity	0.3	
	Ambient temperature	298.15	K
	Temperature of diamonds	298.15	K
	Convection coefficient of air	10	W/(m ² K)
	Laser coupling coefficient	1	

MATLAB – COMSOL connection

COMSOL can be controlled by external applications such as MATLAB (The MathWorks Inc., 2007), widely used software for mathematical programming. Controlling COMSOL using MATLAB enables creation of algorithms which enable automation of forward calculations. By numerically varying any of the heat flow parameters in the heat transfer system and running the forward calculation for each variation one can obtain a numerical function to understand how the parameter affects heat flow in a given system.

COMSOL creates a file which is essentially a MATLAB [* .m] file. In such a file there are various commands which are executed in a given sequence and various parameter values which are used in a simulation. Typically, the layout of the .m file is as follows: geometry data, meshing commands, settings for various materials properties and boundary conditions, instructions for solving of the problem, and type of expected output. COMSOL commands can then be encapsulated into custom MATLAB functions. MATLAB can use a ‘fem’ variable which is created by COMSOL and contains all of the

information about the model, all the necessary functions and variables. One can use encapsulated function calls to run many iterations of COMSOL calculations instead of manually running *script .m* files. This allows calculating a numerical functional dependence of any variables involved in the calculations, as well as using COMSOL calculation capability to run a least squares algorithms to fit experimentally observed data to any of the model parameters.

Functional description of heat flow system parameters' dependence on temperature, geometry or any other variable is defined as a polynomial on n-th degree.

FE heat flow calculations were used to obtain numerical relationships of the effect of sample thermal conductivity (k), thickness of the sample and thermal properties of insulations media on the full-width-half-max (FWHM) of the temperature distribution at the hot spot during laser heating. FWHM of the hot spot was found to be strongly correlated to k of the sample. Attention was also paid to comparing effects of different sample configurations (relative sample sizes and insulation media vs. sample thicknesses). Thermo-physical properties of all of the materials in the calculations were obtained either from literature or taken directly from COMSOL's extensive materials properties database. Our heat flow calculations performed with the aid of COMSOL agree well with previous FE calculations in a laser heated DAC (Bodea and Jeanloz, 1989; Kiefer and Duffy, 2005).

Both steady state and transient time calculations were performed in this study. As will be described in more detail in subsequent sections, the steady state computations were geared toward the problem of inverse calculations of thermal conductivities from measured temperature gradients in an approach similar to those described by Kavner et

al. (2008) and Konopkova et al. (2011). For example, temperature solutions were calculated for two different materials in a laser-heated DAC in identical loading conditions and differing only in their k . Figure 2.5 and Figure 2.6 show typical temperature solutions for a particular set of samples. Figure 2.5 shows two hypothetical temperature distributions for different materials with k differing by a factor of 2. The two materials were virtually heated to the same maximum temperature and it can be seen that the temperature gradients for the material with higher k is significantly more spatially spread out than for the material with lower k . Figure 2.6 shows a one-dimensional plot of calculated radial distribution of surface temperatures for two materials, Pt and Zr with nominal $k=76$ W/(m K) and 26 W/(m K) respectively, each of the materials heated to a series of increasing maximum temperatures by variation of the laser power. This result is well in accord with previous reports (Bodea and Jeanloz, 1989; Panero and Jeanloz, 2001a, 2001b; Kiefer and Duffy, 2005).

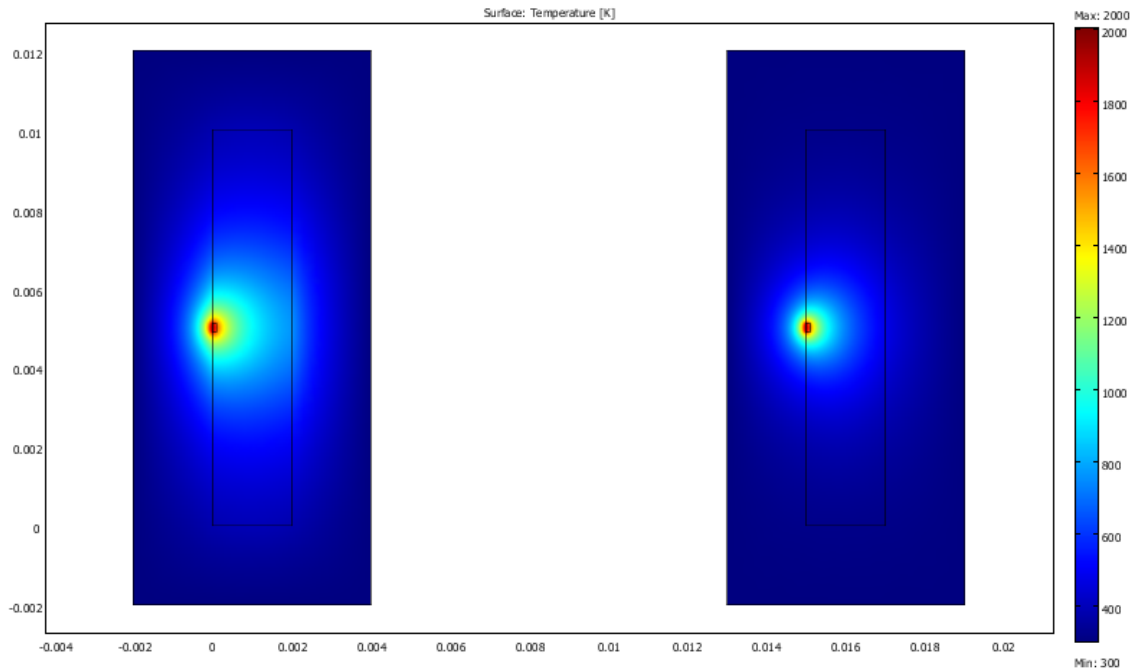


Figure 2.5. Effect of thermal conductivity on heat flow in LH-DAC: comparison of calculated temperature gradients for materials with different thermal conductivities in LH-DAC. Calculations are done using 2-D axially symmetric geometry. Laser shape was described using a Gaussian distribution function. The laser power in two cases was adjusted so that the maximum temperatures in both samples are equal.

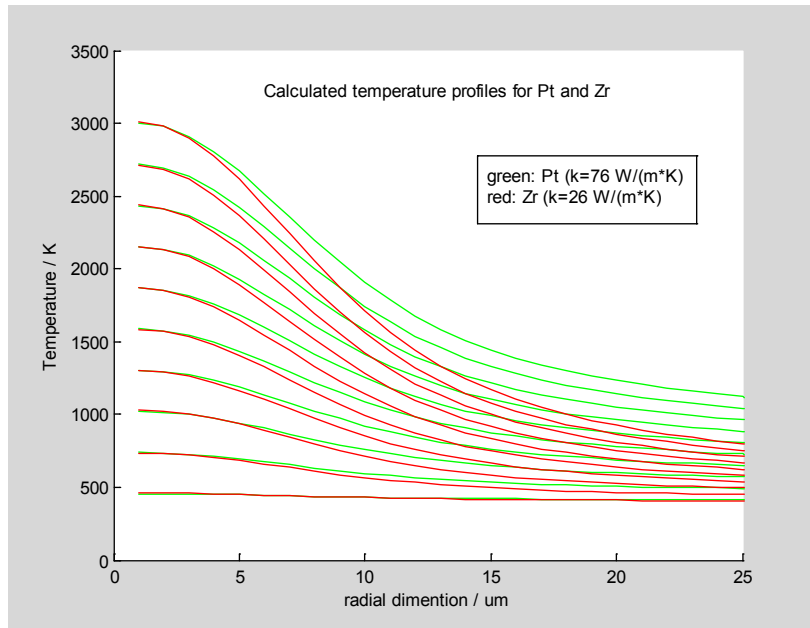


Figure 2.6. Comparison of calculated temperature gradients for Pt and Zr, materials with different nominal thermal conductivities heated to several different maximum temperatures. Laser shape was described using a Gaussian distribution function. The laser power in two cases was adjusted so that the maximum temperatures in both samples are equal.

It is generally known that different solid phases of the same material can have different values of thermal conductivity (k), which is generally correlated to the degree of crystal symmetry. Differences in thermal transport properties of different phases of a material can be used to map out phase transition boundaries at various P - T conditions.

Steady state and transient calculations were done to see whether differences in k in different phases of a solid can be used to map the phase transition boundaries at high pressures and high temperatures. In the event that different solid phases of a material have sufficiently different k , steady state calculations show that the laser power vs. temperature of laser heated material can be used to determine the exact temperature of the phase equilibrium. Figure 2.7 shows a typical calculation for a material with a discontinuity in the value k at given temperature corresponding to a solid-to-solid phase

transition. As was expected, FE calculations show that a discontinuity in k between two phases of a material results in changing of the slope of the laser power vs. maximum temperature of the sample. In case of the plot shown in Figure 2.7, the difference in k between the two phases is a factor of 2.

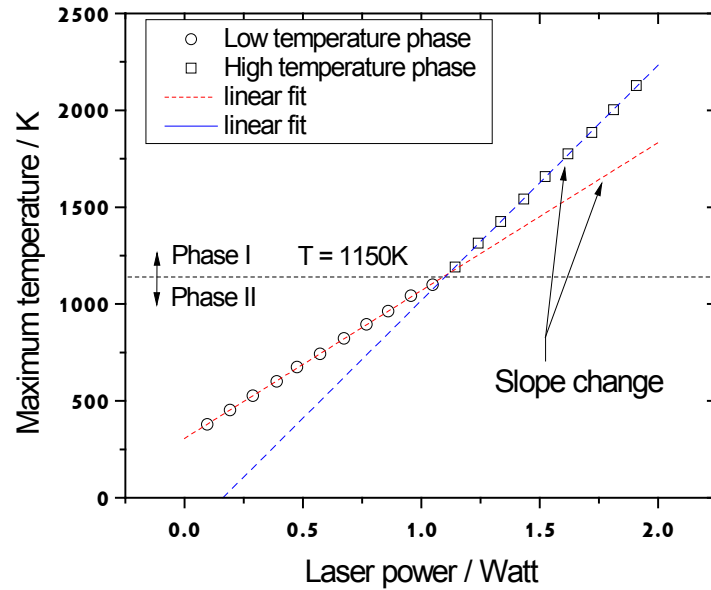


Figure 2.7. Calculated power vs. temperature plot for a hypothetical material with $k=26$ W/(m K) for $T < 1150$ K and $k=15$ W/(m K) for $T \geq 1150$ K, laser-heated in a DAC. A change of slope is apparent at 1150K, the phase transition temperature. When a material has a discontinuous thermal conductivity the power vs. temperature profile shows a discrete change in slope.

Steady state calculations neglect any effects of latent heat and/or emissivity changes associated with phase transitions and therefore do not accurately describe the actual experiment. Therefore, transient time calculations were done to accurately model the laser heating induced phase transition experimental conditions with accurate considerations of latent heat and emissivity. Latent heat of a phase transition has been modeled using the method described by Groulx et al. (Groulx and Ogoh, 2009). The

transient analysis predicts a plateau-fluctuation of temperature around the phase transition temperature; which has indeed been observed in our experiments.

Finally, as required for a systematic error analysis, FE calculations were used to compute the sensitivity of temperature calculations to many different variable parameters and boundary conditions involved in heat flow in a laser-heated DAC.

FE parameter sensitivity calculations have shown that, in fact, the material physical properties have large enough correlation with the observed temperature distribution and would not be overshadowed by contributions from errors in system geometry. This is very important because system geometry can seldom be reproduced from one experiment to another even in the current state of the art of the DAC sample loading techniques.

The main experimental difficulty which still stands in the way to accurate measurements of k in a steady-state laser-heated DAC is the inability to accurately constrain the laser power absorbed by the material (Konopkova et al., 2011). The technique described in the subsequent sections avoids the uncertainty in the laser power absorption of the sample by utilizing a calibration technique that uses a standard material with a known k . Pure platinum is commonly used as a k standard in industrial thermal properties measurements. Spectral emissivity (ϵ) of platinum has been measured in previous studies (Dubrovinsky & Saxena, 1999a; Deemyad & Silvera, 2008). Therefore, the difficulty in constraining the values of absorbed laser power in laser-heating experiments involving platinum is not as severe. Determining k of platinum or another standard material at high-temperatures and high pressures can be done using the method

described by Konopkova et al. (2011). Measurement of k of other materials at high-temperature and high-pressures is described in a later section.

2.02 Experimental methods and system design

Laser heating the DAC

In designing the experiments I kept the following goals in mind 1) to be able to compress our samples to very high pressures while simultaneously heating portions of the samples to very high temperatures in a controlled fashion; 2) to prepare and load the samples in repeatable geometries with known boundary conditions; and 3) to be able to measure temperature distributions in the heated samples.

Typical laser-heating systems for the DAC are capable of heating a small portion of the sample in a DAC to thousands of Kelvin (K) and simultaneously measure temperatures at the hottest point using a non-contact spectral-radiometric technique (Shen et al., 2001; Meng et al., 2006b) Several laser-heating installations have been described in the literature that are capable of measuring not only the temperature of the hottest point but also the profile of the temperature distributions across the sample, either in a one-line scan or a full 2-dimensional map (Shen et al., 2001; Campbell, 2008; Kavner and Nugent, 2008).

The samples are loaded in a DAC (see Figure 1.3, Figure 1.4) and are heated on one side using a focused beam from a Nd:YLF laser (1053nm, CW, maximum power: 50W, TEM₀₀, focused using 20x Apo-chromat focusing objective, Mitutoyo) (see Figure 2.8). The power of the laser is controlled by attenuation using a $\frac{1}{2} \lambda$ wave-plate and a polarizing prism. Temperature of the heated surface is measured using the non-contact spectral-radiometric technique which is used in many other laser heating systems (Shen et

al., 2001; Boehler et al., 2009) The thermal radiation from the surface of the specimen is measured and fitted to the Plank's equation which relates the intensity of light (I) radiated from a material at temperature (T) as a function of wavelength (λ):

$$I(\lambda, T) = \frac{2\pi hc^2 \varepsilon}{\lambda^5 [e^{(hc/k)\lambda T} - 1]} \quad \text{EQ. 2-4}$$

where ε is the emissivity, h is the Plank's constant, c is the velocity of light.

Temperature distribution across the surface of the specimen can be obtained by fitting the above mentioned parameters to grey-body radiation collected from several points across the sample. Wavelength and temperature dependences of emissivity play a role in the fitting of the Plank's equation ($I(\lambda, T) = \frac{2\pi hc^2 \varepsilon}{\lambda^5 [e^{(hc/k)\lambda T} - 1]}$ EQ. 2-4), but usually a simple linear dependence is assumed (Dubrovinsky and Saxena, 1999a). Similar to a method described by Jeanloz et al. (1996), a thin slit in front of the spectrometer coupled with a 2-dimensional (2-D) CCD detector is used to measure an entire line scan of a temperature gradient on the sample's surface in a single exposure. The thermal radiation from the specimen's surface is collected by the focusing objective (the same objective which is used for focusing the laser) and directed to a spectrometer. An achromatic lens is placed in front of the spectrometer to focus the image of the sample's surface on the spectrometer's entrance slit. The entrance of the spectrometer is a $\sim 30\mu\text{m}$ vertically oriented narrow mirror slit which enables only a single line thermal radiation from the sample to enter the spectrometer. The light which does not go through the slit is reflected and directed via a beam-splitter to a video camera monitor (Figure 1.5 a-b). Using a mirror slit allows constant monitoring of sample alignment. The diffraction grating in the spectrometer decomposes each point on the line of light that enters the

spectrometer into its corresponding wavelength spectrum, thus creating a 2 dimensional image which is collected on a 2-D charge-coupled device (CCD) detector. Each horizontal line on the CCD contains spectrum of one point from the vertical line of thermal radiation from the sample's heated surface. Thermal radiation spectrum obtained on each horizontal line of the CCD is intensity-corrected and fitted to a Plank's spectral radiation equation ($I(\lambda, T) = \frac{2\pi hc^2 \epsilon}{\lambda^5 [e^{(hc/k)\lambda T} - 1]}$ EQ. 2-4) to obtain the temperature of the corresponding point on the vertical line selected by the narrow slit.

An alternative approach to calculate the temperature gradients is to use a method similar to the one described by Kavner et al. (2008). Plank's equation fitting is done only for the point with the highest intensity (highest temperature), and the Stefan-Boltzmann law is used to calculate the temperatures of adjacent points. The Stefan-Boltzmann law for the total flux (j) at a given temperature (T) is:

$$j = \sigma T^4 \quad \text{EQ. 2-5}$$

where the σ is the Stefan-Boltzmann constant. The total integrated intensity from several CCD rows adjacent to the row corresponding to the highest temperature point is used to determine the one dimensional scan temperature distribution across the hot spot.

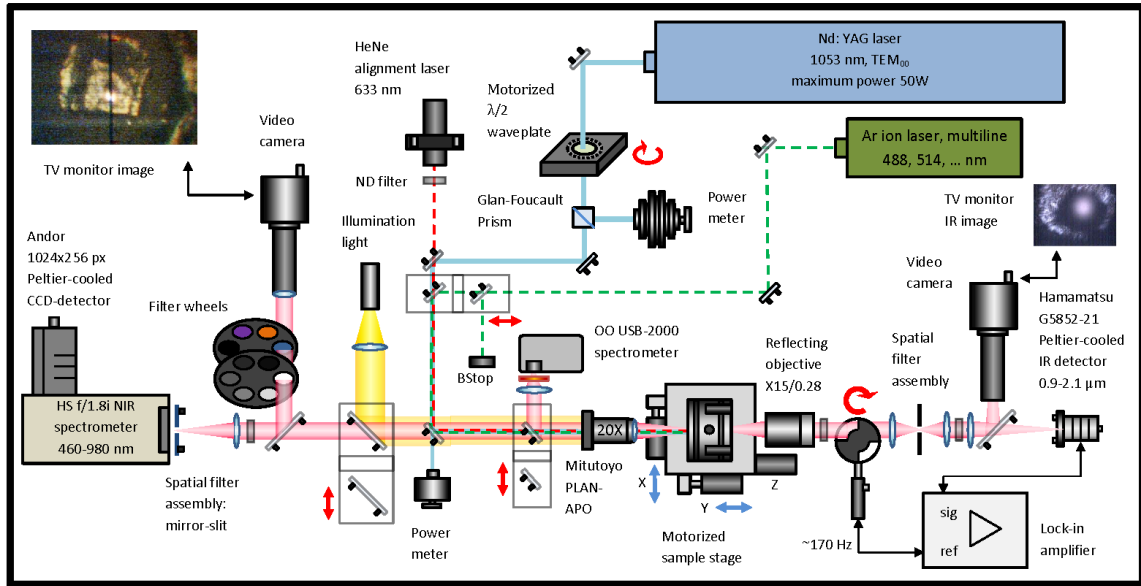


Figure 2.8. Laser heating system in CeSMEC, (schematic)

Experiment control and data collection methods

Custom software was designed for the laser heating and temperature measurement system. The software, written in LabVIEW programming language, integrates the control of individual laser heating system components and enables complete automation of the experiment through a graphical user interface (UI) (Figure 2.9). Some of the key hardware components of the system, which are controlled by the LH-DAC software suite, are the half-wave plate actuator for laser power control (Newport), laser power meter (Melles-Griot), actuator for image scanning (Newport), and a CCD detector for blackbody radiation measurements (Andor). In-line ruby fluorescence measurement setup has been installed on the laser heating system using a separate Ocean Optics spectrometer. This system allows for an *in-situ* determination of pressure in the DAC.

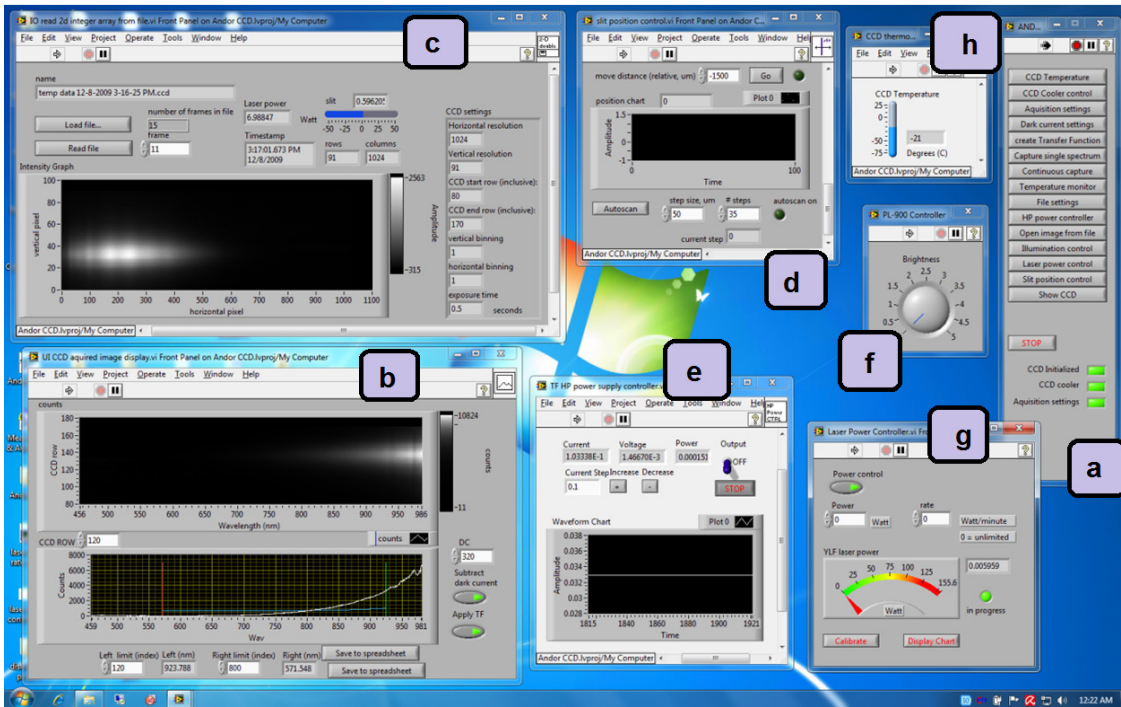


Figure 2.9. Laser-heating system UI: Several modules which are a part of the LH-DAC software suite. a) main control menu, module launcher; b) acquired CCD data display; c) saved data file reader; d) spectrometer thin slit actuator; e) resistive heating power control; f) illumination control; g) laser power control. Not shown: optical transfer function measurement calculation; grey-body temperature fitting; multi-frame data file thermal gradients analysis; database UI for experiment record retrieval and management.

The file manipulation and data analysis part of the software suite can be used together or separately from experimental data acquisition part. I wrote a standalone software suite which can be used for reading the recorded files and analyzing the temperature histories and thermal gradients. This way the experimental data are portable and not tied to the Laser-heating PC, which requires various drivers to be installed in order for the CCD software suite to run. Recorded files can be opened and analyzed on any computer with any operating system.

The CCD data acquisition can run in a loop, enabling continuous temperature measurement and recording. Prolonged experiments such as measuring melting

temperatures in the laser-heated DAC creates a large amount of raw data, therefore the recorded file storage has been consolidated into a database system which organizes the large amount of recorded data into separate projects experiments. Each data file consists of a series of frames and each frame contains the raw CCD signal, CCD settings and laser power and other variable experimental parameters.

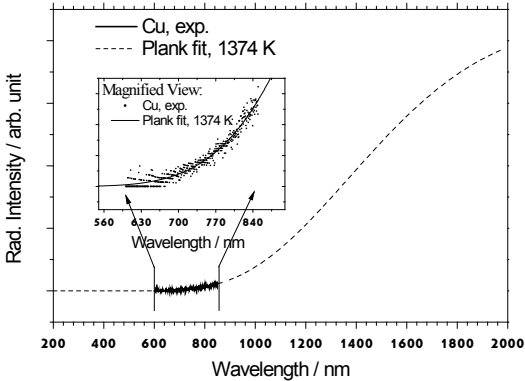
Temperature measurement system accuracy and calibration

It is well known that there are many potential causes of temperature measurement errors associated with using the type of spectro-radiometric technique that has been described in the previous section. Therefore, it is absolutely necessary to carefully calibrate the system using available optical radiation standards, i.e. determine the optical transfer function of the system, to be able to properly correct the raw thermal radiation spectra measured during an actual experiment. Optical transfer function of the system was determined using thermal radiation from a resistively heated platinum wire at its melting point (temperature of 2041 K) at ambient pressure as a spectral intensity radiation standard. The optical transfer function was subsequently checked by measuring spectra of several metals at pressure of 1 bar at their known melting temperatures (e.g. Cu, Fe, Hf, W) (Table 2.3). The plots in Figure 2.10 show typical quality of fitting of collected blackbody radiation from several samples at their melting point temperatures. Metal wires made from these respective metals were resistively heated in a specially made heater assembly by applying voltage to endpoints of the wires. The heating was done in ultra-high purity UHP argon flow. The thermal radiation was collected from the wires' surface at the hottest point until their melting temperatures (i.e. until the wire melts and stops conducting current). The melting temperatures measured for these metals using

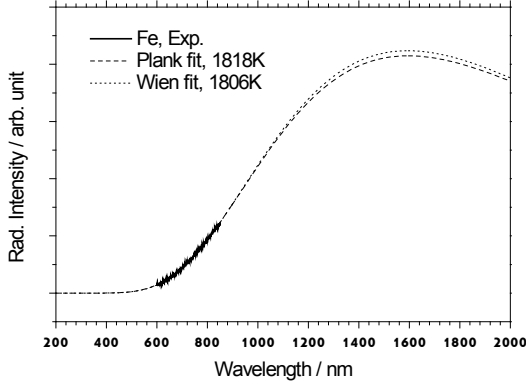
the temperature measurement system in CeSMEC agree well with melting data from the published literature (see Table 2.3 and Figure 2.11).

The optical transfer function obtained from the melting point of platinum was used here as a point of calibration for a custom constructed tungsten lamp setup. The assembly of the tungsten lamp setup is a tungsten filament lamp is positioned behind a small pinhole in a mechanically stable configuration. This allows the same light to be imaged by the spectrometer every time. The spectrum of the calibration lamp is measured at a chosen current of 6.000 amperes, which provides suitable spectral coverage in the range of wavelength of interest. Using the tungsten lamp has two advantages – 1) it is experimentally simpler than having to melt platinum each time to re-measure the transfer function, and 2) it yields acceptable accuracy of calibration.

a)



b)



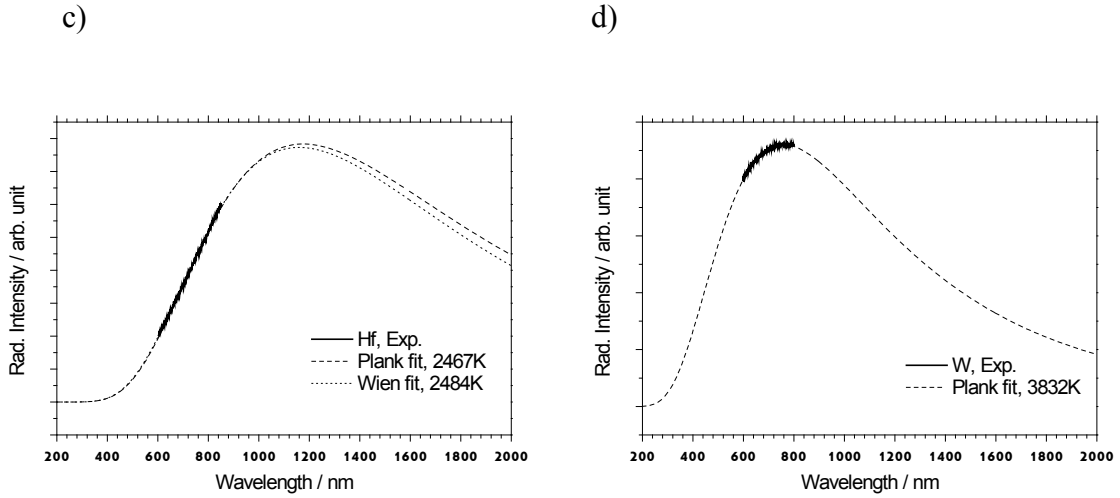


Figure 2.10. Plank's equation ($I(\lambda, T) = \frac{2\pi hc^2 \epsilon}{\lambda^5 [e^{(hc/k) \lambda T} - 1]}$ EQ. 2-4) fitting to spectra obtained from several resistively heated metals at their melting temperatures. (Pressure = 1 bar)
 a) Cu, b) Fe, c) Hf, d) W

Table 2.3. Temperature measurement calibration. The temperature measurement system reproduces the melting temperature data for many common metals.

Metal	Literature reported T_{melting} (K)	Radiometrically measured T_{melting}	
		Plank's equation least squares fit T_{melting} (K)	Difference from literature value
Cu	1357	1389	2.36 %
Fe	1811	1800	-0.60 %
Pt	2041	(used for calibration)	
Hf	2506	2576	2.79 %
Mo	2896	2563	-11.50 % large error
Re	3459	3425	-0.98 %
W	3695	3795	2.70 %

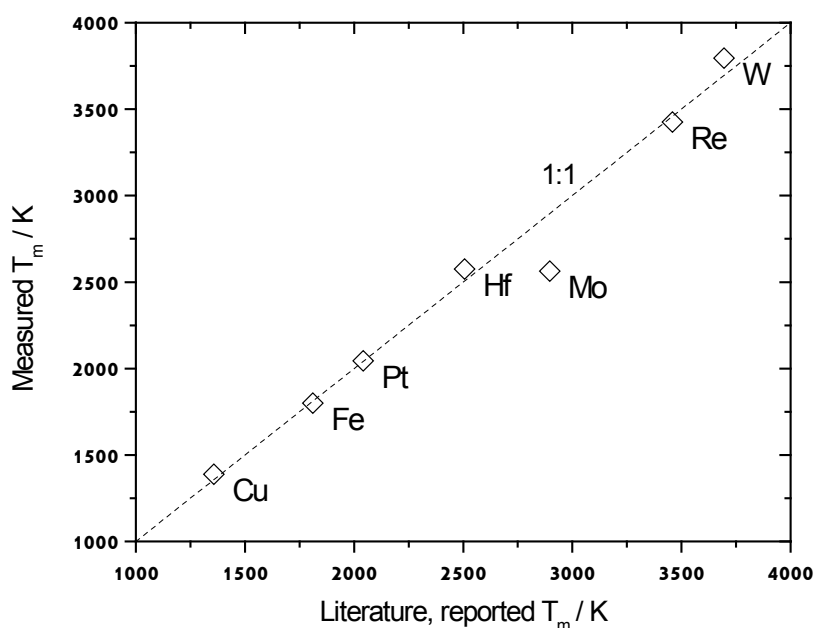


Figure 2.11. Accuracy of temperature measurement. The temperature measurement system reproduces the melting temperature data for many common metals (with exception of Mo, probably due to oxidation. Oxide of Mo has a lower melting temperature than the pure metal). Note: Melting of hafnium in UHP argon flow was problematic due to rapid oxidation. Hafnium and tungsten wires were resistively heated to melting temperatures in argon + hydrogen gas mixture flow. (200 vol. argon to 5 vol. hydrogen mix). This leads to correct measurement of melting temperature of hafnium. Line labeled 1:1 is shown simply as a visual aid, it does not represent a least squares fit.

Finally, based on published methods and the techniques developed in this study, I offer the following recommendations:

- A new optical transfer function must be measured before running each new series of experiments. This is because even a several-micrometer movement of the spectrometer entrance slit changes the transfer function of the system very drastically.
- It is critical that the aperture in front of the focusing objective (if one is used) must be placed precisely at the center of the optical axis, otherwise very large optical (chromatical) aberrations, which lead to temperature measurement errors, will occur.

Reliability of temperature measurement at high pressures

Melting temperatures of iron were measured at pressures up to 50 GPa in order that our temperature measurement system can provide accurate temperature measurement for materials under high pressures in a DAC. In this case, the pressure was determined in cold samples using ruby fluorescence. In this experiment, the errors associated with effects of thermal pressure are considered to be much smaller than the accuracy of the measurement of the temperature of melting (within the experimental error); and therefore the measurement of pressures at higher temperatures are not corrected for the effects of thermal pressure.

Different criteria are commonly used by others to determine the onset of melting in laser heated diamond anvil cell experiments. In our laboratory experiments I used an all-optical technique described by others (Boehler, 1993; Saxena et al., 1994; Dubrovinsky and Saxena, 1999b). This technique relies on plotting laser power against temperature and observing a plateau in the temperature profile at some high temperature.

The plateauing and fluctuation of the temperature of a laser heated spot around a certain temperature occurs because of a rapid melting and freezing of the solid and is commonly referred to as the ‘yo-yo’ effect. A theoretical analysis of the temperature oscillations with increasing of the laser power was presented by Dubrovinsky and Saxena (1999b) and confirmed in this study using FE COMSOL calculations.

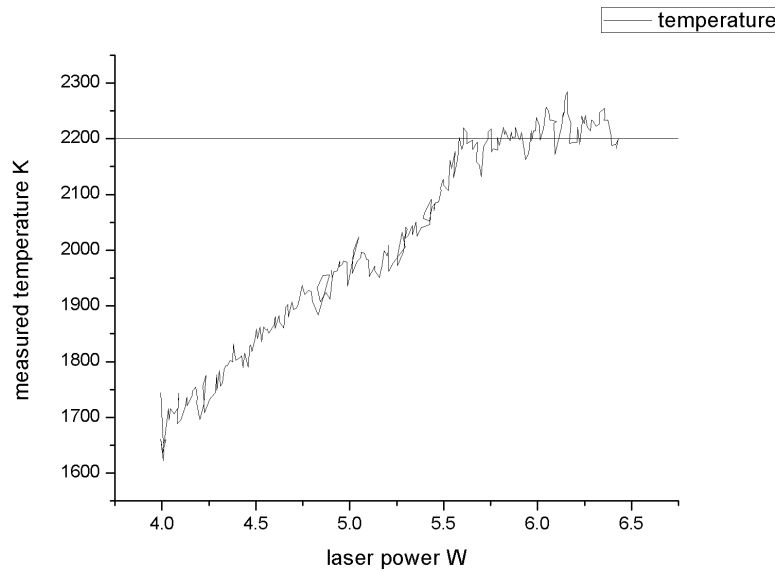


Figure 2.12. Temperature vs. laser power plateau. The melting point of Fe is measured by looking for a plateau in the temperature during the increasing of the laser power. As seen in this figure, during the increase of the laser power the temperature of the sample plateaus and fluctuates around 2200K, this is taken as the melting point of the solid. Pressure \approx 18 GPa

Spectral thermal emissivity (ϵ) of many materials is often unknown, which creates significant errors in temperature measurement using the Plank’s equation ($I(\lambda, T) =$

$$\frac{2\pi hc^2 \epsilon}{\lambda^5 [e^{(hc/k)\lambda T} - 1]} \quad \text{EQ. 2-4). Other errors arise from detector misalignment and}$$

incorrect optical transfer function measurements. One way to check the optical alignment of the system is that if alignment is correct then the wavelength range chosen fitting of

the plank equation should not affect the resulting temperature. If different values of temperatures are obtained by fitting different ranges of wavelengths, then likely the optical alignment is wrong. Around 2000K, typical combination of errors usually amounts to about 150K absolute temperature uncertainty. However, relative temperature uncertainties (difference in temperature of one experimental point to the next) can usually be as low as 15K.

Hotspot temperature history [increasing laser power]

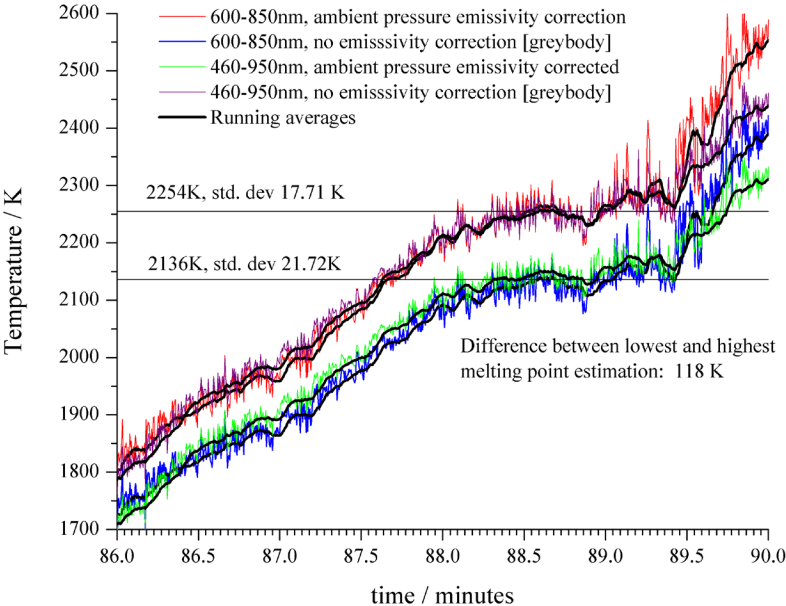


Figure 2.13. Uncertainties in radiometric temperature measurement. Pressure = 18 GPa.

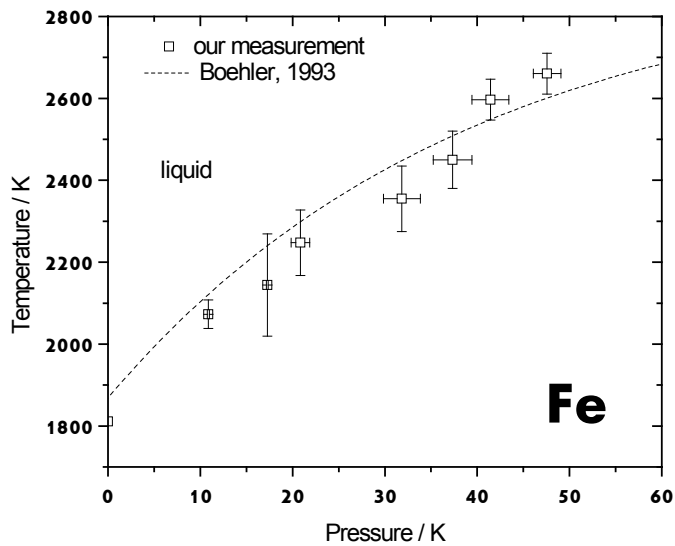


Figure 2.14. High pressure melting curve of Fe

Measured melting points of Iron to pressures of up to 50 GPa. (Sample: Iron, 70 micrometer square foil, 20 micrometer thickness; Pressure medium MgO, dried 1000C; Pressure determination: ruby fluorescence scale)

Using reverse side temperature measurement as melting determination criteria in a laser heated DAC

Here I describe a new method which can potentially provide additional ways of melting of ways to determine melting of optically opaque materials during laser heating. Relying on the ‘yo-yo’ effect alone can sometimes lead to an incorrect assumption of melting. The ‘yo-yo’ effect can sometimes be seen at temperatures which are clearly not representative of the melting temperatures. A chemical reaction of the sample with the insulation media can manifest itself as a fluctuation of temperatures that is indistinguishable from the typical ‘yo-yo’ effect associated with melting. It is very difficult to distinguish between the ‘yo-yo’ effect arising from a reaction from a similar effect arising from a phase change in a material because in both cases they are caused by

a change in heat flow parameters in the laser heated sample and/or its immediate environment (i.e. insulation medium). In either of these cases, the temperature on the laser heated side of the sample undergoes some degree of fluctuation near a given temperature. However, the overall heat flow picture in a laser-heated DAC when a sample undergoes a reaction with the insulation medium is somewhat different from the case when a sample melts or undergoes a phase change. This led to a realization that the two cases (i.e. reaction vs. phase change in the sample) should be experimentally distinguishable utilizing continuous temperature measurements of both sides of the sample – the laser heated side and the reverse side (i.e. non-laser heated side), in contrast to relying on temperature measurements only on the laser-heated side. To confirm this hypothesis, I compared results of laser heating experiments involving two differently loaded samples. In one case a metal sample was loaded into a DAC in argon atmosphere with MgO dried at 1000 °C. Another sample was prepared in controlled ‘dirty’ conditions, i.e. the sample was loaded in air and the pressure medium was not previously dried. From previous experiments it was known that samples loaded in an inert atmosphere environment and with properly dried insulation medium are generally safe from reactions at pressure and at temperature ranges of interest up to their melting temperatures. On the other hand, the samples loaded with ‘dirty’ insulation medium have been previously known to react with the insulation medium and show a ‘yo-yo’ effect at temperatures lower than their melting temperature. I laser heated the respective samples to about 1800K, below onset of the ‘yo-yo’ effect. I measured the temperatures of the sample and monitored the infrared glow on the laser heated side and on their reverse (non-heated) side (Figure 2.15). Subsequently, I increased the laser power sufficiently to

observe the ‘yo-yo’ effect. In case of the ‘dirty’ sample, during the onset of the ‘yo-yo’ effect, the thermal glow on the reverse side disappeared and temperature dropped below the measurable range. In case of the ‘clean’ sample the onset of the ‘yo-yo’ effect on the laser heated side did not extinguish the thermal glow on the reverse side and the temperature on the reverse side did not drop below the measurable range. Potentially, it may be possible to use the reverse side temperature measurements in order to systematically determine the validity using the ‘yo-yo’ effect for melting determination in a variety of materials.

Measuring the temperatures on the reverse side

The DAC laser heating system in CeSMEC has been modified to include a capability to measure temperature of the sample during heating from both sides. Due to the fact that the heating is only from one single side, the temperatures on the side of the sample which is not being heated are lower than on the laser heated side. During normal laser heating experiments, the temperatures on the non-heated side are usually below 1500K and are too low to be measured using the same radiometric technique as is used for the laser heated side. However, there is enough infrared radiation from the sample even at low temperatures to be able to monitor and measure temperatures in the DAC as low as 300 °C (Shuker et al., 2008). Figure 2.15 shows an infrared video camera image (false color) of thermal radiation from a sample which was laser heated from the opposite side. As shown in a schematic in Figure 2.8, in order to be able to accurately measure the temperatures on the reverse side I use the photodiode (Hamamatsu G5288-21) detector, which is sensitive down to about 200 °C. Voltage created by the photodiode is amplified using a lock-in amplifier, based on design by Shuker et al. (Shuker et al., 2008). Using a

lock-in amplifier allows extremely noise resistant measurements and a very high dynamic range. I wrote a custom auto-leveling software algorithm which automatically adjusts the sensitivity range of the lock-in amplifier which allows me to measure voltages from the photodetector over at least 4 orders of magnitude with extremely fine resolution in each range.

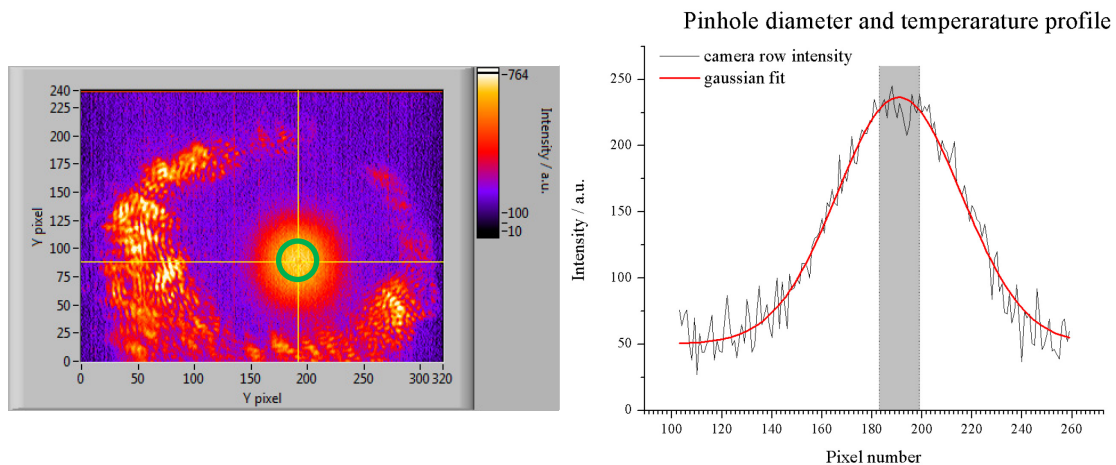


Figure 2.15. Reverse side temperature measurement

Left - an example of the glow from the sample on the reverse side (image taken with a Logitech webcam). A region of interest (green circle) is selected out using a spatial filter (pinhole) before entering the photodiode detector. To minimize the temperature reading error, the area must be as small as possible and contain no large temperature gradients. Right - radiative intensity from one row on the image on the left, comparison between hotspot width and pinhole diameter (grey region represents light collected by the photodiode).

Calibration of the G5852-21/SR-510 pyrometer system

Resistively heated Poco graphite and a tungsten wire were separately used radiation intensity standards to calibrate the signal from the infrared detector versus sample temperature. The detector was calibrated using a Poco graphite strip heater assembly which included a thermocouple embedded into the graphite strip.

There is overlap between temperature ranges that are measurable with the ‘front’ and ‘reverse’ side setups. The temperature measurements made by the previously calibrated ‘front’ side can be used to calibrate the ‘reverse’ side infrared detector. Therefore, in case of resistively heated tungsten, the visible light spectro-radiometric measurement setup on the ‘front’ side of the system and the infrared detector were focused onto the same point on the resistively heated wire.

2.03 Measuring heat flow and mapping phase transitions in Hf at high P-T

An experimental study to determine phase transition temperatures in hafnium was carried out using an all-optical approach under high pressure of up to 50 GPa. These experiments revealed unexpected features in the high pressure/temperature phase diagram of hafnium, contrary to studies on hafnium using combined laser heating and synchrotron radiation (described in Part 1 of this dissertation).

Introduction

Hafnium has a hexagonal-close packed (α -phase) structure typical of group IV transition metals (Ti, Zr). At ambient pressure (P), hafnium transforms from a room-temperature α to a body-centered cubic (β -phase) structure at temperatures (T) above 2030 K. Upon increasing the pressure at room-temperature, hafnium is reported to undergo a sequence of $\alpha \rightarrow \omega$ (simple hexagonal) $\rightarrow \beta$ phase transitions, which is also typical of other group IV metals (Xia, Parthasarathy, et al., 1990). Although it is generally considered that hafnium would follow the general α - ω - β high P - T phase diagram consistent with many other metals with *hcp* structure at ambient P - T conditions (Xia, Parthasarathy, et al., 1990; Joshi et al., 2002) the phase transitions for Hf have never been experimentally studied at simultaneous high pressure and high temperature conditions.

Several approaches can be used to determine P - T of phase transitions in materials in a laser heated diamond anvil cell. Melting in a diamond anvil cell is usually determined using either all-optical techniques or using x-ray diffraction. An optical technique usually entails relying on optical observations of the laser heated sample to determine the onset of melting or of a solid-solid phase transition. The optical

observation can mean either visual observation of convective motion in the vicinity of the heated spot or measurement and analysis of the relationship between laser power and temperature of the sample. In the latter technique, the onset of melting or a solid-solid phase transition usually manifests itself as either a plateau, change of slope or a discontinuity in the temperature vs. laser power relationship, depending on heat transport and surface emissivity properties of corresponding phases. Combining an optical approach with x-ray diffraction is usually used to check the reliability of each of the individual techniques. In fact combinations of optical and x-ray diffraction based techniques are nowadays commonly used to study melting of materials at very high pressures and high temperatures in synchrotron laboratories (Jeanloz et al., 1996; Errandonea et al., 2000; Errandonea, Boehler, et al., 2001; Errandonea, Schwager, et al., 2001a; Errandonea, 2004b). Errandonea (2006) gives a good review of the current technical advances in using an optical and x-ray diffraction experimental setup for determining high pressure melting behavior of transition metals.

Experiment

The sample, a commercially obtained Hf metal foil of 99.97% purity with nominal 3% Zr was loaded into a DAC of symmetrical type with diamonds 400 μ m diameter culet. The gasket used in the DAC was made out of 302-type stainless steel and indented to thickness of \sim 40 μ m and a hole for the sample was drilled with a diameter of 100 μ m. Ruby fluorescence scale was used as an internal pressure standard at room temperature (Mao et al., 1978). For sample loading schematic refer to Figure 1.4a. MgO powder, dried at 1000 $^{\circ}$ C, was used as the pressure transmitting and insulation medium. In several experiments, CsCl was used instead of MgO as an insulation medium. Due to the

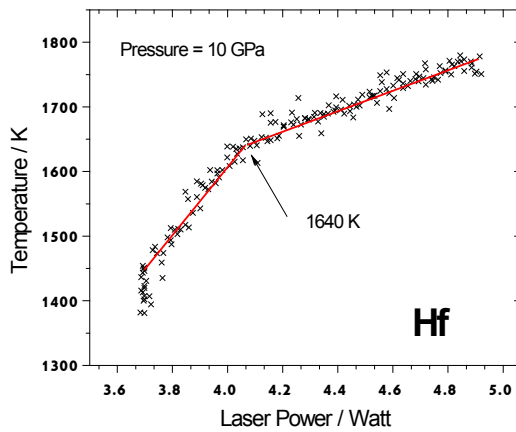
lower thermal conductivity of CsCl, only about 60% of the laser power was to reach same maximum temperatures by using CsCl instead of MgO. Loading of the sample was done in a glove box with ultra-high-purity (UHP) argon flow atmosphere. Loading Hf in MgO with argon was found to be a necessary step to prevent unwanted oxidation of the sample during laser-heating.

The heating was done using the single sided laser heating system in CeSMEC and the temperature was measured using a non-contact radiometric technique described in previous sections. Grey-body emissivity of the sample was assumed. Transfer function of the optical system was calibrated by an average of two blackbody standards: platinum at 2041K and tungsten at 3695K. Several points on the sample were laser-heated, in each case by gradually increasing the incident laser power in a linear ramp pattern. Power of the heating laser and spectra of thermal radiation from several points across the heated spot were recorded at intervals of between 0.1 to 2 seconds. Heating was repeated at several pressures between 10 GPa and 47 GPa. At any given pressure, heating was repeated several times on different points across the sample. In each heating run, a time sequence of raw (uncorrected) grey-body spectra collected on the CCD (see previous section for description of the laser heating system), laser power and time-stamps of each exposure were saved to a single file for later offline analysis. Spectral range between 600-850nm was used for temperature determination.

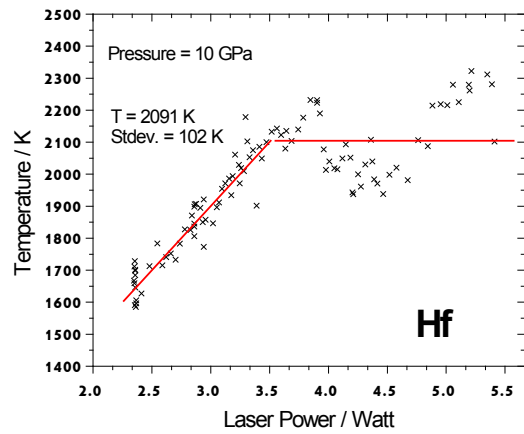
Results and discussion

The temperatures vs. laser power histories from each heating run at various pressures were used to create a P - T map of possible phase transition conditions. For each heating run, by plotting temperature and laser power together one can observe various

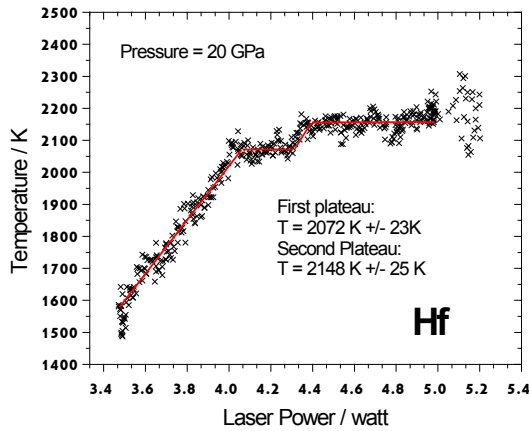
features – such as abrupt changes of slope (e.g. Figure 2.16a), a pronounced yo-yo effect (e.g. Figure 2.16b), a plateau of temperature vs. laser power (e.g. Figure 2.16c) or a combination of these features (Figure 2.16d-f). Visual observation together with statistical analysis was used to determine the average temperatures and temperature uncertainties of various features in each of the acquired temperature vs. laser power measurements.



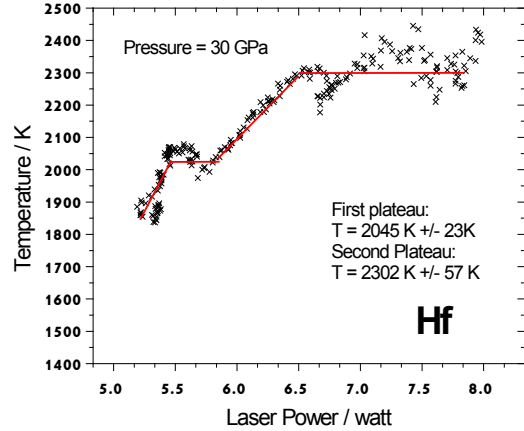
a)



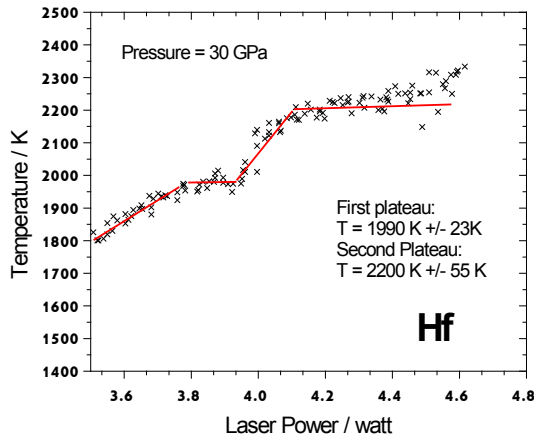
b)



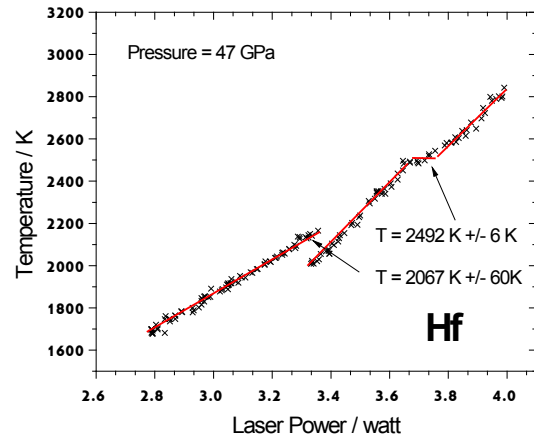
c)



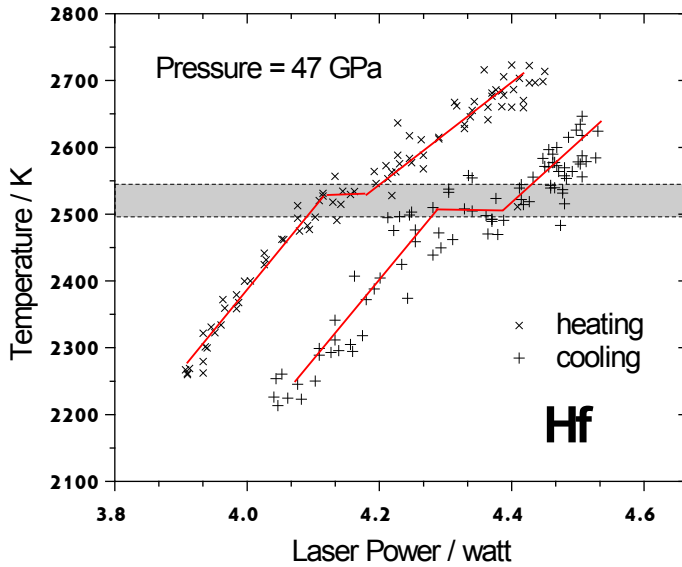
d)



e)



f)



g)

Figure 2.16. Temperature vs. laser power profiles for several laser heating runs at various pressures (P). a, b) $P = 10$ GPa; c) $P = 20$ GPa; d, e) $P = 30$ GPa; f) $P = 47$ GPa; g) $P = 47$ GPa (x – during heating, + - during cooling). Lines are drawn to enhance visual clarity of various heat flow discontinuities.

At a pressure of 10 GPa, each of the heating runs (total 3) exhibited a distinct change in slope in the temperature vs. laser power curve at around 1640K, see Figure 2.16a. This can be indicative of either a phase transition or a change of the surface of the sample due

to a chemical reaction of the sample with the pressure medium. However, hafnium is known to undergo a solid-solid phase transition from a room temperature hexagonally-close-packed to a body-centered-cubic phase at 2053K at ambient pressure. The assumption that there is a phase transition in hafnium at 1640K at 10 GPa is not consistent with literature data. One possible reason for this observation may be a fairly large error in temperature measurement due to an incorrect assumption of wavelength dependence of emissivity of hafnium during spectro-radiometric temperature determination. Another reason could be a reaction of hafnium with the MgO pressure medium. There have been several reports of alkali oxides reactions with transition metals at high P-T (Errandonea, Boehler, et al., 2001), however, I have not found any data on the hafnium – MgO system at high P-T.

Curiously, at higher pressures (20 GPa and up) each of the measured temperature vs. laser power curves shows two distinct plateau-like features at different temperatures, see Figure 2.16c-f. This indicates two distinct changes in the properties of the laser heated material at different temperatures. Initial guess would be that the plateau at a lower temperature is an indication of a solid-solid phase transition, whereas the plateau at higher temperature (or in some cases, yo-yo effect) is an indication of melting. If the temperature vs. laser power features (*TLF*) (i.e. changes in slope, plateaus and ‘yo-yo’ temperature oscillations) are plotted together, as in Figure 2.17a, one can observe a definite correlation between the temperature and pressures at which these features occur. However, the observed *TLFs* are not consistent with the known phase transition and melting temperature of hafnium at 1 bar. As can be seen in Figure 2.17a, the highest temperature observed *TLF* is about 400 K below the melting temperature of hafnium at 1

bar, which is not consistent with the reasoning that these observations indicate melting. However, if the difference of 400 K can be attributed to an error in radiometric temperature determination and corresponding corrections are made, the observed *TLF* can be lined up with the expected phase transition and melting temperatures for hafnium, see Figure 2.17b. This would suggest that there is a triple point of β -phase with the liquid phase around 10 GPa, see Figure 2.17b.

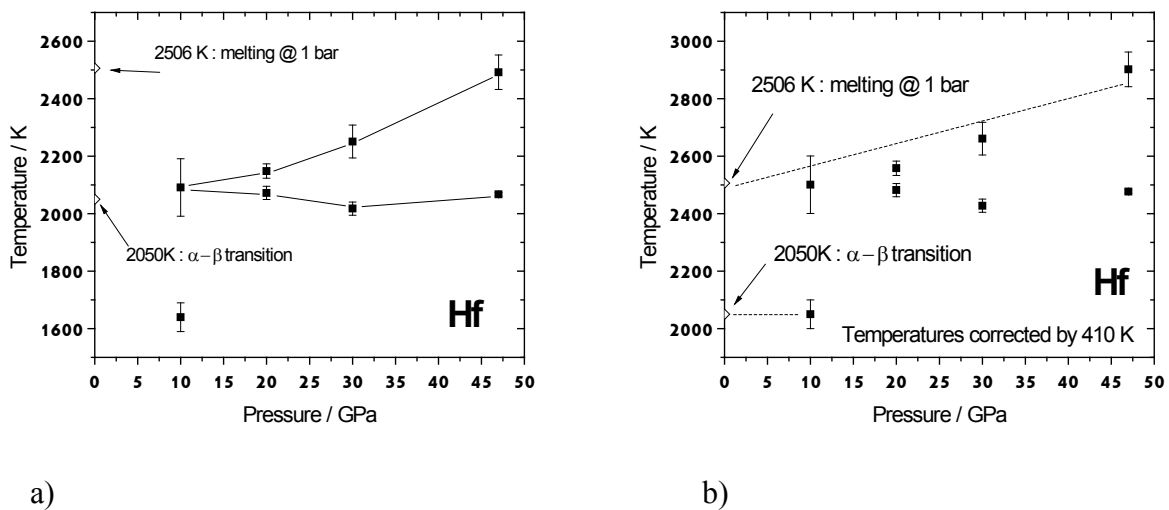


Figure 2.17. P-T map of laser heating features in hafnium

If one makes the assumption that the observed slope change TLF at 1640K is indeed due to the α - β phase transition but the temperature calculation is wrong, it should be possible to precisely determine spectral emissivity of hafnium at this pressure and temperature by estimating the correct temperature of this phase transition using some other method, for example the thermodynamic approach presented in subsequent sections. Moreover, in one heating run the temperatures were recorded during heating as well as gradual cooling. Analogously to the usual heating runs where the laser power was slowly ramped up, during a cooling run after reaching a high temperature the laser power

was gradually decreased with time in a linear ramp pattern. Interestingly, during cooling of the sample, a plateau in temperature was observed at almost the same temperature as during the heating stage, see Figure 2.16g. Cooling curve was recorded during only one experimental run.

Conclusion

The results from this study suggest that the beta phase could have a triple point in contact with the liquid phase and possibly some unknown phase. However, with this data alone it is difficult to be certain whether the temperature-laser-power discontinuities observed at various P-T conditions are due to phase changes in the hafnium sample itself or whether they are due to possible surface reactions between the hafnium sample and the surrounding MgO insulation medium. It is obvious that a separate study of phase transitions and reactions between hafnium and MgO conducted using synchrotron x-ray diffraction is required in order to determine the phase diagram boundaries for hafnium.

2.04 Thermal conductivity of Zr at high pressure and temperature

Introduction

As I have mentioned in the introductory sections, several studies have been attempted before to experimentally determine thermal conductivity of materials in a laser heated DAC. This was done by gradually heating the sample using a laser, measuring the power of the incident laser beam and temperature of a single point on the sample and relating the observations to a numerical heat-transfer model (Konopkova et al., 2011). However, according to my own observations and personal communication with experts in DAC laser heating, it is very difficult to use a single point temperature measurement approach to produce reliable results of thermal conductivities. This consideration was the drive for me to measure multiple-point temperature distribution scans on our laser heated samples. Because of non-repeatability of the DAC loading geometry which can currently be accomplished in typical laboratory conditions and because of difficulties of measurement of actual absorbed laser power, measurements of single point temperatures on a laser-heated sample cannot be used to obtain absolute values of thermal conductivities.

The following section describes an experiment which was specially designed for measuring thermal transport in various materials during continuous-wave (CW) laser-heating in a DAC. The results will show that this technique reproduces the theoretical prediction for thermal behavior of several metals in the laser-heated DAC system (Figure 2.5, Figure 2.6 and discussion). In order to test whether the laser heating system described in the previous sections can be used to measure the predicted heat flow behavior in a sample in a laser heated DAC, I chose two materials that are known to have

sufficiently different ambient condition thermal properties. The first two metals that were chosen are platinum and zirconium whose room temperature thermal conductivities are different by a factor of about 2.

Sample preparation and loading for thermal conductivity measurement

The main consideration in the following type of experiment, as discussed in the previous sections, is that the two metal samples are to be loaded with identical thermal insulation environment. Placing two samples in an identical heat transfer environment simplifies the heat transfer calculations and allows measurement of their relative thermal conductivities. As discussed in the previous sections, the absolute positioning of the samples in the DAC is not as critical as long as the two samples are positioned at identical distances from the diamonds. Thus, two metal foils [platinum (Sigma Aldrich, 99.995%)] and zirconium (Sigma Aldrich, 99.98%)] (dimensions 70x70 μm , 20 μm nominal thickness), whose ambient condition thermal conductivities were assumed to be $k=76 \text{ W}/(\text{m K})$ and $26 \text{ W}/(\text{m K})$ respectively (Kirby, 1991; Milošević and Maglić, 2006), were loaded into a DAC using a side-by-side geometry as shown in Figure 2.18. Diamonds with 400-300 μm diameter culet size were used, gasket hole diameter was 150 μm . Dry powdered MgO, and alternatively powdered ZrO_2 , were used as pressure transmitting and thermal insulation medium. ZrO_2 is one of the hardest known materials and is not usually used as a pressure transmitting medium in a DAC. I found, however, that after applying sufficiently high pressure (around 20 GPa), powdered ZrO_2 becomes optically transparent and suitable for use during laser heating. I found that, in trying to release some of the non-hydrostatic stress created when initially pressurizing ZrO_2 in the loaded cell to achieve transparency, pressure can be decreased by about 30% without

compromising the optical transparency of the ZrO_2 , thus enabling laser heating to be done at lower pressures than pressures required to compress ZrO_2 to optical transparency. In subsequent experimental runs, in order to achieve very uniform and repeatable sample loading geometry, a thin and finely polished disk of MgO was placed as a substrate under the metal foils instead of compressed powder MgO during loading. Thin disks of MgO were prepared by sectioning small sections from a single crystal of MgO using a thin circular diamond saw and subsequently polishing the thin sections to reduce their thickness to about 15 micrometers. Further experiments have shown that using compressed powder MgO substrates instead of thin single crystal MgO disks produced similarly repeatable results. Therefore, compressed powder MgO was primarily used instead of thin single crystal MgO discs in the majority of the subsequent experiments.

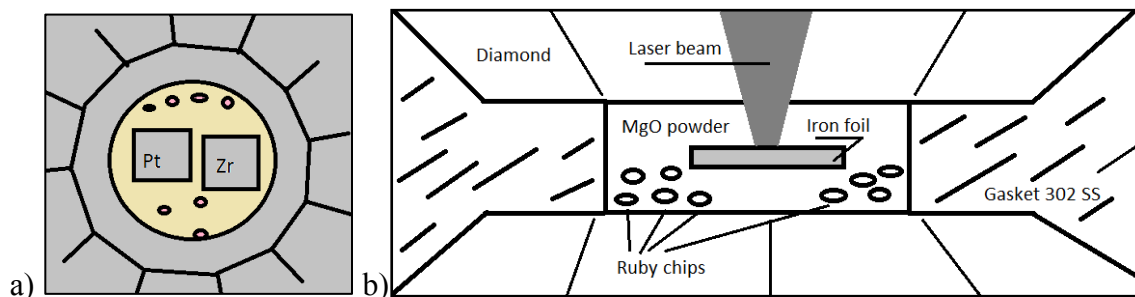


Figure 2.18. Side-by-side sample DAC loading schematic
a) top view; b) profile view

Measuring temperature gradients

The heating was done using the single sided laser heating system in CeSMEC and the temperature was measured using a non-contact radiometric technique described in previous sections. Grey-body emissivity of the sample was assumed. Center points on the samples were laser-heated, in each case by gradually increasing the incident laser power in a linear ramp pattern. Focus of the laser was controlled by visible light observation

from the heated sample, and thus, the narrowness of the focus of the laser beam and the shape of the laser beam were assumed to be the same during each heating. Power of the heating laser and spectra of thermal radiation from multiple-point line scan across the heated spot were recorded at intervals of between 1 to 2 seconds. Figure 2.19 (left) shows a time sequence of temperature line-scan measurements, in this particular case during a gradual decrease (instead of increase) of the power of the incident laser with time. In this intensity plot, the vertical axis corresponds to a position across the heated spot and the horizontal axis corresponds to a time progression of measured temperature distributions. Figure 2.19 (right) shows a typical measured temperature profile at a given time and a given laser power.

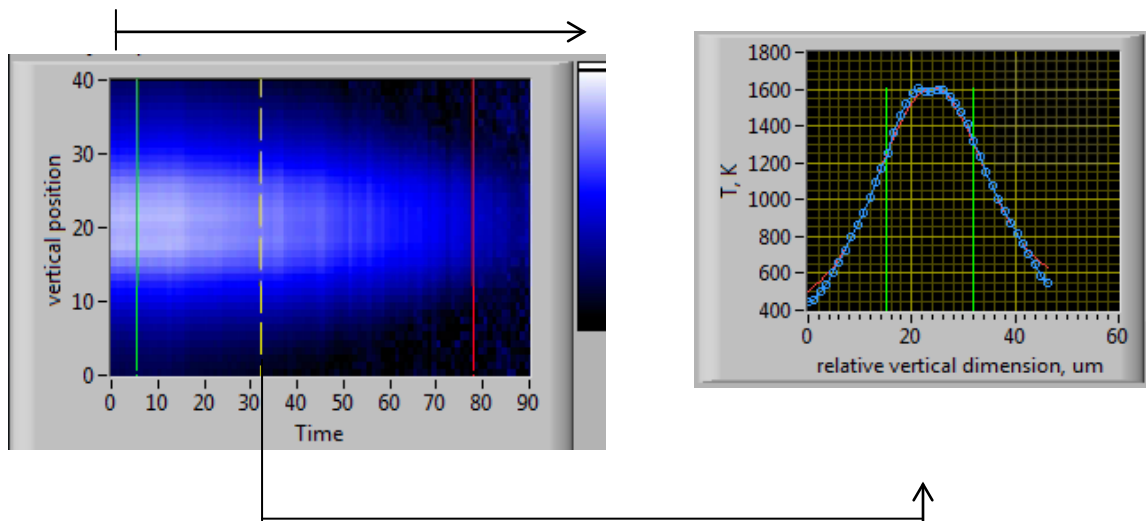


Figure 2.19. Temperature gradients vs. laser power

Left: Temperature distribution across sample is plotted for each exposure taken with linearly decreasing laser power. Right: spatial temperature gradient on the heated sample at a given laser power.

Note on Temperature of Diamonds

Incorrect assumption of temperature of the reverse side of diamonds can adversely affect the accuracy of the numerical heat flow model. Previously, it was assumed that the diamond temperature is at room temperature, or very close. However, for better accuracy of the model, one needs to accurately know the reverse side temperature. Therefore, an experiment was performed to determine the steady state temperature of the diamond face on the reverse side after heating a platinum foil at constant 1500K for 10 minutes with several chosen values of laser power. In the case of our current setup an approximate empirical relationship between the laser power and the temperature of the diamonds can be described by a linear function:

$$T_{\text{diamond face}} \text{ (K)} = 11.9 \text{ (K/watt)} * \text{Power (watt)} + 298.15 \text{ (K)}$$

Of course, this only applies to the current laser heating setup in CeSMEC and needs to be measured separately for each system.

Results and discussion

Qualitative treatment

Initially, the measured temperature distribution was processed in a simplified manner by fitting it to a Gaussian function to approximate the Full Width at Half Maximum (FWHM) of each particular measured temperature distribution. This was done in order to qualitatively see how the hot spot spreads in each of the samples. Figure 2.21 shows the FWHM of the hot spots at various temperatures of platinum as compared to zirconium at various maximum temperatures. The horizontal axis corresponds to the temperature of the hottest point on the laser heated spot (i.e. the center of the hot spot). It is readily seen that the temperature FWHM, and thus the heat spread, is larger in

platinum for any value of highest temperature. This makes sense qualitatively since platinum has a higher value of thermal conductivity, allowing heat to spread more easily through the sample. Conversely, zirconium's lower thermal conductivity means that heat cannot flow as easily through it, causing hottest temperatures to be concentrated in the center of the spot. This first result qualitatively agrees with the theoretical calculations.

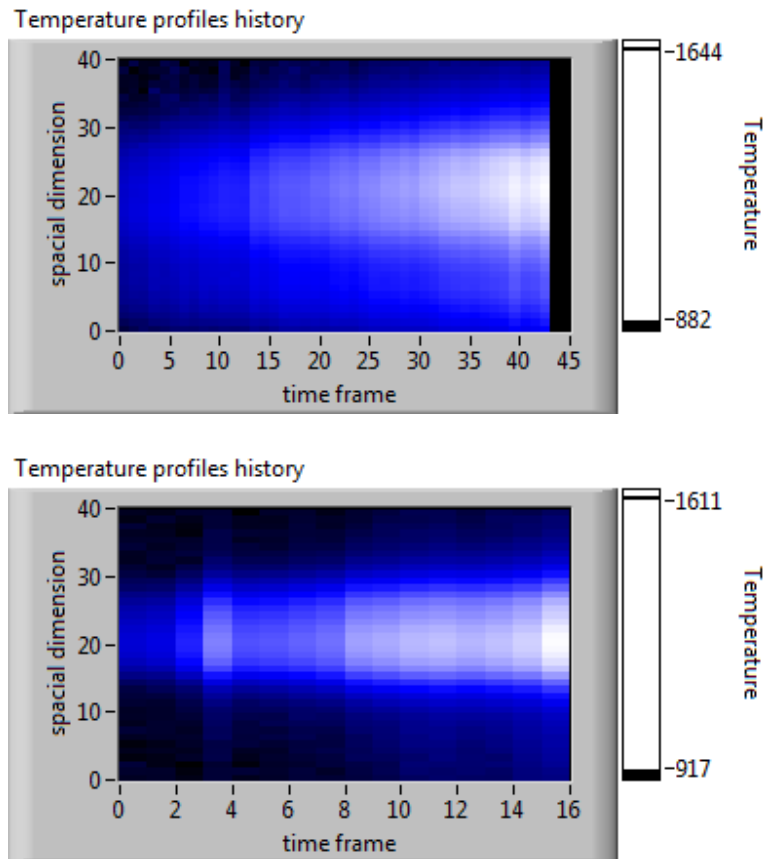


Figure 2.20. Time resolved visual comparison of heat distribution (y-axis) in platinum (up) and zirconium (down) laser heated in a DAC. Zirconium temperature distributions are narrower, indicating a lower thermal conductivity.

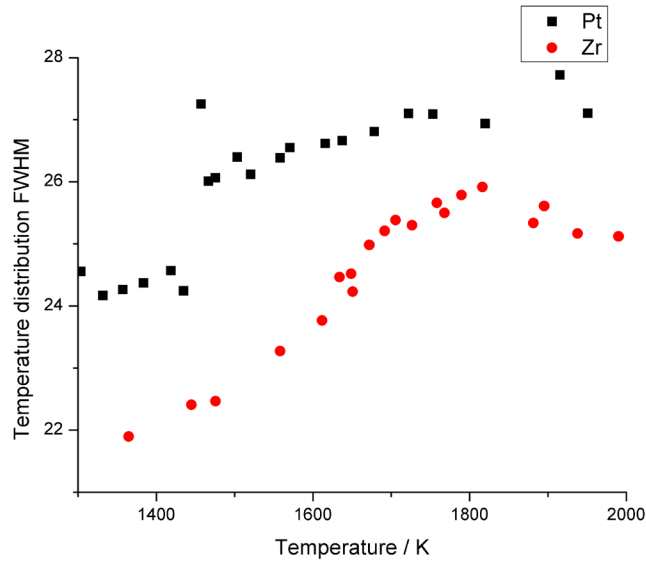


Figure 2.21. Measuring the width of the temperature profiles

Additionally, as can be seen in Figure 2.21, the FWHM of the hot spot on laser heated zirconium levels off and starts to slightly decrease after about 1850K. This indicates that some kind of change has taken place in the heated material, either a solid-to-solid phase transition, melting or possibly a reaction with the surrounding material.

Figure 2.22 shows a relationship between incident laser power and temperature of the hottest point on the sample from several different data sets which were collected during heating platinum and zirconium in MgO and ZrO₂. As was predicted by the numerical heat transfer model described in the earlier sections of this thesis, more laser power is required to heat platinum to a given highest temperature as compared to zirconium. It is difficult to compare the effects of different insulation media on the laser power vs. temperature relationship because the heating in the two cases has been done at different pressures. Moreover, the thickness of the insulation layers in the two cases was not controlled to be the same.

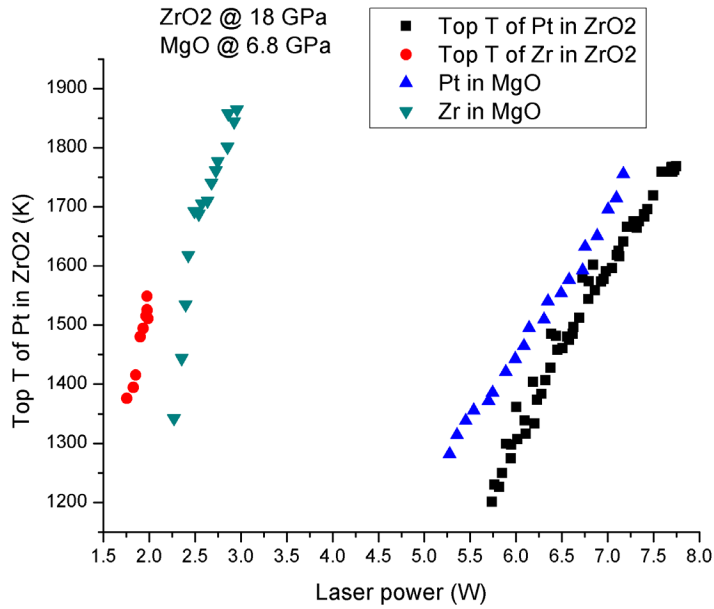


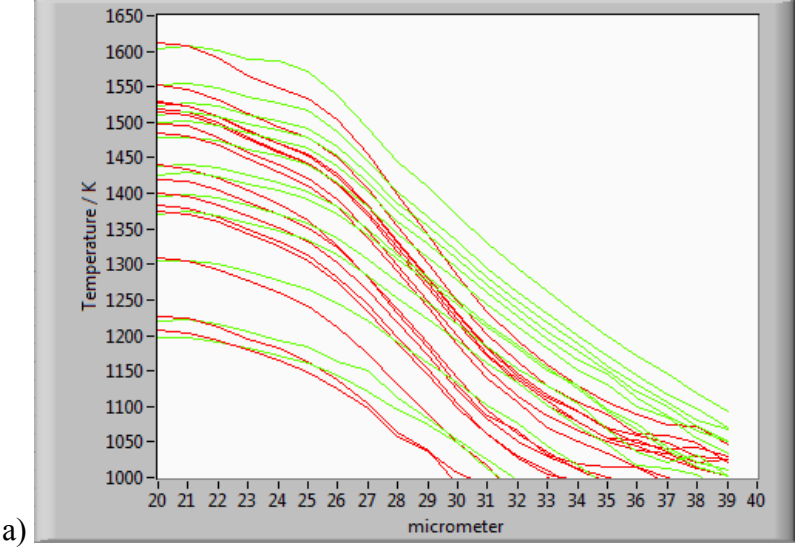
Figure 2.22. Heating platinum and zirconium in different insulation media.

Quantitative heat flow calculations

After observing a qualitative agreement between my experimental measurements and theoretical predictions, I used my numerical heat-transfer model which was described in previous sections to determine the relative thermal conductivities of platinum and zirconium based on the measurements of lateral heat distributions at different powers of the incident laser.

Temperature dependence of thermal conductivity of platinum was taken from literature as: $k(T) = a_0 + a_1 T + a_2 T^2 + a_3 T^3$, with $a_0 = 73.9963$, $a_1 = -0.01558$, $a_2 = 2.65e-5$, $a_3 = -6.13e-9$ (Kirby, 1991). Pressure dependence of thermal conductivity of platinum was ignored for the sake of simplicity of testing my model. In general, the pressure dependence of platinum is not expected to be zero, however, and needs to be taken into account in full analysis. Using the experimentally measured temperature gradients for platinum, I constrained other unknown heat transfer model parameters.

Then I used the constrained model parameters to predict thermal conductivity of zirconium by fitting only the measured temperature gradients to the model with thermal conductivity of zirconium as the only free parameter. The result of the fitting can be seen in Figure 2.23 and Figure 2.24. By constraining the model parameters by using platinum as a calibration standard and assuming (for simplicity) a constant value of thermal conductivity of zirconium, the least square fitting of the measured data to the numerical heat transfer model gives a value of $k = 18 \text{ W}/(\text{m K})$ for zirconium, which is somewhat lower than the reported room temperature value $23 \text{ W}/(\text{m K})$. Of course, this value depends on the thermal conductivity of platinum which was assumed and not measured. Therefore, it can only be said that the obtained value of k for zirconium is lower relative to platinum by a factor of 0.225 at 18 GPa and 1200K. However it may be possible to further improve the fitting by assuming a linear dependence of thermal conductivity of the unknown metal instead of trying to fit a constant value and thus obtain a functional form of $k(T)$.



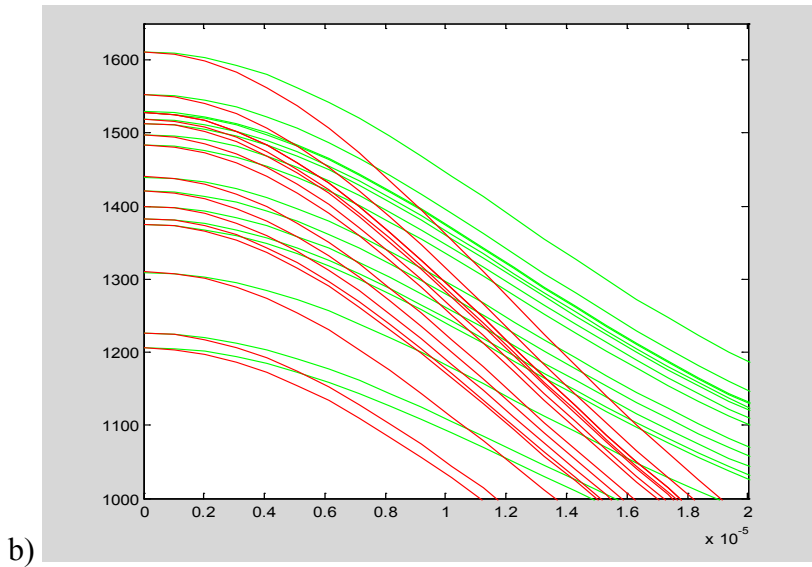


Figure 2.23. a) Measured temperature gradients at various laser powers for Pt and Zr. Temperature gradients in Pt (Green) are seen to be more spread-out temperature gradients of Zr (Red), pressure = 18 GPa; b) Calculated temperature gradients at various laser powers for Pt and Zr. Thermal conductivity of platinum used in this calculation were obtained from literature (Kirby, 1991).

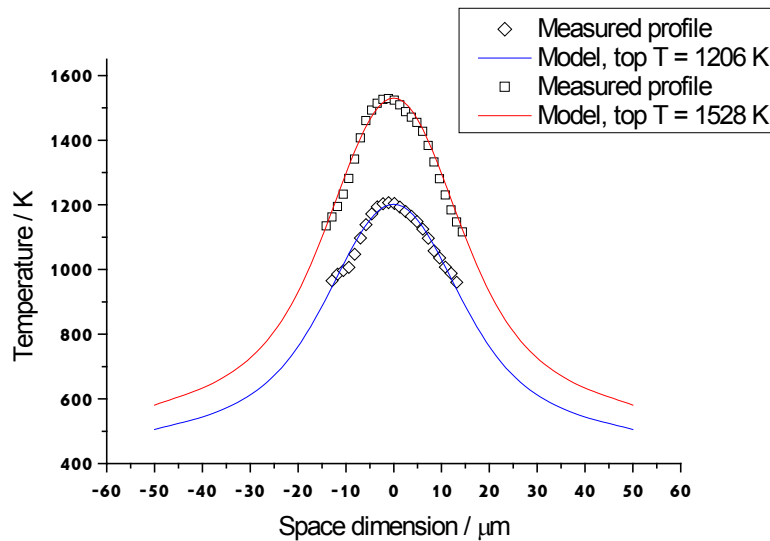


Figure 2.24. Numerical model fit to the measured temperature gradients of zirconium. Model parameters are constrained using thermal parameters of platinum. Thermal conductivity, $k(T)$, of zirconium is the only free fitting parameter.

CONCLUSION

There are two parts of this dissertation. In Part I of this dissertation I have described a systematic study of several transition elements to understand their high-temperature and high-pressure phase equilibria and thermophysical properties in a series of experiments utilizing synchrotron x-ray diffraction. Over the course of the study, a unique thermodynamic database was created for 13 common transition metals (Ti, Zr, Hf, Mo, W, V, Nb, Ta, Pd, Pt, Cu, Ag, and Au) which has:

- All the thermochemical data on these elements in their standard state (mostly available and compiled)
- All the equations of state (EoS) formulated pressure-volume-temperature data (some from literature, others measured as a part of this study)
- Complete thermodynamic data for selected elements from standard to extreme conditions
- Phase diagrams from thermodynamic equilibrium calculations consistent with experiments
- Thermophysical properties (C_p , H , S , G) of the high P - T ω -phase of Ti, Zr and Hf were determined during the optimization of the EoS parameters and are presented in this study. These results should have important implications in understanding hexagonal-close-packed to simple-hexagonal phase transitions in transition metals and other materials.

The so-called explicit Gibbs free energy EOS was used to calculate the high-pressure properties of several elements, based on CALPHAD methodology. The

proposed EoS uses an interpolation with a Thomas–Fermi model and does not show any negative values for heat capacity. EoS parameters were calculated for 13 transition elements. High-pressure shock wave data show a major discrepancy with calculated Hugoniot results, but this may be due to uncertainty and lack of accuracy of the shock wave data at high pressure.

Optimized *EoS* parameters can be used as the input for *ChemSage* (Eriksson and Hack, 1990) or *FactSage* (Bale et al., 2009) thermodynamic software to calculate all thermodynamic properties at high *P-T* conditions. For readers who do not have access to either *ChemSage* or *FactSage* software, I include tabulated values of all thermodynamic and volume data for Ti, Zr and Hf at high pressures and temperatures in the APPENDIX.

In Part II of this dissertation, I have described an improved experimental system to measure effects of high pressure and high temperature on changes in thermal transport properties of materials was designed and tested. I have described theoretical calculations and presented a novel an experimental design to measure thermal transport in materials in a laser heated diamond anvil cell. Using the newly installed measurement system, I performed measurements on several chosen metals (zirconium and platinum), and for the first time, determined relative values of their thermal conductivity at simultaneous high temperature and high pressure conditions. Least-squares fitting of the measured data to the numerical heat-transfer model produced relative values of thermal conductivities that are consistent with ambient conditions data available in the literature (Kirby, 1991; Milošević and Maglić, 2006).

Future directions of this research, namely - the improved ability to quantitatively measure relative thermal conductivities, should also include studies of geologically

important materials at high temperature and pressure conditions. The research presented in this dissertation should have important implications for earth sciences because the ability to characterize the relative thermal conductivities of different materials within the Earth should aid in constraining the heat flow within the Earth and improve the understanding of its history and evolution.

APPENDICES

APPENDIX: Related studies at high pressure and supplemental materials

Studies which are described in APPENDIX I and APPENDIX II were done concurrently with the work presented in PART I and PART II in this thesis. They are strictly a part of this thesis because they do not exactly fit in the main theme of this dissertation which focuses on thermophysical properties of materials at high pressures and high temperatures. However, because of the importance and novelty of the results obtained in these high pressure studies and the invaluable experimental and theoretical experience which I acquired while working on them, I include them in the APPENDIX.

APPENDIX I: High pressure study of SrVO₃ and CaVO₃ perovskite oxides

Abstract

The effect of high hydrostatic pressure on SrVO₃ and CaVO₃ perovskite oxides has been investigated by synchrotron X-Ray diffraction in a diamond anvil cell at room temperature and by first principles calculation. It was shown that SrVO₃ crystal structure, space group *Pm-3m*, is stable to at least 29GPa; and CaVO₃ crystal structure, space group *Pnma*, is stable to at least 18GPa; i.e. no phase transitions were observed in the pressure range studied. Compressibility calculated by first principles agrees very well with experimentally measured values for SrVO₃ but is overestimated in the case of CaVO₃. [Bulk modulus was determined experimentally and correspondingly with first principles calculations by fitting of the isothermal Birch-Murnaghan equation of state. For SrVO₃ it was found that bulk modulus $\{B_0, B_0'\} = \{177.1, 4.52\}$ (first principles), $\{B_0, B_0'\} = \{177.2, 4.51\text{fixed}\}$ (experiment); and for CaVO₃ $\{B_0, B_0'\} = \{184.2, 4.3\}$ (first principles), $\{B_0, B_0'\} = \{210.5, 4.3\text{fixed}\}$ (experiment). As was expected, first principles calculation and Rietveld refinement of experimental X-ray diffraction data has shown that compression of CaVO₃ is mostly due to tilting of the V-O octahedra. Non-hydrostatic effects, i.e. differential stress, of SrVO₃ was analyzed by applying the lattice strain theory.

Introduction

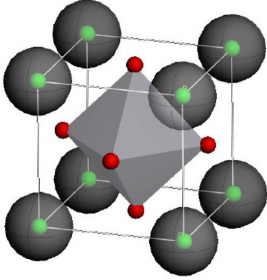
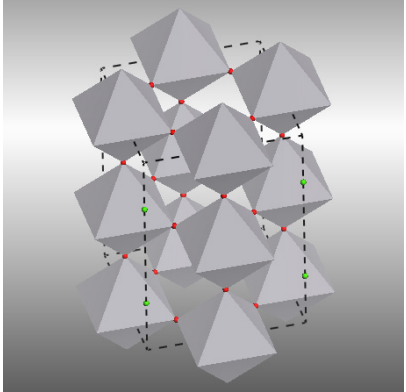
Transition metal oxides which normally crystalize in the ABO₃ perovskite structure are well known to exhibit many interesting properties and have a large range of possible applications. Perovskites can be widely applied because depending on their electronic structure, they can be dielectric, ferroelectric, semiconducting, superconducting (Yamanaka, 2004), and among other qualities, can have excellent

oxygen ion mobility at elevated temperatures (Hsu et al., 2006). Materials with distorted perovskite structures exhibit colossal magnetoresistance; they have been considered as potential materials for holographic data storage. Both CaVO_3 and SrVO_3 are strongly correlated metals which have been used as study cases to understand electronic correlation in solids (Odier et al., 1995; Ueda, 1998; Falcon, 2004; Nekrasov et al., 2005).

Crystal structure which gives rise to the great variety of physical properties of perovskites can change with pressure, temperature and chemical composition and substitution. Phase transitions in perovskite associated with change of pressure are still a subject of investigation. It has been suggested in literature that relative compressibility of the octahedra in various perovskites influences the thermodynamics of their phase transitions and therefore should be taken as a general rule for predicting their high temperature and pressure behavior (Angel et al., 2005). ABX_3 perovskites typically crystallize in one of several crystallographic space groups, most commonly $Pbnm$, $R-3c$ and $Pm3m$ (Glazer, 1972). Depending on tilting and compressibility of the B-O octahedra perovskites can undergo phase transitions either from higher to lower or from lower to higher symmetries with changing pressures and temperature. Under ambient pressure, SrVO_3 and CaVO_3 were known to crystallize in $Pm-3m$ and $Pbnm$ respectively (Falcon, 2004; Maekawa et al., 2006). These perovskites have not been previously studied under high pressure. In this study I calculate and experimentally measure the compressibilities of CaVO_3 and SrVO_3 and show that their ambient condition phases are stable at least to pressures which were achieved in the experiment. The presented results should find some

future use in extending theoretical understanding of structural behavior of perovskites and their phase transitions.

Table A-I.1. Structures of SrVO₃ and CaVO₃

	SrVO ₃	CaVO ₃
Symmetry	Cubic	Orthorhombic
Space group	P m -3 m	P n m a
Lattice parameter	a = 3.86	a = 5.37 b = 7.63 c = 5.37
3-D atomic schematic	Ca: green, V: octahedral centers, O: red	Ca: green, V: octahedral centers, O: red
		
Atomic positions (fractional):	Sr: 0 0 0 V: 0.5 0.5 0.5 O: 0.5 0 0.5	Ca: 0.973, 0.25, 0.495 V: 1, 0.5, 1 O: 0.989, 0.75, 1.058 O: 0.716, 0.469, 1.058

Experiment and first principles calculation

Sample preparation

Polycrystalline CaVO₃ and SrVO₃ were synthesized by the citrate precursor method adopted from H. Falcon et al (Falcon, 2004). Starting reagents were CaCO₃ (SrCO₃) and V₂O₅ all 99% min. purity. V₂O₅ was dissolved in NH₄OH solution at room temperature, CaCO₃ (SrCO₃) were dissolved in citric acid solution at slightly elevated temperature. Then, two solutions, NH₄VO₃ and Ca (Sr) citrate were mixed together and slowly evaporated until blue organic resin was formed. The citrate resin was slowly

decomposed on a hot plate and then fired in air at 800°C for 1h. CaVO₃ (SrVO₃) perovskites were produced by reduction of the precursor at 1050°C for 12 h in 5% H₂/Argon flow.

X-ray diffraction

X-ray diffraction measurements of CaVO₃ under pressures of up to 16.8 GPa and of SrVO₃ up to 28.1 GPa were conducted using a MAR3450 imaging detector on the B2 beamline ($\lambda = 0.48595\text{\AA}$) at Cornell High Energy Synchrotron Source. Measurements at high pressure were carried out using the diamond anvil cell (DAC) of Mao-Bell type (Jayaraman, 1986) with diamonds 400 μm diameter culet. Typical exposure times for x-ray diffraction collection were in the range between 5 to 30 min. A 4:1 methanol-ethanol mixture was used as a pressure transmitting medium. Pressure inside the cell was measured using the ruby fluorescence technique. Sample to detector distance and other diffraction geometry parameters were calibrated using a CeO₂ standard. 2D angle-dispersive diffraction images were processed using the software FIT2D (Hammersley, 2009) to generate the intensity versus two-theta diffraction patterns. Each diffraction peak was indexed and fitted with a pseudo-Voigt function to determine its *d*-spacing. To determine the *a*, *b* and *c* lattice parameters of CaVO₃, *d*-spacings of diffraction peaks (101), (111), (200), (321), (400) were fitted using least-squares to an orthorhombic *Pbnm* lattice. To determine the *a* lattice parameter of the cubic SrVO₃, the *d*-spacings of diffraction peaks (100), (110), (111), (200), (210), (211) and (220) were fitted using least squares to a cubic *Pm-3m* lattice.

First principles modeling of high pressure effects

Theoretical calculations to predict compressibility of CaVO_3 and SrVO_3 were performed using the CASTEP first-principles calculation software (Clark et al., 2005). Geometry optimization calculations, which allow the calculation of lattice parameters at a given pressure, were performed at a multitude of non-monotonically decreasing pressure points to simulate an experimentally obtainable pressure-volume data set. GGA-PBE functional and ultrasoft pseudo-potentials were used for all calculations. Other calculation input parameters are summarized in Table II. Initial geometry optimization was done assuming zero external pressure to obtain the first data point. The output lattice parameters of the first optimization were used as input for the subsequent optimization at increased external pressure. Each subsequent output was used as an input for the next higher pressure step. The calculations performed in this study were adopted from a robust technique which has been described by others including Milman et al (Milman et al., 2000). For CaVO_3 as well as SrVO_3 , geometry optimization calculations were done with exponentially increasing pressure steps up to 40 GPa. All first-principles calculations described herein were done at 0 K.

Table A-II.2. Structures of SrVO_3 and CaVO_3 , theoretical calculation
Summary of first principles calculation parameters for CaVO_3 and SrVO_3

	CaVO_3	SrVO_3
Symmetry	Orthorhombic	Cubic
Space group	$P n m a$	$P m -3 m$
Lattice parameter	$a = 5.37, b = 7.63, c = 5.37$	$a = 3.86$
Atomic positions (fractional x, y, z):	Ca: 0.973, 0.25, 0.495 V: 1, 0.5, 1 O: 0.989, 0.75, 1.058 O: 0.716, 0.469, 1.058	Sr: 0, 0, 0 V: 0.5, 0.5, 0.5 O: 0.5, 0, 0.5

Results

Representative diffraction patterns are shown in Figure A-I.1. Rietveld refinement of x-ray diffraction data at ambient pressure shows that lattice parameters of CaVO_3 and SrVO_3 measured in this study agree with the literature reported value within the experimental error. Figure A-I.2 shows the output from EXPGUI Rietveld refinement software for SrVO_3 .

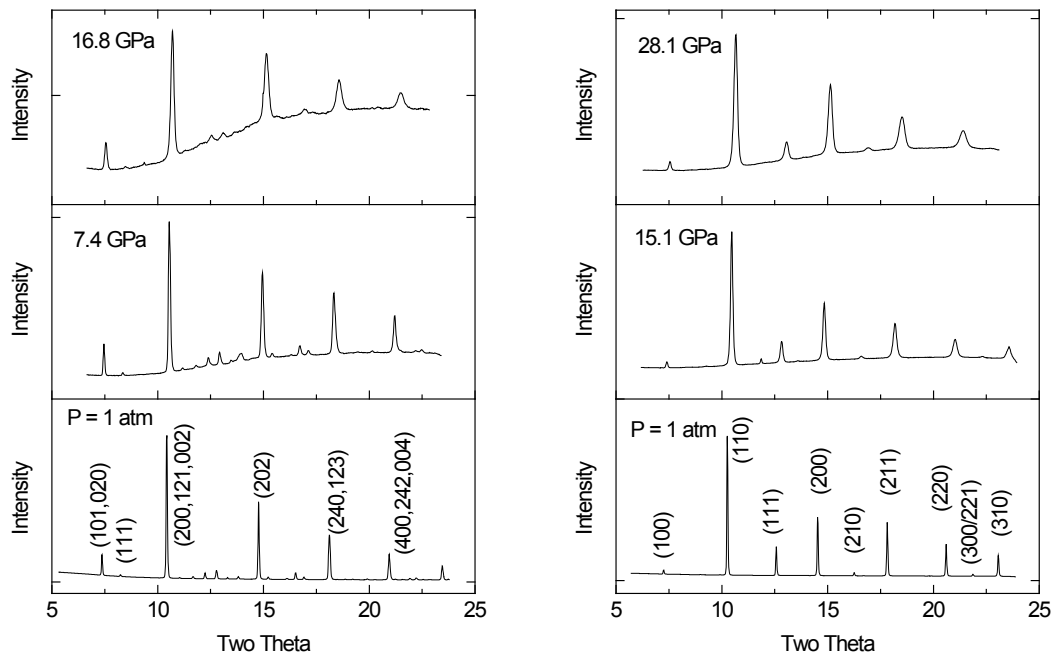


Figure A-I.1. Representative diffraction patterns and indexing of CaVO_3 (left) and SrVO_3 (right).

Rwp = 6.36% Rwp(w/o bck) = 6.37% Rp = 14.38%

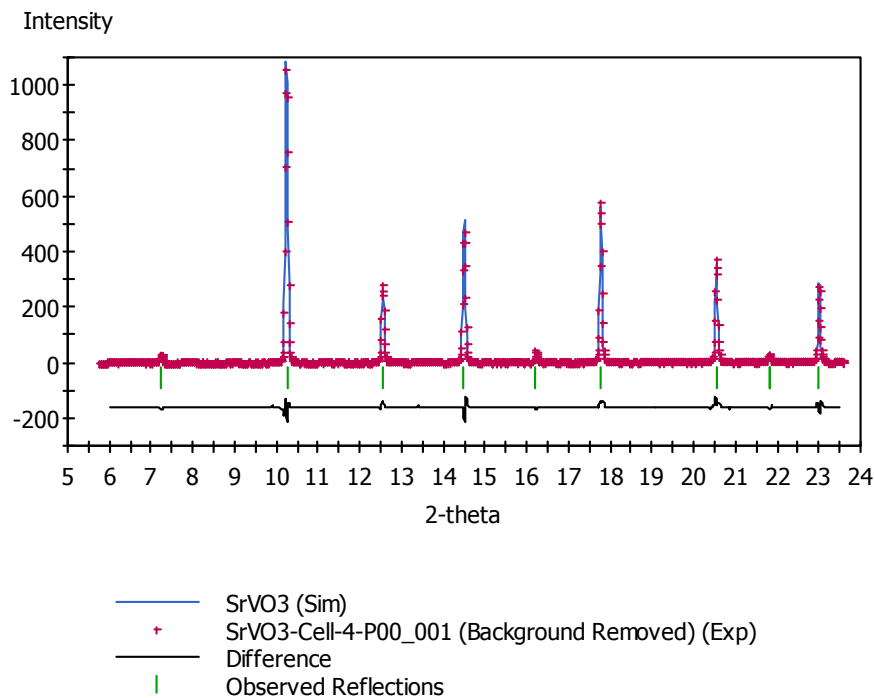


Figure A-I.2. Rietveld refinement of SrVO₃, pressure = 1 bar.

The pressure dependence of lattice parameters obtained by first principles calculation and by experiment was fitted with least squares method to the third-order Birch-Murnaghan isothermal equation of state ($P = 3/2B_0[V/V_0]^{-7/3} - (V/V_0)^{-5/3}\{1 + 3/4(B_0' - 4)[(V/V_0)^{-2/3} - 1]\}$ EQ. 1-6, section 1.02) (Birch, 1978).

For SrVO₃ it was found that bulk modulus $\{B_0, B_0'\} = \{177.1, 4.52\}$ (first principles), $\{B_0, B_0'\} = \{177.2, 4.51\text{fixed}\}$ (experiment); and for CaVO₃ $\{B_0, B_0'\} = \{184.2, 4.3\}$ (first principles), $\{B_0, B_0'\} = \{210.5, 4.3\text{fixed}\}$ (experiment).

Calculated and experimentally measured pressure dependence volumes of SrVO₃ and CaVO₃ are shown in Figure A-I.3.

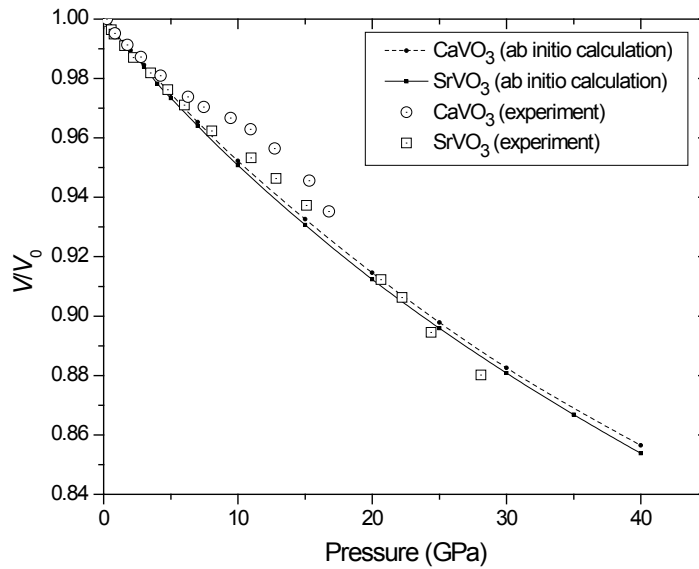


Figure A-I.3. Compression of SrVO₃ and CaVO₃

Summary and conclusions

The effect of high hydrostatic pressure on SrVO₃ and CaVO₃ perovskite oxides has been investigated by synchrotron X-Ray diffraction in a diamond anvil cell at room temperature and by first principles calculation. It was shown that SrVO₃ crystal structure, space group *Pm-3m*, is stable to at least 29GPa; and CaVO₃ crystal structure, space group *Pnma*, is stable to at least 18GPa; i.e. no phase transitions were observed in the pressure range studied. Compressibility calculated by first principles agrees well with experimentally measured values for SrVO₃ but is overestimated in the case of CaVO₃.

APPENDIX II: Exploring properties of nano-materials using high pressure:

The high-pressure structural properties of ZnO bulk and nano crystals

Abstract

The elastic properties of high quality ZnO crystals and nanopowder of grain size of about 65 nm are studied for both wurtzite (low pressure) and rock-salt high pressure phases. The measured values of bulk moduli for wurtzite and rocksalt phases of bulk ZnO crystals are equal to (156 ± 13) and (187 ± 20) GPa, respectively, and considerably larger for ZnO nano-crystals. The phase transition begins at pressure of about 9 GPa and it is completed at pressure of about 13.8 GPa for bulk crystals, whereas the values of pressure at which the phase transition occurs are lower for nano-crystals. Carefull Rietveld analyzis of the obtained data does not exhibit presence of any intermediate phases between low-pressure wurtzite and high-pressure rock salt phases of ZnO. The phase transition is accompanied by a strong decrease of the near band-gap photo-luminescence intensity. In addition, the pressure coefficient of the near-band-gap luminescence in ZnO nano-crystals exhibits strong deviation from the linearity observed in bulk crystals. Analysis of the results shows that defect present in the nanopowdered sample are responsible for the observed effects.

Introduction

The zinc oxide, zinc magnesium oxide and zinc cadmium oxide compounds have gained substantial interest in recent years. Zinc oxide is a direct wide band gap semiconductor material ($E_g=3.37$ eV) with a large exciton binding energy of 60 meV for bulk crystal, which could be easily increased in a quantum wells system. ZnO is nearly lattice matched to GaN which makes this material attractive for future developments of optoelectronic, spintronic, and sensor application. ZnO in polycrystalline form is commonly used in industry for producing pigments in paints, rubber, sunscreens and

sunblocks, varistors and medicines. However, it is not easy to grow large ZnO monocrystals of good quality due to many defects which occur in bulk crystals. Among the defects which are observed in this material, the oxygen vacancies are the most common (McCluskey and Jokela, 2009; Klingshirn et al., 2010).

The structural properties of ZnO crystals under hydrostatic pressure have already been studied for many years (Jaffe and Hess, 1993; Gerward and Olsen, 1995; Karzel et al., 1996; Ahuja et al., 1998; Recio et al., 1998; Desgreniers, 1998; Decremps et al., 2000, 2003; Jaffe et al., 2000; Mori et al., 2004; Liu et al., 2005). It is known that at hydrostatic pressures of about 9 to 13 GPa the phase transition from wurtzite (B4) to rocksalt phase (B1) occurs. Interesting behavior of this phase transition was predicted by Boulfefel and Leoni (Boulfefel and Leoni, 2008). Their theoretical calculation predicts that an intermediate tetragonal phase should appear between the B4 and B1 phases. Established values of bulk moduli for both phases are quite scattered and vary from about 135 GPa to about 180 GPa for wurtzite phase and from 132 to about 230 GPa for rocksalt phase. One of possible reasons for such large scattering of the values of bulk moduli could be associated with the quality of the sample material. Samples could contain a large number of intrinsic defects, which are difficult to control. The phase transition pressure and the existence of the intermediate phase between the B4 and B1 phases can also be related to the sample quality and the existence of uniaxial pressure components in the pressure-transmitting medium (PTM). I would like to compare the elastic properties under high hydrostatic pressure of very good quality bulk ZnO crystals with those of ZnO nanocrystals prepared by evaporation of coarse grained commercially available oxide powder into a radio-frequency air plasma and nanostructured with solar physical vapor

deposition process (SPVD) (Aitahcene et al., 2007). The pressure-induced phase transitions strongly affect luminescence properties of ZnO crystals, effectively quenching bulk crystal luminescence and broadening luminescence emitted from nanocrystalline samples. This aspect of pressure influence on luminescence properties of ZnO samples is discussed in the paper.

Bulk crystals of ZnO can be grown by different techniques such as vapor phase transport, hydrothermal and pressure melt method. The largest crystals have been obtained by a hydrothermal method. In this method an aqueous solution together with a KOH and LiOH are used as a solvent for the ZnO seeds. Unfortunately, the hydrothermal crystals incorporate alkali metals, mostly K and Li and small amounts of metallic impurities from the autoclave. A common method to produce very high quality ZnO crystals wafers is based on vapor transport, however in this case the dimensions of crystals which can be obtained are limited to a few centimeters.

Remarkably large ZnO crystals, up to 2 kg in weight, have been found during industrial production of zinc white in Olawa Foundry in Olawa, Poland. Properties of these crystals have been reported elsewhere only once and have been looked at as rather a mineralogical curiosity (Nowak et al., 2007). Industrial production of zinc white in Olawa Foundry is performed by a method known as the French process. The system consists of two chambers, the upper part being the combustion chamber where natural gas is burned to produce heat. In the upper chamber the temperature rises to about 1500 °C and it is separated from a bottom chamber by a ceramic diaphragm. Metallic zinc is melted and vaporized in a bottom chamber at a temperature above 907 °C. Zinc vapor is overheated to 950°C and leaves the chamber into the oxidation chamber where it

instantaneously reacts with the oxygen in the air to give ZnO particles with an average size of a few micrometers. A periodic shutdown of the facility for physical inventory verification reveals that the diaphragm and vaporization chamber is covered by remarkably large ZnO crystals. Due to the fact that these large ZnO crystals have excellent optical properties, described in the next part of this paper, samples of this material were used in our high pressure experiments.

The nanopowder ZnO samples were prepared by evaporation of mixtures of coarse grained oxides in an inductively coupled plasma. The obtained ZnO powder with a grain size of about 1 μm was subsequently nanostructured by the solar physical vapor deposition process with the use of a Heliotron sun reactor in the High Flux Solar Facilities at the CNRS Laboratoire Procédés, Matériaux et Énergie Solaire (PROMES), Odeillo/Font Romeu (France). The 1 μm grained ZnO powder was pressed into small pellets and placed in the sun reactor in a vacuum glass chamber. The sample was illuminated by the focused sunlight with power density of about $(730 \pm 100) \text{ W/cm}^2$. The sample underwent sunlight ablation and was deposited by condensation on a water cooled copper tube ('cold finger') located few centimeters above the target and on a ceramic filter. The final product was finally scratched from the cold finger and the filter. SEM picture of the powder is shown in Figure A-II.1. The details of the process are described in references (Grigorjeva et al., 2007; Kalinko et al., 2007).

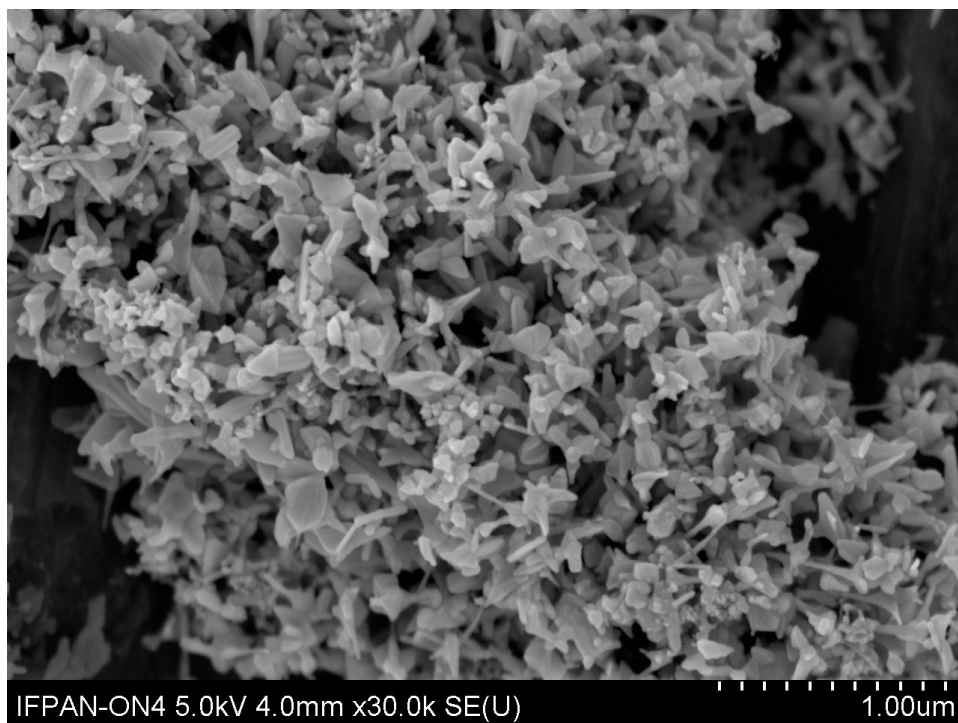


Figure A-II.1. SEM picture of ZnO nanopowder after SPVD process in solar reactor (Duzynska, Hrubciak, Drozd et al., 2012)

The photo-luminescence (PL) spectra of ZnO samples were obtained using a 325-nm (3.81 eV) line of a He-Cd 15 mW laser as the excitation source. The spectra were measured with the use of a Horiba Jobin-Yvon FHR 1000 monochromator with a charge coupled device (CCD) detector. The spectra were corrected for the quantum efficiency of the detector. The high-pressure measurements were performed with use of a low-temperature diamond anvil cell (Diacell Products MCDAC-2) loaded with argon as a pressure-transmitting medium. The diamond anvil cell was mounted into an Oxford Optistat CF cryostat and measurements were performed at 11K. The *R1*-line ruby luminescence was used for pressure calibration. Polished samples of bulk ZnO crystals with a thickness of about 30 μm or ZnO nanopowder were loaded into the cell along with

a small piece of ruby. The changes of pressure were done at room temperature in order to minimize nonhydrostatic effects.

X-ray diffraction measurements of bulk crystalline ZnO were conducted on the beamline IDB-16 ($\lambda = 0.398\text{\AA}$) of the Advanced Photon Source (APS) at Argonne National Laboratory. Diffracted x-rays were collected at Bragg angles of up to $2\Theta=25^\circ$ using a MAR3450 imaging detector. One series of measurements for bulk ZnO crystal was performed in neon gas as a pressure transmitting medium (PTM) in order to check the effects of possible non-hydrostaticity. The results obtained in neon and in Poly(dymethylsiloxane) (silicone oil, viscosity 5cSt) are consistent with each other, which means that the effects of non-hydrostaticity are rather weak and similar for both used pressure-transmitting media. A symmetrical type diamond anvil cell (DAC) with 300 μm culet diameter diamonds was used for measurements with neon and a Mao-Bell (Jayaraman, 1986) type DAC with 400 μm culet diameter diamonds was used for measurements with silicone oil.

X-ray diffraction measurements of ZnO nanopowder under pressures of up to 15 GPa were conducted using a MAR3450 imaging detector on B2 beamline ($\lambda = 0.48595\text{\AA}$) at Cornell High Energy Synchrotron Source. Measurements at high pressure were carried out using the diamond anvil cell (DAC) of Mao-Bell (Jayaraman, 1986) type with 400 μm culet diameter diamonds. Typical exposure times for x-ray diffraction collection were in the range between 450 to 600 seconds. Silicone oil was used as a hydrostatic pressure transmitting medium.

Sample to detector distance and other diffraction geometry parameters were calibrated using a CeO_2 standard. 2D angle-dispersive diffraction images were processed

using the software FIT2D (Hammersley, 2009) to generate the intensity versus two-theta diffraction patterns. Each diffraction peak was fitted with a pseudo-Voigt function using FITYK software (Wojdyr, 2010) to obtain its 2-theta angle. To determine the a and c lattice parameters of *wurtzite* phase of ZnO, d -spacings of diffraction peaks (100), (002), (101), (102), (110) and (103) were fitted using least-squares to a hexagonal lattice. Lattice parameter of the cubic *NaCl*-phase ZnO was determined using an arithmetic average of d -spacings of diffraction peaks (111), (200), (220), (311) and (222). Platinum was used as an *in situ* pressure marker. Similarly, lattice parameter of the platinum pressure marker was calculated using 4 non-overlapping diffraction peaks – (111), (200), (220) and (311). The pressure was calculated using an equation of state of platinum proposed by Fei et al. (2007)

Results and discussion

Figure A-II.5 illustrates the emission spectra of the bulk crystals of ZnO at temperature of 10 K and ambient pressure in comparison with the nanocrystalline sample. In the case of bulk crystals all exciton lines are clearly visible. At higher energy, observed peaks were probably due to upper ($UPB_A=3.3678$ eV) and lower ($LPB_A=3.3636$ eV) polariton branches of A exciton. Excited state transition of exciton A are visible at $FX_A^{n=1}=3.3659$ eV and $FX_A^{n=2}=3.3780$ eV, for Γ^6 band symmetry. The weak emission centered at $FX_B^{n=1}=3.3738$ (Γ^6 symmetry) is assigned to the B exciton transition. Moreover two main sharp lines with FWHM of 0.5 meV are related to two excitons bound on unidentified neutral donors.

The near-band-gap low temperature emission of nanocrystalline ZnO forms a broad band with a maximum at about 3.3 eV, showing some unresolved bands, most

probably associated with bound exciton luminescence and some phonon replicas of the exciton lines. Apparently, quality of such samples is not as good as that of bulk crystals. Some stress and defects existing in small nanocrystals may contribute to the broadening of the luminescence of nanocrystalline sample as compared with the bulk material (Desgreniers, 1998; Recio et al., 1998; Fidelus et al., 2012).

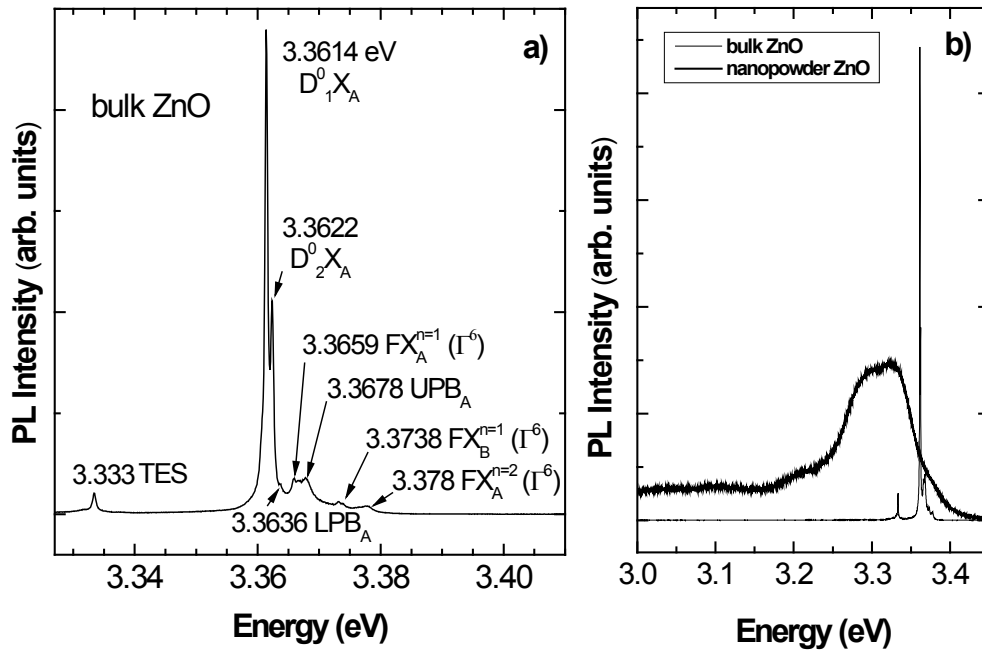


Figure A-II.2. Normalized ambient-pressure luminescence spectra of bulk and nanocrystalline ZnO samples at ambient pressure at $T = 14$ K. (TES – two electron satellite) (Duzynska, Hrubciak, Drozd et al., 2012)

The results of XRD measurements of bulk ZnO sample in neon as a pressure transmitting medium for pressure between 5.53 and 17.98 GPa are presented in Figure A-II.3. The data shows that the crystal undergoes a pressure-induced phase transition at a pressure of about 9 GPa from B4 wurtzite phase to B1 rocksalt phase. The pure rocksalt phase is observed above pressure of 13.8 GPa. Both phases exist between 9 and 13.8 GPa. At the phase transition the volume per formula unit (p.f.u.) undergoes a large

collapse, from around 22.4 \AA^3 down to 18.6 \AA^3 . The dependence of the volume per formula unit as a function of pressure is shown in Figure A-II.4 for bulk ZnO and ZnO nanocrystals. Two series of measurements were conducted for bulk ZnO crystals with neon and silicon oil as PTM. Both series of measurements yielded very similar results and they are treated together in further analysis.

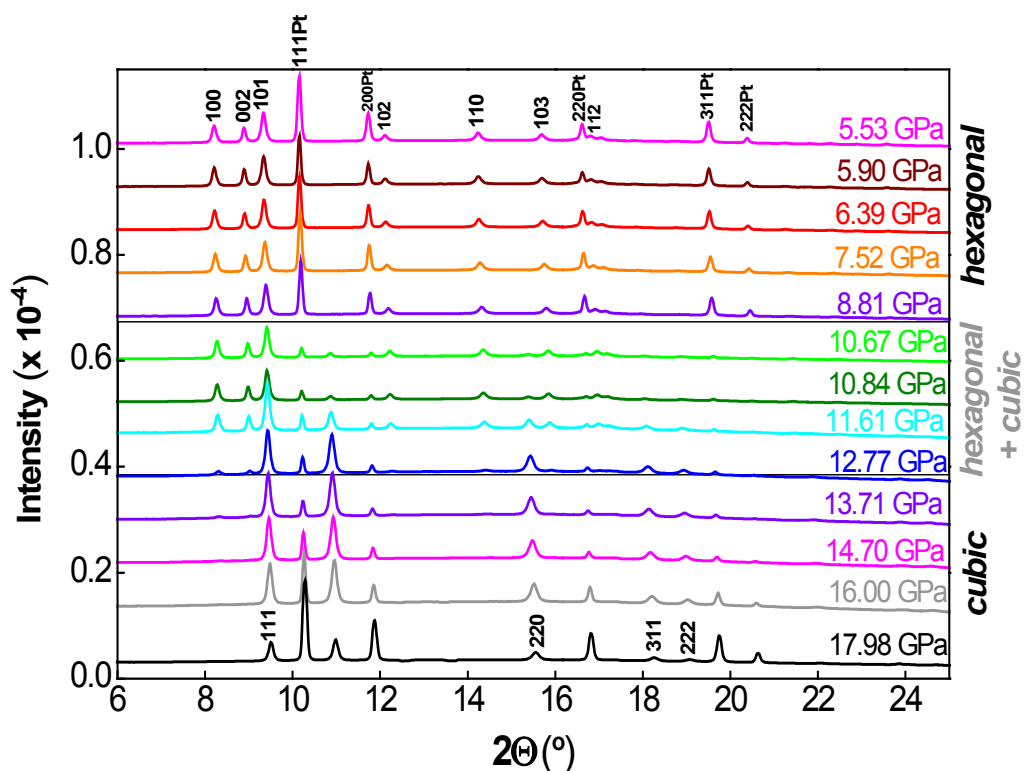


Figure A-II.3. X-Ray diffraction spectra for ZnO bulk crystal as a function of pressure at room temperature with neon as pressure-transmitting medium. Dashed area shows coexistence of wurtzite (hexagonal) and rocksalt (cubic) phases. (Duzynska, Hrubiak, Drozd et al., 2012)

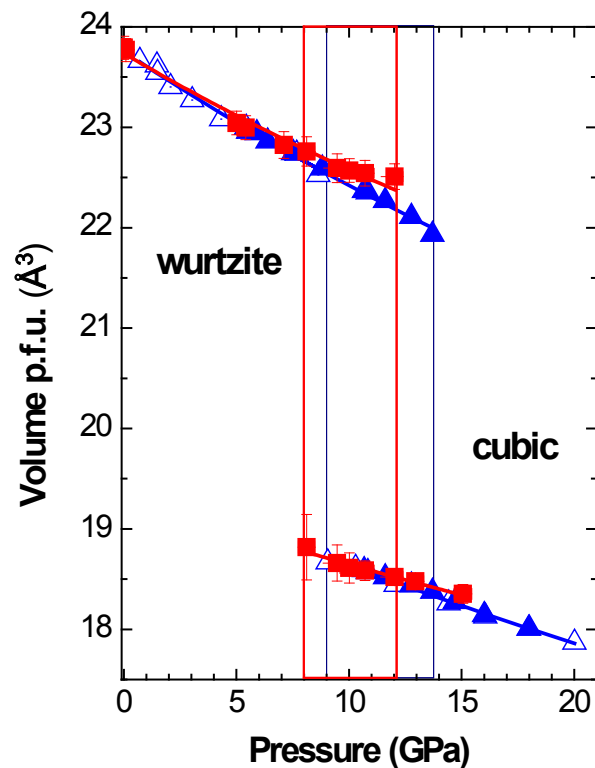


Figure A-II.4. The pressure dependence of the volume per formula unit for bulk and nanocrystalline ZnO. Triangles (blue on line) – bulk ZnO sample. Open symbol: data taken with silicon oil as a pressure transmitting medium (PTM), solid symbols: with neon as a PTM. Squares (red on line) - ZnO nanopowder. The shaded areas are the pressure ranges for which both phases coexist. These ranges are different for bulk and nanocrystalline samples, for nanocrystalline ZnO this range is shifted to lower pressures. Lines: fits of Birch-Murnaghan equation of state. (Duzynska, Hrubciak, Drozd et al., 2012)

The solid lines in Figure A-II.4 are the fits of Birch-Murnaghan (Murnaghan, 1944) equation of state to the data for both wurtzite and cubic phases. The fits yield values of bulk moduli and their pressure derivatives, listed in Table A-II.1.

Table A-II.1. Bulk moduli, their pressure derivatives and volumes per formula unit for bulk and nanopowder ZnO at room temperature.

	Wurtzite phase		Rocksalt phase	
	ZnO crystal	ZnO nano-powder	ZnO crystal	ZnO nano-powder
Bulk modulus B_0 (GPa)	156±13	178±10	180±59	254±27
Pressure derivative of bulk modulus B_0'	3.3±1.9	4.5 (fixed)	3.5±4.1	4 (fixed)
Volume per formula unit (\AA^3)	23.76±0.03	23.74±0.05	19.6±0.2	19.34±0.08

Obtained values of bulk moduli for low-and high pressure phases of ZnO bulk samples are in the middle of results reported up to now [between 135 GPa and 183 GPa, according to literature (Liu et al., 2005; Karzel et al., 1996), for B4 phase, and between 132 GPa (Recio et al., 1998) and 228 GPa (Karzel et al., 1996) for B1 phase]. Taking into account very good quality of our bulk ZnO crystal we consider that obtained results are the most reliable. The defects in crystals (both intrinsic and extrinsic) may change the structural stability of the crystals, changing the pressure range, at which the phase transition occurs, as it was observed in the case of LiNbO₃ crystals with different stoichiometry (Suchocki et al., 2006). Obtained values of bulk modulus of wurtzite phase of bulk crystals are in very good agreement with theoretical calculations, presented in by Jaffe et al. (1993). The measured bulk modulus for rocksalt phase agrees very well with theoretical estimations of Liu et al. (Liu et al., 2005), however relatively large error bars resulted from small number of experimental points encompass several other theoretical estimations (Jaffe and Hess, 1993; Gerward and Olsen, 1995; Karzel et al., 1996; Ahuja

et al., 1998; Recio et al., 1998; Desgreniers, 1998; Decremps et al., 2000, 2003; Jaffe et al., 2000; Mori et al., 2004).

Different results are obtained for nano-powdered ZnO samples. They appear to be considerably less compressible than bulk crystals for both low- and high-pressure phases, as it can be seen from Table A-II.1. Other types of ZnO nanoparticles such as nanowires and nanobelts exhibit similar behavior. Also the phase transition region is different for the nano-crystals and extends from 8 to 12 GPa. For small nanocrystals such result could be associated with surface effects, i.e. influence of surface tension of the nanopowdered samples (Tolbert and Alivisatos, 1993). Surface tension decreases the pressure at which phase transition occurs, and also increases bulk moduli of both phases. However the average size of nanocrystals in our sample (65 nm) cannot explain such behavior unless the actual size of the nanoparticles is much smaller than that observed by SEM, i.e. large complexes of much smaller nanocrystals are observed in SEM (Baran et al., 2012). Relatively large amount of defects present in our nanocrystalline samples may be another source of this effect.

Special attention has been paid to the analysis of the phase transition region in order to search for the postulated intermediate phase. However, careful Rietveld analysis of that pressure region did not reveal any signature of any additional phases in both types of ZnO samples studied.

The phase transitions profoundly modify photo-luminescence (PL) properties of ZnO samples. Figure A-II.5 presents results of high-pressure photo-luminescence measurements of both types of the samples at $T = 10$ K. For bulk sample (Figure A-II.5) relatively sharp luminescence in the region of band-gap energies is observed up to about

9 GPa. Above that pressure the luminescence became very broad, and finally completely disappears for pressure above 12 GPa. This very well agrees with the XRD results, apparently above 12 GPa amount of wurtzite phase is very small and it is not detected in the luminescence.

A different behavior is observed for the nanocrystalline sample, presented in Figure A-II.5b. A relatively sharp luminescence is observed only up to pressure of about 6 GPa. For higher pressures the sharp luminescence structure becomes gradually much broader. Also two components peaks of different luminescence intensity can be observed in the spectra: one with lower energy and intensity at low pressures (at energy of about 3.26 eV at pressure of 1.1 GPa), and the second one with higher energy and higher intensity at low pressure (at energy of about 3.29 eV at pressure of 1.1 GPa). Above pressure of 8 GPa the sharp structure is replaced by a broad band in the region of the band-gap. This change is also accompanied by a strong decrease of the luminescence efficiency under 325 nm excitation.

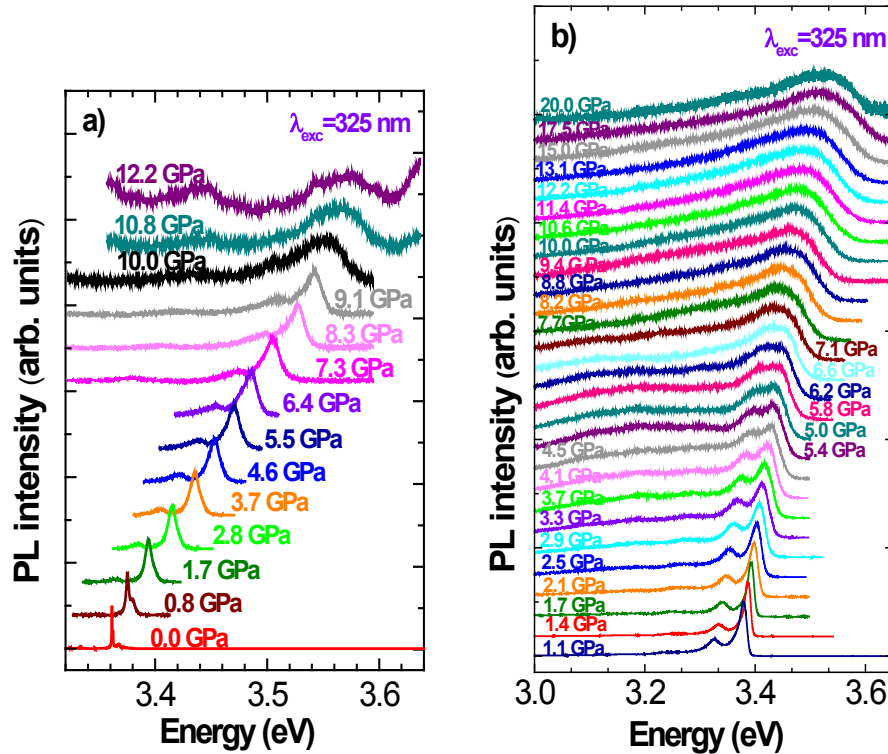


Figure A-II.5. Normalized PL spectra as a function of pressure at $T = 11$ K of (a) bulk ZnO crystal, (b) ZnO nanocrystalline sample (Duzynska, Hrubciak, Drozd et al., 2012)

The positions of the maxima of the luminescence as a function of pressure for both samples are shown in Figure A-II.6. The bulk sample luminescence maximum shifts with pressure linearly with pressure coefficient equal to about 19.9 meV/GPa. The nanocrystalline sample exhibits a different behavior: at low pressure up to about 3 GPa luminescence peak shifts linearly with a pressure coefficient being the same as for the bulk sample. At higher pressures the luminescence peak increases its energy non-linearly and with a much slower rate than in the bulk sample. There is also an apparent kink in this dependence, at pressure of 8 GPa, at which XRD data show appearance of rock-salt phase for this sample. Possibly, this is an effect of the relative changes of the luminescence intensity in two major peaks observed in the nanocrystalline sample. With

increase of pressure, the lower energy peak become dominating over the higher energy luminescence peak, having higher intensity at low pressures.

It remains unclear, why it is possible to observe luminescence above the phase transition pressure in the nanocrystalline sample. The high-pressure B1 phase of ZnO is supposed to have indirect band-gap. Therefore the luminescence should be quenched, as it is observed in the bulk sample. Contrary to that it is observed in the nanocrystalline sample, up to about at least 20 GPa. Similar result was observed earlier in ZnO nanosheets (Chen et al., 2005).

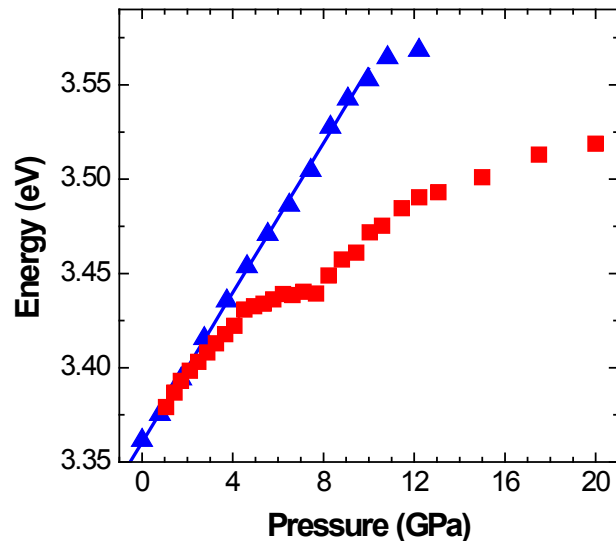


Figure A-II.6. Pressure dependencies of the position of the maxima of PL for bulk (triangles) and nanocrystalline (squares) ZnO samples at $T = 11$ K. (Duzynska, Hrubciak, Drozd et al., 2012)

Summary and conclusions

Lack of reliable values of bulk modulus of ZnO was the motivation for measurements of the elastic properties of this compound using very good quality ZnO crystals. A subsequent goal of this paper was to compare the compressibility of very good

quality bulk ZnO with the compressibility of ZnO nano-crystals. The values of bulk moduli for wurtzite (hexagonal) and rocksalt (cubic) phases, established in this work, are equal to (156 ± 13) and (187 ± 20) GPa, respectively. These values are considerably larger for ZnO nano-crystals. These results show the influence of grain size and crystal quality of the nanocrystalline samples of ZnO on their elastic properties. The phase transition from wurtzite to cubic phase is observed in the pressure region between 9.5 and 13.8 GPa for bulk crystals and at slightly lower pressures for nanocrystalline ZnO. Contrary to theoretical expectations (Boufelfel and Leoni, 2008) no additional intermediate phase of ZnO was detected, neither for bulk nor for nanocrystalline samples.

The phase transition quenches the near-band-gap luminescence of ZnO in bulk crystals. In ZnO nano crystals, occurrence of the phase transition strongly broadens the near-band-gap luminescence and decreases its efficiency. In addition, the pressure coefficient of the luminescence maximum in nanocrystalline ZnO considerably deviates from the linear dependence observed for bulk ZnO.

APPENDIX III: Supplementary materials.

Tables of thermophysical properties of several metals

Table A-III.1. Tables of thermophysical properties: Group IVB transition metals

Table	Element	Phase	Pressure / bar	Page
1.1	Ti	α	1	162
1.2	Ti	α	100,000	163
1.3	Ti	ω	1	164
1.4	Ti	ω	800,000	165
1.5	Ti	β	1	166
1.6	Ti	β	500,000	167
2.1	Zr	α	1	168
2.2	Zr	α	600,000	169
2.3	Zr	ω	1	170
2.4	Zr	ω	600,000	171
2.5	Zr	β	1	172
2.6	Zr	β	600,000	173
3.1	Hf	α	1	174
3.2	Hf	α	600,000	175
3.3	Hf	ω	1	176
3.4	Hf	ω	600,000	177
3.5	Hf	β	1	178
3.6	Hf	β	600,000	179

Table 1.1

Phase: Ti solid α

Atomic weight 47.867

Pressure: 1 bar

T (K)	C_P (J/mol K)	H (kJ/mol)	S (J/mol K)	G (kJ/mol)	V (cm ³ /mol)	B (GPa)	C_V (kJ/mol K)	γ
300	23.96	0.05	37.24	-9.23	9.828	108.35	23.94	0.93
400	23.96	2.65	37.24	-12.71	9.828	107.80	23.94	0.94
500	23.96	5.40	37.24	-16.86	9.828	107.15	23.94	0.95
600	23.96	8.23	37.24	-21.58	9.828	106.39	23.94	0.97
700	23.96	11.11	37.24	-26.78	9.828	105.53	23.94	1.00
800	23.96	14.03	37.24	-32.39	9.828	104.60	23.94	1.01
900	23.96	17.03	37.24	-38.37	9.828	103.59	23.94	1.01
1000	23.96	20.15	37.24	-44.69	9.828	102.51	23.94	0.99
1100	23.96	23.47	37.24	-51.33	9.828	101.34	23.94	0.96
1166	23.96	25.79	37.24	-55.89	9.828	100.53	23.94	0.93
1166	23.96	25.79	37.24	-55.89	9.828	100.52	23.94	1.16
1200	23.96	26.79	37.24	-58.28	9.828	100.09	23.94	1.15
1300	23.96	29.76	37.24	-65.49	9.828	98.81	23.94	1.14

For EoS parameters refer to Table 1.4 on page 75, for EoS formulation refer to the section on page 9.

Table 1.2

Phase: Ti solid α

Atomic weight 47.867

Pressure: 100,000 bar

T (K)	C_p (J/mol K)	H (kJ/mol)	S (J/mol K)	G (kJ/mol)	V (cm ³ /mol)	B (GPa)	C_v (kJ/mol K)	γ
300	23.96	101.57	37.24	92.88	9.828	141.17	23.94	1.00
400	23.96	104.13	37.24	89.60	9.828	140.77	23.94	1.00
500	23.96	106.83	37.24	85.65	9.828	140.34	23.94	1.01
600	23.96	109.61	37.24	81.16	9.828	139.88	23.94	1.03
700	23.96	112.43	37.24	76.20	9.828	139.40	23.94	1.05
800	23.96	115.29	37.24	70.83	9.828	138.90	23.94	1.07
900	23.96	118.22	37.24	65.09	9.828	138.37	23.94	1.07
1000	23.96	121.26	37.24	59.03	9.828	137.83	23.94	1.05
1100	23.96	124.47	37.24	52.65	9.828	137.26	23.94	1.02
1166	23.96	126.71	37.24	48.28	9.828	136.87	23.94	1.00
1166	23.96	126.71	37.24	48.28	9.828	136.87	23.94	1.22
1200	23.96	127.68	37.24	45.97	9.828	136.66	23.94	1.22
1300	23.96	130.60	37.24	39.05	9.828	136.05	23.94	1.21

For EoS parameters refer to Table 1.4 on page 75, for EoS formulation refer to the section on page 9.

Table 1.3

Phase: Ti solid ω

Atomic weight 47.867

Pressure: 1 bar

T (K)	C_p (J/mol K)	H (kJ/mol)	S (J/mol K)	G (kJ/mol)	V (cm ³ /mol)	B (GPa)	C_v (kJ/mol K)	γ
300	23.96	2.25	37.24	-7.10	9.828	124.22	23.94	1.08
500	23.96	7.60	37.24	-14.78	9.828	123.09	23.94	1.08
700	23.96	13.31	37.24	-24.74	9.828	121.58	23.94	1.12
900	23.96	19.23	37.24	-36.38	9.828	119.76	23.94	1.13
1100	23.96	25.67	37.24	-49.39	9.828	117.64	23.94	1.06
1166	23.96	27.99	37.24	-53.96	9.828	116.86	23.94	1.03
1166	23.96	27.99	37.24	-53.96	9.828	116.86	23.94	1.28
1300	23.96	31.96	37.24	-63.60	9.828	115.22	23.94	1.27
1500	23.96	38.10	37.24	-78.75	9.828	112.71	23.94	1.24
1700	23.96	44.47	37.24	-94.73	9.828	110.12	23.94	1.22
1900	23.96	51.09	37.24	-111.48	9.828	107.48	23.94	1.20
1939	23.96	52.41	37.24	-114.83	9.828	106.96	23.94	1.20
1939	23.96	52.41	37.24	-114.83	9.828	106.96	23.94	1.20
2100	23.96	57.88	37.24	-128.94	9.828	104.80	23.94	1.21
2300	23.96	64.68	37.24	-147.05	9.828	102.10	23.94	1.23
2500	23.96	71.48	37.24	-165.75	9.828	99.42	23.94	1.25
2700	23.96	78.28	37.24	-184.99	9.828	96.79	23.94	1.26
2800	23.96	81.68	37.24	-194.80	9.828	95.48	23.94	1.26

For EoS parameters refer to Table 1.4 on page 75, for EoS formulation refer to the section on page 9.

Table 1.4

Phase: Ti solid ω

Atomic weight 47.867

Pressure: 800,000 bar

T (K)	C_P (J/mol K)	H (kJ/mol)	S (J/mol K)	G (kJ/mol)	V (cm ³ /mol)	B (GPa)	C_V (kJ/mol K)	γ
300	23.96	658.00	37.24	651.85	9.828	334.36	23.94	1.23
500	23.96	662.91	37.24	646.42	9.828	332.75	23.94	1.23
700	23.96	668.16	37.24	638.89	9.828	331.09	23.94	1.26
900	23.96	673.57	37.24	629.83	9.828	329.38	23.94	1.28
1100	23.96	679.29	37.24	619.52	9.828	327.61	23.94	1.24
1166	23.96	681.28	37.24	615.88	9.828	327.01	23.94	1.22
1166	23.96	681.28	37.24	615.88	9.828	327.01	23.94	1.39
1300	23.96	684.94	37.24	608.16	9.828	325.77	23.94	1.39
1500	23.96	690.51	37.24	595.94	9.828	323.92	23.94	1.39
1700	23.96	696.22	37.24	582.97	9.828	322.04	23.94	1.39
1900	23.96	702.06	37.24	569.32	9.828	320.14	23.94	1.39
1939	23.96	703.21	37.24	566.58	9.828	319.76	23.94	1.39
1939	23.96	703.21	37.24	566.58	9.828	319.76	23.94	1.39
2100	23.96	707.99	37.24	555.04	9.828	318.21	23.94	1.42
2300	23.96	713.93	37.24	540.20	9.828	316.28	23.94	1.45
2500	23.96	719.87	37.24	524.84	9.828	314.33	23.94	1.48
2700	23.96	725.82	37.24	509.01	9.828	312.38	23.94	1.51
2800	23.96	728.79	37.24	500.92	9.828	311.40	23.94	1.52

For EoS parameters refer to Table 1.4 on page 75, for EoS formulation refer to the section on page 9.

Table 1.5

Phase: Ti solid β

Atomic weight 47.867

Pressure: 1 bar

T (K)	C_P (J/mol K)	H (kJ/mol)	S (J/mol K)	G (kJ/mol)	V (cm ³ /mol)	B (GPa)	C_V (kJ/mol K)	γ
800	23.96	19.66	37.24	-30.78	9.828	137.14	23.94	0.71
900	23.96	22.40	37.24	-37.25	9.828	135.94	23.94	0.71
1000	23.96	25.19	37.24	-44.02	9.828	134.70	23.94	0.71
1100	23.96	28.04	37.24	-51.08	9.828	133.41	23.94	0.72
1200	23.96	30.96	37.24	-58.40	9.828	132.07	23.94	0.72
1300	23.96	33.94	37.24	-65.97	9.828	130.69	23.94	0.72
1400	23.96	37.00	37.24	-73.77	9.828	129.26	23.94	0.72
1500	23.96	40.15	37.24	-81.79	9.828	127.78	23.94	0.72
1600	23.96	43.40	37.24	-90.03	9.828	126.24	23.94	0.72
1700	23.96	46.78	37.24	-98.47	9.828	124.66	23.94	0.71
1800	23.96	50.28	37.24	-107.11	9.828	123.03	23.94	0.71
1900	23.96	53.93	37.24	-115.96	9.828	121.34	23.94	0.70
1939	23.96	55.39	37.24	-119.46	9.828	120.66	23.94	0.70
1939	23.96	55.39	37.24	-119.46	9.828	120.67	23.94	0.70
2000	23.96	57.73	37.24	-124.99	9.828	119.59	23.94	0.69
2100	23.96	61.71	37.24	-134.23	9.828	117.80	23.94	0.69
2200	23.96	65.86	37.24	-143.65	9.828	115.95	23.94	0.68
2300	23.96	70.22	37.24	-153.28	9.828	114.04	23.94	0.67

For EoS parameters refer to Table 1.4 on page 75, for EoS formulation refer to the section on page 9.

Table 1.6

Phase: Ti solid β

Atomic weight 47.867

Pressure: 500,000 bar

T (K)	C_P (J/mol K)	H (kJ/mol)	S (J/mol K)	G (kJ/mol)	V (cm ³ /mol)	B (GPa)	C_V (kJ/mol K)	γ
800	23.96	476.12	37.24	428.42	9.828	384.13	23.94	0.55
900	23.96	478.75	37.24	422.30	9.828	383.21	23.94	0.56
1000	23.96	481.42	37.24	415.88	9.828	382.26	23.94	0.57
1100	23.96	484.13	37.24	409.20	9.828	381.29	23.94	0.59
1166	23.96	485.95	37.24	404.65	9.828	380.64	23.94	0.60
1166	23.96	485.95	37.24	404.65	9.828	380.64	23.94	0.60
1200	23.96	486.89	37.24	402.26	9.828	380.30	23.94	0.60
1300	23.96	489.68	37.24	395.10	9.828	379.28	23.94	0.62
1400	23.96	492.53	37.24	387.72	9.828	378.23	23.94	0.63
1500	23.96	495.43	37.24	380.13	9.828	377.16	23.94	0.64
1600	23.96	498.40	37.24	372.35	9.828	376.05	23.94	0.65
1700	23.96	501.44	37.24	364.38	9.828	374.91	23.94	0.67
1800	23.96	504.57	37.24	356.22	9.828	373.74	23.94	0.68
1900	23.96	507.79	37.24	347.90	9.828	372.52	23.94	0.69
1939	23.96	509.07	37.24	344.60	9.828	372.04	23.94	0.70
1939	23.96	509.07	37.24	344.60	9.828	372.04	23.94	0.70
2000	23.96	511.11	37.24	339.39	9.828	371.27	23.94	0.70
2100	23.96	514.53	37.24	330.73	9.828	369.97	23.94	0.72
2200	23.96	518.07	37.24	321.89	9.828	368.63	23.94	0.73
2300	23.96	521.74	37.24	312.89	9.828	367.24	23.94	0.74

For EoS parameters refer to Table 1.4 on page 75, for EoS formulation refer to the section on page 9.

Table 2.1

Phase: Zr solid α

Atomic weight 91.224

Pressure: 1 bar

T (K)	C_P (J/mol K)	H (kJ/mol)	S (J/mol K)	G (kJ/mol)	V (cm ³ /mol)	B (GPa)	C_V (kJ/mol K)	γ
300	23.96	0.05	37.24	-11.66	9.828	88.52	23.94	0.70
400	23.96	2.61	37.24	-15.95	9.828	88.20	23.94	0.72
500	23.96	5.23	37.24	-20.89	9.828	87.84	23.94	0.73
600	23.96	7.92	37.24	-26.36	9.828	87.44	23.94	0.74
700	23.96	10.69	37.24	-32.29	9.828	87.01	23.94	0.74
800	23.96	13.54	37.24	-38.63	9.828	86.54	23.94	0.75
900	23.96	16.49	37.24	-45.32	9.828	86.03	23.94	0.75
1000	23.96	19.54	37.24	-52.35	9.828	85.48	23.94	0.75
1100	23.96	22.71	37.24	-59.70	9.828	84.88	23.94	0.74
1200	23.96	25.98	37.24	-67.33	9.828	84.23	23.94	0.76
1300	23.96	29.25	37.24	-75.24	9.828	83.54	23.94	0.79
1400	23.96	32.53	37.24	-83.40	9.828	82.82	23.94	0.81
1500	23.96	35.81	37.24	-91.80	9.828	82.07	23.94	0.83
1600	23.96	39.08	37.24	-100.41	9.828	81.29	23.94	0.84
1700	23.96	42.36	37.24	-109.23	9.828	80.49	23.94	0.86
1800	23.96	45.63	37.24	-118.24	9.828	79.68	23.94	0.87
1900	23.96	48.91	37.24	-127.43	9.828	78.85	23.94	0.88
2000	23.96	52.18	37.24	-136.80	9.828	78.02	23.94	0.90
2100	23.96	55.46	37.24	-146.33	9.828	77.18	23.94	0.91
2200	23.96	58.73	37.24	-156.02	9.828	76.34	23.94	0.91
2300	23.96	62.01	37.24	-165.85	9.828	75.50	23.94	0.92

For EoS parameters refer to Table 1.4 on page 75, for EoS formulation refer to the section on page 9.

Table 2.2

Phase: Zr solid α

Atomic weight 91.224

Pressure: 600,000 bar

T (K)	C_P (J/mol K)	H (kJ/mol)	S (J/mol K)	G (kJ/mol)	V (cm ³ /mol)	B (GPa)	C_V (kJ/mol K)	γ
300	23.96	0.05	37.24	-11.70	9.828	88.50	23.94	0.70
400	23.96	2.61	37.24	-15.90	9.828	88.20	23.94	0.72
500	23.96	5.23	37.24	-20.90	9.828	87.80	23.94	0.73
600	23.96	7.92	37.24	-26.40	9.828	87.40	23.94	0.74
700	23.96	10.70	37.24	-32.30	9.828	87.00	23.94	0.74
800	23.96	13.50	37.24	-38.60	9.828	86.50	23.94	0.75
900	23.96	16.50	37.24	-45.30	9.828	86.00	23.94	0.75
1000	23.96	19.50	37.24	-52.40	9.828	85.50	23.94	0.75
1100	23.96	22.70	37.24	-59.70	9.828	84.90	23.94	0.74
1200	23.96	26.00	37.24	-67.30	9.828	84.20	23.94	0.76
1300	23.96	29.30	37.24	-75.20	9.828	83.50	23.94	0.79
1400	23.96	32.50	37.24	-83.40	9.828	82.80	23.94	0.81
1500	23.96	35.80	37.24	-91.80	9.828	82.10	23.94	0.83
1600	23.96	39.10	37.24	-100.00	9.828	81.30	23.94	0.84
1700	23.96	42.40	37.24	-109.00	9.828	80.50	23.94	0.86
1800	23.96	45.60	37.24	-118.00	9.828	79.70	23.94	0.87
1900	23.96	48.90	37.24	-127.00	9.828	78.90	23.94	0.89
2000	23.96	52.20	37.24	-137.00	9.828	78.00	23.94	0.90
2100	23.96	55.50	37.24	-146.00	9.828	77.20	23.94	0.91
2200	23.96	58.70	37.24	-156.00	9.828	76.30	23.94	0.91
2300	23.96	62.00	37.24	-166.00	9.828	75.50	23.94	0.92

For EoS parameters refer to Table 1.4 on page 75, for EoS formulation refer to the section on page 9.

Table 2.3

Phase: Zr solid ω

Atomic weight 91.224

Pressure: 1 bar

T (K)	C_p (J/mol K)	H (kJ/mol)	S (J/mol K)	G (kJ/mol)	V (cm ³ /mol)	B (GPa)	C_v (kJ/mol K)	γ
300	23.96	1.01	37.24	-10.82	9.828	90.97	23.94	1.18
400	23.96	3.56	37.24	-15.15	9.828	90.04	23.94	1.20
500	23.96	6.19	37.24	-20.13	9.828	89.07	23.94	1.21
600	23.96	8.88	37.24	-25.64	9.828	88.07	23.94	1.20
700	23.96	11.65	37.24	-31.62	9.828	87.03	23.94	1.19
800	23.96	14.50	37.24	-37.99	9.828	85.96	23.94	1.18
900	23.96	17.45	37.24	-44.73	9.828	84.86	23.94	1.16
1000	23.96	20.50	37.24	-51.80	9.828	83.72	23.94	1.14
1100	23.96	23.67	37.24	-59.18	9.828	82.55	23.94	1.13
1200	23.96	26.94	37.24	-66.85	9.828	81.34	23.94	1.13
1300	23.96	30.21	37.24	-74.80	9.828	80.10	23.94	1.16
1400	23.96	33.49	37.24	-83.00	9.828	78.84	23.94	1.17
1500	23.96	36.76	37.24	-91.44	9.828	77.58	23.94	1.19
1600	23.96	40.04	37.24	-100.09	9.828	76.31	23.94	1.20
1700	23.96	43.31	37.24	-108.95	9.828	75.04	23.94	1.21
1800	23.96	46.59	37.24	-118.00	9.828	73.79	23.94	1.22
1900	23.96	49.86	37.24	-127.24	9.828	72.54	23.94	1.23
2000	23.96	53.14	37.24	-136.64	9.828	71.32	23.94	1.23
2100	23.96	56.42	37.24	-146.21	9.828	70.11	23.94	1.24
2200	23.96	59.69	37.24	-155.94	9.828	68.92	23.94	1.24
2300	23.96	62.97	37.24	-165.81	9.828	67.75	23.94	1.24

For EoS parameters refer to Table 1.4 on page 75, for EoS formulation refer to the section on page 9.

Table 2.4

Phase: Zr solid ω

Atomic weight 91.224

Pressure: 600,000 bar

T (K)	C_p (J/mol K)	H (kJ/mol)	S (J/mol K)	G (kJ/mol)	V (cm ³ /mol)	B (GPa)	C_v (kJ/mol K)	γ
300	23.96	671.09	37.24	661.76	9.828	269.30	23.94	0.75
400	23.96	673.48	37.24	658.30	9.828	268.67	23.94	0.77
500	23.96	675.95	37.24	654.22	9.828	268.02	23.94	0.78
600	23.96	678.48	37.24	649.63	9.828	267.35	23.94	0.79
700	23.96	681.07	37.24	644.62	9.828	266.66	23.94	0.80
800	23.96	683.71	37.24	639.23	9.828	265.97	23.94	0.81
900	23.96	686.40	37.24	633.51	9.828	265.26	23.94	0.82
1000	23.96	689.16	37.24	627.49	9.828	264.53	23.94	0.82
1100	23.96	691.97	37.24	621.19	9.828	263.79	23.94	0.83
1200	23.96	694.84	37.24	614.63	9.828	263.03	23.94	0.85
1300	23.96	697.71	37.24	607.82	9.828	262.25	23.94	0.88
1400	23.96	700.59	37.24	600.80	9.828	261.47	23.94	0.90
1500	23.96	703.47	37.24	593.57	9.828	260.67	23.94	0.92
1600	23.96	706.34	37.24	586.15	9.828	259.86	23.94	0.94
1700	23.96	709.22	37.24	578.55	9.828	259.04	23.94	0.96
1800	23.96	712.10	37.24	570.78	9.828	258.21	23.94	0.97
1900	23.96	714.98	37.24	562.85	9.828	257.38	23.94	0.99
2000	23.96	717.86	37.24	554.77	9.828	256.54	23.94	1.00
2100	23.96	720.74	37.24	546.55	9.828	255.70	23.94	1.02
2200	23.96	723.63	37.24	538.18	9.828	254.85	23.94	1.03
2300	23.96	726.51	37.24	529.69	9.828	254.00	23.94	1.04

For EoS parameters refer to Table 1.4 on page 75, for EoS formulation refer to the section on page 9.

Table 2.5

Phase: Zr solid β

Atomic weight 91.224

Pressure: 1 bar

T (K)	C_P (J/mol K)	H (kJ/mol)	S (J/mol K)	G (kJ/mol)	V (cm ³ /mol)	B (GPa)	C_V (kJ/mol K)	γ
300	23.96	4.86	37.24	-8.14	9.828	84.72	23.94	0.78
400	23.96	7.42	37.24	-12.86	9.828	84.31	23.94	0.80
500	23.96	10.05	37.24	-18.24	9.828	83.84	23.94	0.81
600	23.96	12.74	37.24	-24.14	9.828	83.34	23.94	0.82
700	23.96	15.50	37.24	-30.51	9.828	82.79	23.94	0.82
800	23.96	18.35	37.24	-37.28	9.828	82.19	23.94	0.83
800	23.96	18.35	37.24	-37.28	9.828	82.20	23.94	0.83
900	23.96	21.22	37.24	-44.40	9.828	81.56	23.94	0.86
1000	23.96	24.05	37.24	-51.84	9.828	80.89	23.94	0.89
1100	23.96	26.88	37.24	-59.57	9.828	80.19	23.94	0.90
1200	23.96	29.71	37.24	-67.55	9.828	79.48	23.94	0.91
1300	23.96	32.58	37.24	-75.78	9.828	78.76	23.94	0.91
1400	23.96	35.49	37.24	-84.22	9.828	78.02	23.94	0.90
1500	23.96	38.45	37.24	-92.87	9.828	77.26	23.94	0.90
1600	23.96	41.48	37.24	-101.73	9.828	76.49	23.94	0.89
1700	23.96	44.58	37.24	-110.77	9.828	75.71	23.94	0.88
1800	23.96	47.76	37.24	-120.00	9.828	74.91	23.94	0.86
1900	23.96	51.05	37.24	-129.41	9.828	74.10	23.94	0.85
2000	23.96	54.44	37.24	-139.00	9.828	73.27	23.94	0.84
2100	23.96	57.94	37.24	-148.75	9.828	72.42	23.94	0.82
2200	23.96	61.57	37.24	-158.68	9.828	71.55	23.94	0.81
2300	23.96	65.34	37.24	-168.78	9.828	70.67	23.94	0.79
2400	23.96	69.25	37.24	-179.04	9.828	69.76	23.94	0.77
2500	23.96	73.33	37.24	-189.47	9.828	68.84	23.94	0.76

For EoS parameters refer to Table 1.4 on page 75, for EoS formulation refer to the section on page 9.

Table 2.6

Phase: Zr solid β

Atomic weight 91.224

Pressure: 600,000 bar

T (K)	C_P (J/mol K)	H (kJ/mol)	S (J/mol K)	G (kJ/mol)	V (cm ³ /mol)	B (GPa)	C_V (kJ/mol K)	γ
300	23.96	665.36	37.24	654.53	9.828	228.62	23.94	0.67
400	23.96	667.76	37.24	650.57	9.828	228.25	23.94	0.68
500	23.96	670.24	37.24	645.98	9.828	227.87	23.94	0.69
600	23.96	672.78	37.24	640.89	9.828	227.48	23.94	0.70
700	23.96	675.37	37.24	635.37	9.828	227.08	23.94	0.71
800	23.96	678.02	37.24	629.48	9.828	226.67	23.94	0.71
800	23.96	678.02	37.24	629.48	9.828	226.67	23.94	0.71
900	23.96	680.68	37.24	623.25	9.828	226.25	23.94	0.74
1000	23.96	683.32	37.24	616.73	9.828	225.82	23.94	0.75
1100	23.96	685.97	37.24	609.94	9.828	225.39	23.94	0.76
1200	23.96	688.63	37.24	602.91	9.828	224.95	23.94	0.77
1300	23.96	691.30	37.24	595.66	9.828	224.51	23.94	0.78
1400	23.96	693.99	37.24	588.21	9.828	224.07	23.94	0.78
1500	23.96	696.71	37.24	580.55	9.828	223.61	23.94	0.78
1600	23.96	699.47	37.24	572.72	9.828	223.16	23.94	0.79
1700	23.96	702.26	37.24	564.71	9.828	222.70	23.94	0.79
1800	23.96	705.10	37.24	556.54	9.828	222.23	23.94	0.79
1900	23.96	707.99	37.24	548.21	9.828	221.76	23.94	0.79
2000	23.96	710.93	37.24	539.72	9.828	221.28	23.94	0.79
2100	23.96	713.92	37.24	531.09	9.828	220.79	23.94	0.79
2200	23.96	716.99	37.24	522.31	9.828	220.30	23.94	0.79
2300	23.96	720.12	37.24	513.39	9.828	219.80	23.94	0.79
2400	23.96	723.32	37.24	504.34	9.828	219.29	23.94	0.78
2500	23.96	726.61	37.24	495.15	9.828	218.76	23.94	0.78

For EoS parameters refer to Table 1.4 on page 75, for EoS formulation refer to the section on page 9.

Table 3.1

Phase: Hf solid α

Atomic weight 178.49

Pressure: 1 bar

T (K)	C_p (J/mol K)	H (kJ/mol)	S (J/mol K)	G (kJ/mol)	V (cm ³ /mol)	B (GPa)	C_v (kJ/mol K)	γ
300	23.96	0.05	37.24	-13.07	9.828	126.37	23.94	1.51
400	23.96	2.67	37.24	-17.83	9.828	123.86	23.94	1.51
500	23.96	5.39	37.24	-23.27	9.828	121.32	23.94	1.50
600	23.96	8.20	37.24	-29.26	9.828	118.77	23.94	1.48
700	23.96	11.11	37.24	-35.74	9.828	116.23	23.94	1.46
800	23.96	14.10	37.24	-42.63	9.828	113.70	23.94	1.44
900	23.96	17.18	37.24	-49.91	9.828	111.19	23.94	1.42
1000	23.96	20.34	37.24	-57.53	9.828	108.69	23.94	1.40
1100	23.96	23.58	37.24	-65.47	9.828	106.23	23.94	1.39
1200	23.96	26.89	37.24	-73.71	9.828	103.79	23.94	1.37
1300	23.96	30.28	37.24	-82.24	9.828	101.40	23.94	1.35
1400	23.96	33.74	37.24	-91.02	9.828	99.04	23.94	1.33
1500	23.96	37.28	37.24	-100.05	9.828	96.73	23.94	1.32
1600	23.96	40.89	37.24	-109.33	9.828	94.46	23.94	1.30
1700	23.96	44.57	37.24	-118.83	9.828	92.25	23.94	1.28
1800	23.96	48.32	37.24	-128.55	9.828	90.08	23.94	1.27
1900	23.96	52.15	37.24	-138.48	9.828	87.96	23.94	1.25
2000	23.96	56.04	37.24	-148.61	9.828	85.90	23.94	1.23
2100	23.96	60.00	37.24	-158.94	9.828	83.89	23.94	1.21

For EoS parameters refer to Table 1.4 on page 75, for EoS formulation refer to the section on page 9.

Table 3.2

Phase: Hf solid α

Atomic weight 178.49

Pressure: 600,000 bar

T (K)	C_p (J/mol K)	H (kJ/mol)	S (J/mol K)	G (kJ/mol)	V (cm ³ /mol)	B (GPa)	C_v (kJ/mol K)	γ
300	23.96	671.65	37.24	660.47	9.828	312.17	23.94	0.58
400	23.96	674.10	37.24	656.38	9.828	311.53	23.94	0.61
500	23.96	676.65	37.24	651.66	9.828	310.85	23.94	0.63
600	23.96	679.28	37.24	646.41	9.828	310.15	23.94	0.65
700	23.96	681.97	37.24	640.72	9.828	309.43	23.94	0.67
800	23.96	684.72	37.24	634.64	9.828	308.68	23.94	0.69
900	23.96	687.52	37.24	628.22	9.828	307.90	23.94	0.71
1000	23.96	690.36	37.24	621.48	9.828	307.10	23.94	0.73
1100	23.96	693.26	37.24	614.45	9.828	306.28	23.94	0.75
1200	23.96	696.19	37.24	607.15	9.828	305.44	23.94	0.77
1300	23.96	699.17	37.24	599.61	9.828	304.58	23.94	0.79
1400	23.96	702.20	37.24	591.84	9.828	303.69	23.94	0.81
1500	23.96	705.26	37.24	583.85	9.828	302.79	23.94	0.83
1600	23.96	708.37	37.24	575.66	9.828	301.86	23.94	0.84
1700	23.96	711.51	37.24	567.26	9.828	300.92	23.94	0.86
1800	23.96	714.70	37.24	558.69	9.828	299.96	23.94	0.88
1900	23.96	717.93	37.24	549.93	9.828	298.98	23.94	0.90
2000	23.96	721.19	37.24	541.01	9.828	297.98	23.94	0.91
2100	23.96	724.50	37.24	531.92	9.828	296.97	23.94	0.93
2200	23.96	727.84	37.24	522.67	9.828	295.94	23.94	0.94
2300	23.96	731.22	37.24	513.27	9.828	294.89	23.94	0.96
2400	23.96	734.64	37.24	503.72	9.828	293.83	23.94	0.97
2500	23.96	738.10	37.24	494.02	9.828	292.76	23.94	0.99

For EoS parameters refer to Table 1.4 on page 75, for EoS formulation refer to the section on page 9.

Table 3.3

Phase: Hf solid ω

Atomic weight 178.49

Pressure: 1 bar

T (K)	C_P (J/mol K)	H (kJ/mol)	S (J/mol K)	G (kJ/mol)	V (cm ³ /mol)	B (GPa)	C_V (kJ/mol K)	γ
300	23.96	4.36	37.24	-9.25	9.828	96.09	23.94	0.87
400	23.96	6.92	37.24	-14.17	9.828	95.60	23.94	0.90
500	23.96	9.55	37.24	-19.74	9.828	95.06	23.94	0.90
600	23.96	12.24	37.24	-25.85	9.828	94.49	23.94	0.91
700	23.96	15.01	37.24	-32.41	9.828	93.89	23.94	0.90
800	23.96	17.86	37.24	-39.38	9.828	93.25	23.94	0.90
900	23.96	20.81	37.24	-46.71	9.828	92.57	23.94	0.90
1000	23.96	23.86	37.24	-54.38	9.828	91.84	23.94	0.89
1100	23.96	27.03	37.24	-62.35	9.828	91.08	23.94	0.88
1200	23.96	30.29	37.24	-70.62	9.828	90.27	23.94	0.89
1300	23.96	33.57	37.24	-79.17	9.828	89.42	23.94	0.92
1400	23.96	36.85	37.24	-87.96	9.828	88.55	23.94	0.94
1500	23.96	40.12	37.24	-96.99	9.828	87.64	23.94	0.96
1600	23.96	43.40	37.24	-106.24	9.828	86.72	23.94	0.97
1700	23.96	46.67	37.24	-115.69	9.828	85.78	23.94	0.99
1800	23.96	49.95	37.24	-125.33	9.828	84.83	23.94	1.00
1900	23.96	53.22	37.24	-135.16	9.828	83.87	23.94	1.01
2000	23.96	56.50	37.24	-145.16	9.828	82.91	23.94	1.02
2100	23.96	59.77	37.24	-155.32	9.828	81.95	23.94	1.03
2200	23.96	63.05	37.24	-165.64	9.828	80.99	23.94	1.03
2300	23.96	66.33	37.24	-176.11	9.828	80.03	23.94	1.04

For EoS parameters refer to Table 1.4 on page 75, for EoS formulation refer to the section on page 9.

Table 3.4

Phase: Hf solid ω

Atomic weight 178.49

Pressure: 600,000 bar

T (K)	C_P (J/mol K)	H (kJ/mol)	S (J/mol K)	G (kJ/mol)	V (cm ³ /mol)	B (GPa)	C_V (kJ/mol K)	γ
300	23.96	669.14	37.24	657.67	9.828	294.22	23.94	0.83
400	23.96	671.54	37.24	653.49	9.828	293.59	23.94	0.85
500	23.96	674.04	37.24	648.68	9.828	292.94	23.94	0.86
600	23.96	676.59	37.24	643.37	9.828	292.27	23.94	0.86
700	23.96	679.20	37.24	637.63	9.828	291.59	23.94	0.87
800	23.96	681.87	37.24	631.51	9.828	290.90	23.94	0.88
900	23.96	684.60	37.24	625.05	9.828	290.19	23.94	0.88
1000	23.96	687.39	37.24	618.29	9.828	289.47	23.94	0.89
1100	23.96	690.25	37.24	611.24	9.828	288.73	23.94	0.90
1200	23.96	693.17	37.24	603.93	9.828	287.98	23.94	0.92
1300	23.96	696.09	37.24	596.37	9.828	287.21	23.94	0.94
1400	23.96	699.01	37.24	588.59	9.828	286.43	23.94	0.96
1500	23.96	701.94	37.24	580.60	9.828	285.63	23.94	0.99
1600	23.96	704.86	37.24	572.42	9.828	284.82	23.94	1.01
1700	23.96	707.79	37.24	564.05	9.828	284.01	23.94	1.02
1800	23.96	710.72	37.24	555.51	9.828	283.18	23.94	1.04
1900	23.96	713.65	37.24	546.81	9.828	282.35	23.94	1.06
2000	23.96	716.57	37.24	537.95	9.828	281.52	23.94	1.07
2100	23.96	719.50	37.24	528.95	9.828	280.67	23.94	1.09
2200	23.96	722.43	37.24	519.81	9.828	279.83	23.94	1.10
2300	23.96	725.36	37.24	510.53	9.828	278.98	23.94	1.12

For EoS parameters refer to Table 1.4 on page 75, for EoS formulation refer to the section on page 9.

Table 3.5

Phase: Hf solid β

Atomic weight 178.49

Pressure: 1 bar

T (K)	C_P (J/mol K)	H (kJ/mol)	S (J/mol K)	G (kJ/mol)	V (cm ³ /mol)	B (GPa)	C_V (kJ/mol K)	γ
300	23.96	18.72	37.24	0.35	9.828	91.21	23.94	1.55
400	23.96	20.54	37.24	-6.04	9.828	90.64	23.94	1.37
500	23.96	22.46	37.24	-12.90	9.828	90.23	23.94	1.22
600	23.96	24.46	37.24	-20.16	9.828	89.93	23.94	1.11
700	23.96	26.56	37.24	-27.77	9.828	89.71	23.94	1.02
800	23.96	28.75	37.24	-35.67	9.828	89.54	23.94	0.96
900	23.96	31.04	37.24	-43.86	9.828	89.41	23.94	0.90
1000	23.96	33.42	37.24	-52.31	9.828	89.29	23.94	0.86
1100	23.96	35.88	37.24	-61.01	9.828	89.19	23.94	0.83
1200	23.96	38.45	37.24	-69.93	9.828	89.08	23.94	0.81
1300	23.96	41.10	37.24	-79.06	9.828	88.96	23.94	0.79
1400	23.96	43.85	37.24	-88.41	9.828	88.82	23.94	0.77
1500	23.96	46.68	37.24	-97.95	9.828	88.65	23.94	0.76
1600	23.96	49.61	37.24	-107.69	9.828	88.47	23.94	0.75
1700	23.96	52.64	37.24	-117.62	9.828	88.25	23.94	0.75
1800	23.96	55.75	37.24	-127.72	9.828	87.99	23.94	0.75
1900	23.96	58.96	37.24	-138.00	9.828	87.69	23.94	0.74
2000	23.96	62.26	37.24	-148.45	9.828	87.36	23.94	0.74
2100	23.96	65.65	37.24	-159.07	9.828	86.99	23.94	0.74
2200	23.96	69.14	37.24	-169.85	9.828	86.57	23.94	0.74
2300	23.96	72.71	37.24	-180.80	9.828	86.11	23.94	0.74
2400	23.96	76.38	37.24	-191.90	9.828	85.61	23.94	0.74
2500	23.96	80.14	37.24	-203.15	9.828	85.07	23.94	0.75

For EoS parameters refer to Table 1.4 on page 75, for EoS formulation refer to the section on page 9.

Table 3.6

Phase: Hf solid β

Atomic weight 178.49

Pressure: 600,000 bar

T (K)	C_P (J/mol K)	H (kJ/mol)	S (J/mol K)	G (kJ/mol)	V (cm ³ /mol)	B (GPa)	C_V (kJ/mol K)	γ
300	23.96	678.07	37.24	661.48	9.828	240.26	23.94	0.41
400	23.96	680.04	37.24	655.66	9.828	239.91	23.94	0.33
500	23.96	682.13	37.24	649.33	9.828	239.59	23.94	0.28
600	23.96	684.30	37.24	642.56	9.828	239.28	23.94	0.24
700	23.96	686.54	37.24	635.43	9.828	238.99	23.94	0.21
800	23.96	688.84	37.24	627.97	9.828	238.71	23.94	0.19
900	23.96	691.19	37.24	620.22	9.828	238.44	23.94	0.18
1000	23.96	693.60	37.24	612.21	9.828	238.17	23.94	0.18
1100	23.96	696.06	37.24	603.95	9.828	237.90	23.94	0.17
1200	23.96	698.58	37.24	595.47	9.828	237.63	23.94	0.17
1300	23.96	701.14	37.24	586.77	9.828	237.36	23.94	0.17
1400	23.96	703.76	37.24	577.87	9.828	237.08	23.94	0.18
1500	23.96	706.42	37.24	568.79	9.828	236.80	23.94	0.19
1600	23.96	709.14	37.24	559.52	9.828	236.51	23.94	0.19
1700	23.96	711.90	37.24	550.09	9.828	236.22	23.94	0.20
1800	23.96	714.72	37.24	540.49	9.828	235.92	23.94	0.21
1900	23.96	717.58	37.24	530.73	9.828	235.62	23.94	0.22
2000	23.96	720.49	37.24	520.82	9.828	235.30	23.94	0.23
2100	23.96	723.46	37.24	510.77	9.828	234.97	23.94	0.24
2200	23.96	726.47	37.24	500.57	9.828	234.64	23.94	0.25
2300	23.96	729.53	37.24	490.23	9.828	234.30	23.94	0.27
2400	23.96	732.64	37.24	479.76	9.828	233.94	23.94	0.28
2500	23.96	735.79	37.24	469.16	9.828	233.58	23.94	0.29

For EoS parameters refer to Table 1.4 on page 75, for EoS formulation refer to the section on page 9.

LIST OF REFERENCES

- Adenstedt, H., 1952. Thermal, and Electrical Properties of Hafnium and High Purity Zirconium. *Transactions of the American Society for Metals* 44, 949–67.
- Ahuja, R., Fast, L., Eriksson, O., Wills, J.M., Johansson, B., 1998. Elastic and high pressure properties of ZnO. *Journal of Applied Physics* 83, 8065.
- Ahuja, R., Rekh, S., Johansson, B., 2001. Theoretical prediction of a phase transition in gold. *PhRvB*. 63, 212101.
- Ahuja, R., Sederlind, P., Trygg, J., Melsen, J., Wills, J., Johansson, B., 1994. Influence of pseudocore valence-band hybridization on the crystal-structure phase stabilities of transition metals under extreme compressions. *PhRvB* 50, 14690–3.
- Aitahcene, T., Monty, C., Kouam, J., Thorel, a, Petotervas, G., Djemel, a, 2007. Preparation by solar physical vapor deposition (SPVD) and nanostructural study of pure and Bi doped ZnO nanopowders. *Journal of the European Ceramic Society* 27, 3413–3424.
- Akahama, Y., Kawamura, H., Bihan, T.L., 2002. A new distorted body-centred cubic phase of titanium (δ -Ti) at pressures up to 220 GPa. *Young* 10583.
- Al'tshuler, L., Bakanova, A., Dudoladov, I., Dynin, E., Trunin, R., Chekin, B., 1981. Shock adiabats for metals. New data, statistical analysis and general regularities. *JAMTP* 22, 145.
- Al'tshuler, L., Krupnikov, K., Brazhnik, M., 1958. Dynamic compressibility of metals under pressures from 400,000 to 4,000,000 atmospheres. *SJETP* 7, 614–9.
- Amonenko, V., Vasyutinskii, B., Kartmazov, G., Smirnov, Y., Finkel, V., 1963. Tantalum Structure at Elevated Temperature. *Fiz Met Metalloved* 15.
- An, Q., Luo, S., Han, L., Zheng, L., Tschauner, O., 2008. Melting of Cu under hydrostatic and shock wave loading to high pressures. *J Phys: Condens Matter* 20, 095220.
- Andersen, G.G., Petrunin, V.V., Baurichter, A., 2005. Numerical calculations of pulsed laser heating of non-isotropic materials, in: *Proceedings of the COMSOL Multiphysics User's Conference*. Stockholm.
- Anderson, C., 1936. The Heat Capacities of Vanadium, Vanadium Trioxide, Vanadium Tetroxide and Vanadium Pentoxide at Low Temperatures. *JACS* 58, 564–6.

- Anderson, O., 1995. Equations of state of solids for geophysics and ceramic science, Equations of state of solids for geophysics and ceramic science. Oxford University Press, USA.
- Angel, R.J., Zhao, J., Ross, N.L., 2005. General Rules for Predicting Phase-Transitions in Perovskites due to Octahedral Tilting. *Physical Review Letters* 95, 025503.
- Asimow, P., Sun, D., Ahrens, T., 2009. Shock compression of preheated molybdenum to 300 GPa. *PEPI* 174, 302–8.
- Baldwin, E.E., 1954. The Thermal Expansion And Elevated Temperature Mechanical Strength Of Hafnium. Knolls Atomic Power Laboratory, Schenectady, N. Y. 1-14.
- Bale, C.W., Bélisle, E., Chartrand, P., Deckerov, S. a., Eriksson, G., Hack, K., Jung, I.-H., Kang, Y.-B., Melançon, J., Pelton, A.D., Robelin, C., Petersen, S., 2009. FactSage thermochemical software and databases — recent developments. *Calphad* 33, 295–311.
- Baran, M., Zhydachevsky, Y., Suchocki, A., Reszka, A., Warchol, S., Diduszko, R., Pajaczowska, A., 2012. No Title. *Optical Materials* 34, 604.
- Batani, D., Balducci, A., Beretta, D., Bernardinello, A., Lower, T., Koenig, M., 2000. Equation of state data for gold in the pressure range < 10 TPa. *PhRvB*. 61, 9287–94.
- Beck, P., Goncharov, A.F., Montoya, J. a., Struzhkin, V.V., Militzer, B., Hemley, R.J., Mao, H.-K., Lett, P., 2009. Response to “Comment on ‘Measurement of thermal diffusivity at high-pressure using a transient heating technique’” [*Appl. Phys. Lett.* 95, 096101 (2009)]. *Applied Physics Letters* 95, 096102.
- Beck, P., Goncharov, A.F., Struzhkin, V.V., Militzer, B., Mao, H., Hemley, R.J., 2007. Measurement of thermal diffusivity at high pressure using a transient heating technique. *Applied Physics Letters* 91, 181914.
- Belonoshko, A., Ahuja, R., Eriksson, O., Johansson, B., 2000. Quasi ab initio molecular dynamic study of Cu melting. *PhRvB*. 61, 3838–44.
- Belonoshko, A., Simak, S., Kochetov, A., Johansson, B., Burakovsky, L., Preston, D., 2004. High-pressure melting of molybdenum. *Phys Rev Lett*. 92, 195701.
- Berne, C., Pasturel, A., Sluiter, M., Vinet, B., 1999. Ab Initio Study of Metastability in Refractory Metal Based Systems. *Phys Rev Lett*. 83, 1621–3.
- Birch, F., 1978. FINITE STRAIN ISOTHERM AND VELOCITIES FOR SINGLE-CRYSTAL AND POLYCRYSTALLINE NaCl AT HIGH-PRESSURES AND 300-DEGREE-K. *Journal of Geophysical Research* 83, 1257–1268.

- Bodea, S., Jeanloz, R., 1989. Model calculations of the temperature distribution in the laser-heated diamond cell. *Journal of Applied Physics* 65, 4688.
- Boehler, R., 1993. Temperatures in the Earth's core from melting-point measurements of iron at high static pressures. *Nature Letters* 363, 534–536.
- Boehler, R., Musshoff, H.G., Ditz, R., Aquilanti, G., Trapananti, a, 2009. Portable laser-heating stand for synchrotron applications. *The Review of scientific instruments* 80, 045103.
- Bolef, D., Smith, R., Miller, J., 1971. Elastic Properties of Vanadium. I. Temperature Dependence of the Elastic Constants and the Thermal Expansion. *PhRvB*. 3, 4100–8.
- Bolef, D.I., De Klerk, J., 1962. Elastic constants of single-crystal Mo and W between 77 and 500 K. *J Appl Phys*. 33, 2311–4.
- Boulfelfel, S., Leoni, S., 2008. Competing intermediates in the pressure-induced wurtzite to rocksalt phase transition in ZnO. *Physical Review B* 78, 1–7.
- Brand, H, Dobson, D., Vofcadlo, L., Wood, I., 2006. Melting curve of copper measured to 16 GPa using a multi-anvil press. *HPR* 26, 185–91.
- Bridgman, P.W., 1923. The Compressibility of Thirty Metals as a Function of Pressure and Temperature. *Proceedings of the American Academy of Arts and Sciences* 58, 165–242.
- Brosh, E., 2009. Personal communication.
- Brosh, E., Makov, G., Shneck, R., 2005. Thermodynamic analysis of light-actinide elements. *Proceedings of the 11th International Symposium on Thermodynamics of Nuclear Materials* 344, 36–9.
- Brosh, E., Makov, G., Shneck, R., 2007. Application of CALPHAD to high pressures. *Calphad* 31, 173–85.
- Brosh, E., Makov, G., Shneck, R., 2009. Thermodynamic analysis of high-pressure phase equilibria in Fe–Si alloys, implications for the inner-core. *PEPI*. 172, 289–98.
- Brosh, E., Shneck, R., Makov, G., 2008. Solids, Explicit Gibbs free energy equation of state for. *Phys Chem Solids*. 69, 1912–22.
- Bujard, P., Sanjines, R., Walker, E., Ashkenazi, J., Peter, M., 1981. Elastic constants in Nb-Mo alloys from zero temperature to the melting point: experiment and theory. *Journal of Physics F: Metal Physics* 775–86.

- Campbell, A.J., 2008. Measurement of temperature distributions across laser heated samples by multispectral imaging radiometry. *The Review of scientific instruments* 79, 015108.
- Carslaw, H.S., Jaeger, J.C., 1959. *Conduction of Heat in Solids*, 2nd ed. Clarendon, Oxford, England.
- Cazorla, C., Gillan, M., Taioli, S., Alf, D., 2007. Ab initio melting curve of molybdenum by the phase coexistence method. *The Journal of chemical physics* 126, 194502.
- Cazorla, C., Gillan, M., Taioli, S., Alfe, D., 2008. Melting curve and Hugoniot of molybdenum up to 400 GPa by ab initio simulations. *Journal of Physics: Conference Series* 121, 012009.
- Cazorla, C., Gillan, M.J., Taioli, S., Alfè, D., 2008. Melting curve and Hugoniot of molybdenum up to 400 GPa by ab initio simulations. *Journal of Physics: Conference Series* 121, 012009.
- Chang, Y., Himmel, L., 1966. Temperature dependence of the elastic constants of Cu, Ag, and Au above room temperature. *J Appl Phys.* 37, 3567.
- Chang, Y., Hultgren, R., 1965. The Dilation Contribution to the Heat Capacity of Copper and α -Brass at Elevated Temperatures. *The Journal of physical chemistry* 69, 4162–5.
- Chen, S.J., Liu, Y.C., Shao, C.L., Xu, C.S., Liu, Y.X., Wang, L., Liu, B.B., Zou, G.T., 2005. No Title. *J. Appl. Phys.* 98, 106106.
- Clark, S.J., Segall, M.D., Pickard, C.J., Hasnip, P.J., Probert, M.J., Refson, K., Payne, M.C., 2005. First principles methods using CASTEP. *Zeitschrift für Kristallographie* 220, 567–570.
- Clendenen, R.L., Drickamer, H.G., 1964. The effect of pressure on the volume and lattice parameters of ruthenium and iron. *J. Phys. Chem. Solids* 25, 865–868.
- Cohen, L., Kennedy, G., 1966. Melting of copper, silver, and gold at high pressures. *PhRv.* 145, 519–25.
- Collard, S., McLellan, R., 1992. High-temperature elastic constants of platinum single crystals. *AcM&M* 40, 699–702.
- Crangle, J., Smith, T., 1962. Specific Heat of Metallic Palladium Between 65 and 105 K. *Phys Rev Lett.* 9, 86–7.
- Cynn, H., Yoo, C., 1999. Equation of state of tantalum to 174 GPa. *PhRvB.* 59, 8526–9.

- Decremps, F., Datchi, F., Saitta, a., Polian, a., Pascarelli, S., Di Cicco, a., Itié, J., Baudelet, F., 2003. Local structure of condensed zinc oxide. *Physical Review B* 68, 1–10.
- Decremps, F., Zhang, J., Liebermann, R.C., 2000. New phase boundary and high-pressure thermoelasticity of ZnO. *Europhysics Letters* 51, 268–274.
- Deemyad, S., Silvera, I.F., 2008. Temperature dependence of the emissivity of platinum in the IR. *The Review of scientific instruments* 79, 086105.
- Desgreniers, S., 1998. High-density phases of ZnO : Structural and compressive parameters. *Physical Review B* 58, 102–105.
- Dewaele, A., Loubeyre, P., Mezouar, M., 2004. Equations of state of six metals above 94GPa. *PhRvB*. 70, 94112.
- Ding, Y., Ahuja, R., Shu, J., Chow, P., Luo, W., Mao, H., 2007. Structural phase transition of vanadium at 69 GPa. *Phys Rev Lett.* 98, 85502.
- Dorogokupets, P., Oganov, A., 2007. Ruby, metals, and MgO as alternative pressure scales: A semiempirical description of shock-wave, ultrasonic, x-ray, and thermochemical data at high temperatures and pressures. *PhRvB* 75, 24115.
- Dorogokupets, P., Oganov, A. (Eds.), 2006. Equations of state of Al, Au, Cu, Pt, Ta, and W and revised ruby pressure scale, in: *Doklady Earth Sciences*. Springer.
- Dubrovinsky, L., Saxena, S., 1997. Thermal expansion of periclase (MgO) and tungsten (W) to melting temperatures. *Phys Chem Miner.* 24, 547–50.
- Dubrovinsky, L.S., Saxena, S.K., 1999a. Emissivity measurements of some metals and oxides using multiwavelength spectral radiometry. *High Temperatures - High Pressures* 31, 393–399.
- Dubrovinsky, L.S., Saxena, S.K., 1999b. Thermal characteristics of melting. *High Temperatures - High Pressures* 31, 385–391.
- Duffy, T.S., Shen, G., Shu, J., Mao, H.-K., Hemley, R.J., Singh, A.K., 1999. Elasticity, shear strength, and equation of state of molybdenum and gold from x-ray diffraction under nonhydrostatic compression to 24 GPa. *Journal of Applied Physics* 86, 6729.
- Dutta, B., Dayal, B., 1963a. Lattice Constants and Thermal Expansion of Palladium and Tungsten up to 878°C by X-Ray Method. *Physica status solidi B: basic solid state physics* 3, 2253–9.

- Dutta, B., Dayal, B., 1963b. Lattice Constants and Thermal Expansion of Gold up to 878°C by X-Ray Method. *Physica status solidi B: basic solid state physics* 3, 473–7.
- Duzynska, A., Hrubciak, R., Drozd, V., Teisseyre, H., Teisseyere, H., Paszkowich, W., Reszka, A., Kaminska, A., Saxena, S.K., Fidelius, J.D., Grabis, J., Monty, C.J., Suchocki, A., 2012. The structural and optical properties of ZnO bulk and nanocrystals under high pressure. *High Pressure Research iFirst*, 1–10.
- Edwards, J., Speiser, R., Johnston, H., 1951. High temperature structure and thermal expansion of some metals as determined by x-ray diffraction data. I. Platinum, tantalum, niobium, and molybdenum. *J Appl Phys.* 22, 424.
- Ellner, M., 2004. Bond energy in palladium and platinum-rich alloys with the A4 transition metals. *Journal of Alloys and Compounds* 366, 222–227.
- Eriksson, G., Hack, K., 1990. ChemSage- A computer program for the calculation of complex chemical equilibria. *Metallurgical and Materials Transactions B* 21, 1013–23.
- Errandonea, D., 2004a. Comment on “Theoretical solid and liquid state shock Hugoniot of Al, Ta, Mo and W”. *J Phys: Condens Matter* 16, 8801.
- Errandonea, D., 2004b. Comment on Theoretical solid and liquid state shock Hugoniot of Al, Ta, Mo and W . *Journal of Physics: Condensed Matter* 16, 8801–8804.
- Errandonea, D., 2005. Improving the understanding of the melting behaviour of Mo, Ta, and W at extreme pressures. *Physica B: Condensed Matter* 357, 356–364.
- Errandonea, D., 2006. Phase behavior of metals at very high PT conditions: A review of recent experimental studies. *J Phys Chem Solids* 67, 2017–26.
- Errandonea, D., 2010. The melting curve of ten metals up to 12 GPa and 1600 K. *J Appl Phys.* 108, 033517–10.
- Errandonea, D., Boehler, R., Ross, M., 2000. Melting of the rare earth metals and f-electron delocalization. *Physical review letters* 85, 3444–7.
- Errandonea, D., Boehler, R., Ross, M., 2001. Melting of the alkaline-earth metals to 80 GPa. *Physical Review B* 65, 1–4.
- Errandonea, D., Meng, Y., Somayazulu, M., Hausermann, D., 2005. Pressure-induced transition in titanium metal: a systematic study of the effects of uniaxial stress. *Physica B: Condensed Matter* 355, 116–125.

- Errandonea, D., Schwager, B., Ditz, R., Gessmann, C., Boehler, R., Ross, M., 2001a. Systematics of transition-metal melting. *Physical Review B* 63, 2–5.
- Errandonea, D., Schwager, B., Ditz, R., Gessmann, C., Boehler, R., Ross, M., 2001b. Systematics of transition-metal melting. *PhRvB* 63, 132104.
- Errandonea, D., Somayazulu, M., Husermann, D., Mao, H., 2003. Melting of tantalum at high pressure determined by angle dispersive x-ray diffraction in a double-sided laser-heated diamond-anvil cell. *J Phys: Condens Matter* 15, 7635.
- Esser, H., Eusterbrock, H., 1941. Untersuchung der Warmausdehnung von einigen Metallen und Legierungen mit einem verbesserten Dilatometer. *Arch Eisenhüttenw* 14, 341.
- Fabrichnaya, O., Saxena, S.K., Richet, P., 2004. Thermodynamic Data on Solid Phases in the System: MgO-FeO-Fe₂O₃-Al₂O₃-SiO₂. An assessment based on calorimetric and phase equilibrium data.
- Falcon, H., 2004. Neutron diffraction study, magnetism and magnetotransport of stoichiometric CaVO₃ perovskite with positive magnetoresistance. *Journal of Solid State Chemistry* 177, 3099–3104.
- Fateeva, N., Vereshchagin, L., 1971. Melting Curve of Molybdenum up to 90 kbar. *JETP Letters* 14, 153–4.
- Featherston, F., Neighbours, J., 1963. Elastic constants of tantalum, tungsten, and molybdenum. *PhRv.* 130, 1324–33.
- Fei, Y., Li, J., Hirose, K., Minarik, W., Van Orman, J., Sanloup, C., 2004. A critical evaluation of pressure scales at high temperatures by in situ X-ray diffraction measurements. *New Developments in High-Pressure Mineral Physics and Applications to the Earth's Interior.* 515–26.
- Fei, Y., Ricolleau, A., Frank, M., Mibe, K., Shen, G., Prakapenka, V., 2007. Toward an internally consistent pressure scale. *Proceedings of the National Academy of Sciences of the United States of America* 104, 9182–6.
- Feldman, J., Horton, G., 1965. Critical Analysis of the Thermodynamic Data for Pt and a Prediction of $\Theta_{DW}(T)$. *PhRv.* 137, A1106–A8.
- Fidelus, J.D., Karbowski, A., Grabis, J., Jusza, A., Piramidowicz, R., Brusa, R.S., Karwasz, G.P., 2012. Positron-Annihilation, Structural and Optical Studies on Properties of Nanostructured ZrO₂, ZnO, Bi₂O₃ and ZnO–Bi₂O₃. *ACTA PHYSICA POLONICA A* 120, 66–68.

- Fried, L.E., M., H.W., 2000. Explicit Gibbs free energy equation of state applied to the carbon phase diagram. *Physical Review B* 61, 8734–43.
- Funamori, N., Yagi, T., Uchida, T., 1994. Deviatoric stress measurement under uniaxial compression by a powder x-ray diffraction method. *J. Appl. Phys.* 75, 4327–4331.
- Furukawa, G., Reilly, M., Gallagher, J., 1974. Critical Analysis of Heat-Capacity Data and Evaluation of Thermodynamic Properties of Ruthenium, Rhodium, Palladium, Iridium, and Platinum from 0 to 300 K. A Survey of the Literature Data on Osmium. *J Phys Chem Ref Data* 3.
- Gathers, G., 1986. Hugoniot measurements for vanadium. *J Appl Phys.* 59, 3291.
- Geballe, T., Giaque, W., 1952. The Heat Capacity and Entropy of Gold from 15 to 300° K. *JACS* 74, 2368–9.
- Gehlen, P., 1969. A 77–1300 K Single Crystal X-Ray Specimen Chamber. *Rev Sci Instrum.* 40, 715.
- Gerward, L., Olsen, J.S., 1995. The High-Pressure Phase of Zincite. *Journal of Synchrotron Radiation* 2, 233–235.
- Giauque, WF, Meads, P., 1941. The Heat Capacities and Entropies of Aluminum and Copper from 15 to 300° K. *JACS* 63, 1897–901.
- Girifalco, L., 2000. *Statistical mechanics of solids*. Oxford University Press, USA.
- Glazer, A.M., 1972. The Classification of Titled Octahedra in Perovskites. *Acta Crystallographica B*28, 3384.
- Goldstein, R., 2003. Heat transfer—a review of 2001 literature. *International Journal of Heat and Mass Transfer* 46, 1887–1992.
- Golutvin, Y.M., Maslennikova, E.G., 1970. The Heat Capacity Of Metallic Hafnium. *Izv. Akad. Nauk Sssr, Metal.* 5, 174–83.
- Goncharov, A.F., Beck, P., Struzhkin, V.V., Haugen, B.D., Jacobsen, S.D., 2009. Thermal conductivity of lower-mantle minerals. *Physics of the Earth and Planetary Interiors* 174, 24–32.
- Greeff, C., Boettger, J., Graf, M., Johnson, J., 2006. Theoretical investigation of the Cu EOS standard. *SMEC 2005, Study of matter under extreme conditions* 67, 2033–40.
- Greeff, C., Graf, M., 2004. Lattice dynamics and the high-pressure equation of state of Au. *PhRvB.* 69, 054107.

- Greeff, C.W., 2005. Phase changes and the equation of state of Zr. *Modelling and Simulation in Materials Science and Engineering* 13, 1015–1027.
- Grigorjeva, L., Millers, D., Pankratov, V., Kalinko, a, Grabis, J., Monty, C., 2007. Blue luminescence in ZnO single crystals, nanopowders, ceramic. *Journal of Physics: Conference Series* 93, 012036.
- Groulx, D., Ogoh, W., 2009. Solid-Liquid Phase Change Simulation Applied to a Cylindrical Latent Heat Energy Storage System.
- Guillermet, A., Grimvall, G., 1991. Analysis of thermodynamic properties of molybdenum and tungsten at high temperatures. *PhRvB* 44, 4332–40.
- Guillermet, A.F., Fernandez Guillermet, A., 1985. Critical evaluation of the thermodynamic properties of molybdenum. *Int J Thermophys.* 6, 367–93.
- Gülseren, O., Cohen, R., 2002. High-pressure thermoelasticity of body-centered-cubic tantalum. *PhRvB.* 65, 64103.
- Hammersley, A., 2009. <http://www.esrf.eu/computing/scientific/FIT2D/> [WWW Document]. URL <http://www.esrf.eu/computing/scientific/FIT2D/>
- Heinz D, J.R., 1984. The equation of state of the gold calibration standard. *J Appl Phys.* 55, 885–93.
- Hemley, R.J., Mao, H., Shen, G., Badro, J., Gillet, P., Hanfland, M., 1997. X-ray Imaging of Stress and Strain of Diamond, Iron, and Tungsten at Megabar Pressures. *Science* 276, 1242–1245.
- Hixson, R., Boness, D., Shaner, J., Moriarty, J., 1989. Acoustic Velocities and Phase Transitions in Molybdenum under Strong Shock Compression. *Phys Rev Lett.* 62, 637–40.
- Hixson, R., Fritz, J., 1992. Shock compression of tungsten and molybdenum. *J Appl Phys.* 71, 1721.
- Hofmeister, A.M., 2007. Pressure dependence of thermal transport properties. *Proceedings of the National Academy of Sciences of the United States of America* 104, 9192–7.
- Hofmeister, A.M., 2009. Comment on “Measurement of thermal diffusivity at high pressure using a transient heating technique” [*Appl. Phys. Lett.* 91, 181914 (2007)]. *Applied Physics Letters* 95, 096101.

- Holmes, N., Moriarty, J., Gathers, G., Nellis, W., 1989. The equation of state of platinum to 660 GPa (6.6 Mbar). *J Appl Phys.* 66, 2962–7.
- Holzzapfel, W., 2010a. Equations of state for Cu, Ag, and Au and problems with shock wave reduced isotherms. *HPR* 30, 372–94.
- Holzzapfel, W. (Ed.), 2010b. Problems in shock wave reduced isotherms, in: *Physics of Extreme States of Matter*.
- Holzzapfel, W., Hartwig, M., Sievers, W., 2001. Equations of state for Cu, Ag, and Au for wide ranges in temperature and pressure up to 500 GPa and above. *J Phys Chem Ref Data* 30, 515–30.
- Hrubiak, R., Drozd, V., Karbasi, A., Saxena, S.K., 2012. High P-T phase transitions and P-V-T equation of state of hafnium. *Journal of Applied Physics* 111, 112612.
- Hsu, M.-F., Wu, L.-J., Jenn-Ming, W., Shiu, Y.-H., Lin, and K.-F., 2006. Solid Oxide Fuel Cell Fabricated Using All-Perovskite Materials. *Electrochem. Solid-State Lett.* 9, A193.
- Hubbell, W., Brotzen, F., 1972. Elastic constants of niobium-molybdenum alloys in the temperature range -190 to +100°C. *J Appl Phys.* 43, 3306.
- Hugoniot equation of state measurements for eleven materials to five megabars, 1968. .
- Hume-Rothery, W., Reynolds, P., 1938. A High-Temperature Debye-Scherrer Camera, and Its Application to the Study of the Lattice Spacing of Silver. *Proceedings of the Royal Society of London Series A, Mathematical and Physical Sciences*.
- Hung, V., Van, Hai, N., Thanh, 1997. Investigation of the Melting Temperature of Metal at Various Pressures. *J Phys Soc Jpn.* 66.
- Jacobs, M.H.G., Oonk, H.A.J., H.A.J., O., 2000. A realistic equation of state for solids. The high pressure and high temperature thermodynamic properties of MgO. *Calphad* 24, 133–147.
- Jaffe, J.E., Hess, A.C., 1993. Hartee-Fock study of phase changes in ZnO at high pressure. *Physical Review B* 48, 7903–7909.
- Jaffe, J.E., Snyder, J.A., Lin, Z., Hess, A.C., 2000. LDA and GGA calculations for high-pressure phase transitions in ZnO and MgO. *Physical Review B* 62, 1660–1665.
- Jamieson, J.C., Fritz, J.N., Manghnani, M.H., 1982. Pressure Measurement at High Temperature in X-Ray Diffraction Studies: Gold as a Primary Standard. *High-pressure research in geophysics* 140, 27–47.

- Japel, S., Schwager, B., Boehler, R., Ross, M., 2005. Melting of copper and nickel at high pressure: The role of d electrons. *Phys Rev Lett.* 95, 167801.
- Jayaraman, A., 1986. Ultrahigh pressures. *Review of Scientific Instruments* 57, 1013.
- Jeanloz, R., Kavner, a., Lazor, P., Saxena, S.K., 1996. Melting Criteria and Imaging Spectroradiometry in Laser-Heated Diamond-Cell Experiments [and Discussion Comment]. *Philosophical Transactions of the Royal Society A: Mathematical, Physical and Engineering Sciences* 354, 1279–1307.
- Jeong, J.-W., Chang, K., 1999. Molecular-dynamics simulations for the shock Hugoniot meltings of Cu, Pd and Pt. *J Phys: Condens Matter.* 11, 3799.
- Joshi, K.D., Jyoti, G., Gupta, S.C., Sikka, S.K., 2002. Some aspects of pressure-induced transformation in group IVB elements. *Journal of Physics: Condensed Matter* 14, 10921–10925.
- Kalinko, a, Fidelus, J.D., Grigorjeva, L., Millers, D., Monty, C.J., Presz, a, Smits, K., 2007. The luminescence properties of ZnO nanopowders. *Journal of Physics: Conference Series* 93, 012044.
- Kantola, M., Tokola, E., 1967. X-RAY Studies on the Thermal Expansion of Copper - Nickel Alloys. *ANNALES ACADEMIAE SCIENTIARUM FENNICAE, SERIES A6, PHYSICA.* 223, 3–11.
- Karbasi, A., Saxena, S.K.K., Hrubciak, R., 2011. The thermodynamics of several elements at high pressure. *Calphad* 35, 72–81.
- Karzel, H., Potzel, W., Köfferlein, M., Schiessl, W., Steiner, M., Hiller, U., Kalvius, G., Mitchell, D., Das, T., Blaha, P., Schwarz, K., Pasternak, M., 1996. Lattice dynamics and hyperfine interactions in ZnO and ZnSe at high external pressures. *Physical review. B, Condensed matter* 53, 11425–11438.
- Kavner, A., Jeanloz, R., 1998. High-pressure melting curve of platinum. *J Appl Phys.* 83, 7553.
- Kavner, A., Nugent, C., 2008. Precise measurements of radial temperature gradients in the laser-heated diamond anvil cell. *The Review of Scientific Instruments* 79, 024902.
- Kiefer, B., Duffy, T.S., 2005. Finite element simulations of the laser-heated diamond-anvil cell. *Journal of Applied Physics* 97, 114902.
- Kirby, R.K.R.K., 1991. Platinum, A thermal expansion reference material. *Int J Thermophys.* 12, 679–85.

- Kittel, C., McEuen, P., 1996. Introduction to solid state physics. Wiley, New York.
- Klingshirn, C., Fallert, J., Zhou, H., Sartor, J., Thiele, C., Maier-Flaig, F., Schneider, D., Kalt, H., 2010. 65 years of ZnO research - old and very recent results. *Physica Status Solidi (B)* 247, 1424–1447.
- Komabayashi, T., Fei, Y., 2010. Internally consistent thermodynamic database for iron to the Earth's core conditions. *Journal of Geophysical Research* 115, 1–12.
- Konopkova, Z., Lazor, P., Goncharov, A.F., Struzhkin, V.V., Ztruzhkin, V.V., 2011. Thermal conductivity of hcp iron at high pressure and temperature. *High Pressure Research* 31, 228–236.
- Krupnikov, K., Bakanova, A., Brazhnik, M., Trunin, R. (Eds.), 1963. An Investigation of the Shock Compressibility of Titanium, Molybdenum Tantalum, and Iron, in: SPbD.
- Leisure, R., Hsu, D., Seiber, B., 1973. Elastic properties of tantalum over the temperature range 4,300 K. *J Appl Phys.* 44, 3394.
- Liu, H., Ding, Y., Somayazulu, M., Qian, J., Shu, J., Häusermann, D., Mao, H., 2005. Rietveld refinement study of the pressure dependence of the internal structural parameter u in the wurtzite phase of ZnO. *Physical Review B* 71, 1–4.
- Liu, W., Li, B., Wang, L., Zhang, J., Zhao, Y., 2008. Simultaneous ultrasonic and synchrotron x-ray studies on pressure induced α - ω phase transition in zirconium. *Journal of Applied Physics* 104, 076102.
- Liu, Z.-K., Wang, Y., Shang, S.-L., 2011. Origin of negative thermal expansion phenomenon in solids. *Scripta Materialia* 65, 664–667.
- Liu, Z.-L., Zhang, X.-L., Cai, L.-C., Chen, X.-R., Wu, Q., Jing, F.-Q., 2008. Thermal equation of state, and melting and thermoelastic properties of bcc tantalum from molecular dynamics. *J Phys Chem Solids* 69, 2833–40.
- Lowrie, R., Gonas, A., 1967. Single-Crystal Elastic Properties of Tungsten from 24° to 1800°C. *J Appl Phys.* 38, 4505–9.
- Lu, X.-G., Chen, Q., 2009. A CALPHAD Helmholtz energy approach to calculate thermodynamic and thermophysical properties of fcc Cu. *PMag.* 89, 2167.
- Lu, X.-G., Selleb, Y.M., Sundman, B., 2005. Theoretical modeling of molar volume and thermal expansion. *Acta Mater.* 53, 2259–72.
- Lu, X.-G., Selleby, M., Sundman, B., 2005a. Implementation of a new model for pressure dependence of condensed phases in Thermo-Calc. *Calphad* 29, 49–55.

- Lu, X.-G., Selleby, M., Sundman, B., 2005b. Assessments of molar volume and thermal expansion for selected bcc, fcc and hcp metallic elements. *Calphad* 29, 68–89.
- Lukas, H., Fries, S.G., B., S., 2007. *The Calphad Method*, in: *Computational Thermodynamics*. Cambridge University Press, New York.
- Luo, S., Swift, D., 2007. On high-pressure melting of tantalum. *Physica B: Condensed Matter* 388, 139–44.
- Maekawa, T., Kurosaki, K., Yamanaka, S., 2006. Physical properties of polycrystalline SrVO₃- δ . *Journal of Alloys and Compounds* 426, 46–50.
- Mao, H.K., Bell, P.M., 1978. Specific volume measurements of Cu, Mo, Pd and Ag and calibration of the ruby R1 fluorescence pressure gauge from 0.06 to 1 Mbar. *J. Appl. Phys.* 49, 3276–3283.
- Mao, H.K., Bell, P.M., Shaner, J.W., Steinberg, D.J., 1978. Specific volume measurements of Cu, Mo, Pd, and Ag and calibration of the ruby R fluorescence pressure gauge from 0.06 to 1 Mbar. *J Appl Phys.* 49, 3276.
- Mao, H.K., Xu, J., Bell, P.M., 1986. Calibration of the Ruby Pressure Gauge to 800 kbar Under Quasi-Hydrostatic Conditions. *Journal of Geophysical Research* 91, 4673–4676.
- Marsh, S., 1980. *LASL shock Hugoniot data*. University of California Press.
- McCluskey, M.D., Jokela, S.J., 2009. Defects in ZnO. *Journal of Applied Physics* 106, 071101.
- McQueen, R., Marsh, S., 1960. Equation of state for nineteen metallic elements from shock-wave measurements to two megabars. *J Appl Phys* 31, 1253.
- McQueen, R., Marsh, S., Taylor, J., Fritz, J., Carter, W., 1970. The equation of state of solids from shock wave studies. *High Velocity Impact Phenomena*. *High Velocity Impact Phenomena* 294, 417.
- Meads, P., Forsythe, W., Giauque, W., 1941. The Heat Capacities and Entropies of Silver and Lead from 15° to 300° K. *JACS* 63, 1902–5.
- Meng, Y., Shen, G., Mao, H.K., 2006a. Double-sided laser heating system at HPCAT for in situ x-ray diffraction at high pressures and high temperatures. *Journal of Physics: Condensed Matter* 18, S1097–S1103.

- Meng, Y., Shen, G., Mao, H.K., 2006b. Double-sided laser heating system at HPCAT for in situ x-ray diffraction at high pressures and high temperatures. *Journal of Physics: Condensed Matter* 18, S1097–S1103.
- Miller, G., Ahrens, T., Stolper, E., 1988. The equation of state of molybdenum at 1400 C. *J Appl Phys.* 63, 4469.
- Milman, V., Winkler, B., White, J.A., Pickard, C.J., Payne, M.C., Akhmatkaya, E.V., Nobes, R.H., 2000. Electronic structure, properties, and phase stability of inorganic crystals: A pseudopotential plane-wave study. *International Journal of Quantum Chemistry* 77, 895–910.
- Milošević, N.D., Maglić, K.D., 2006. Thermophysical Properties of Solid Phase Zirconium at High Temperatures. *International Journal of Thermophysics* 27, 1140–1159.
- Ming, L., Manghnani, M., 1978. Isothermal compression of bcc transition metals to 100 kbar. *Appl Phys.* 49, 208.
- Mitchell, A., Nellis, W., 1981. Shock compression of aluminum, copper, and tantalum. *J Appl Phys.* 52, 3363.
- Mitra, N., Decker, D., Vanfleet, H., 1967. Melting curves of copper, silver, gold, and platinum to 70 kbar. *PhRv.* 161, 613–7.
- Morgan, J., 1974. The equation of state of platinum to 680 GPa. *High Temperatures - High Pressures* 6, 195–201.
- Mori, Y., Niiya, N., Ukegawa, K., Mizuno, T., Takarabe, K., Ruoff, a. L., 2004. High-pressure X-ray structural study of BeO and ZnO to 200 GPa. *Physica Status Solidi (B)* 241, 3198–3202.
- Moriarty, J., 1992a. Ultrahigh-pressure structural phase transitions in Cr, Mo, and W. *Physical review. B, Condensed matter* 45, 2004–2014.
- Moriarty, J., 1994. Angular forces and melting in bcc transition metals: A case study of molybdenum. *PhRvB.* 49, 12431–45.
- Moriarty, J., 2002. Quantum-based atomistic simulation of materials properties in transition metals. *J Phys: Condens Matter* 14, 2825.
- Moriarty, J.A., 1992b. Ultrahigh-pressure structural phase transitions in Cr, Mo, and W. *PhRvB.* 45, 2004–14.

- Morishima, H., Yusa, H., Introduction, I., 1998. Numerical calculations of the temperature distribution and the cooling speed in the laser-heated diamond anvil cell. *Journal of Applied Physics* 83, 4572–4577.
- Munn, R.W., 1969. The thermal expansion of axial metals. *Advances in Physics* 18, 515–43.
- Murnaghan, F.D., 1944. The compressibility of media under extreme pressures. *Proceedings of the National Academy of Sciences of the United States of America* 30, 244–247.
- Nakamoto, Y., Takemura, K., Ishizuka, M., Shimizu, K., Kikegawa, T. (Eds.), 2005. Equation of State for Vanadium under Hydrostatic Conditions, in: Joint 20th AIRAPT – 43th EHPRG. Karlsruhe/Germany.
- Nekrasov, I.A., Keller, G., Kondakov, D.E., Kozhevnikov, a. V., Pruschke, T., Held, K., Vollhardt, D., Anisimov, V., 2005. Comparative study of correlation effects in CaVO_3 and SrVO_3 . *Physical Review B* 72, 1–6.
- Nix, F., MacNair, D., 1942. The Thermal Expansion of Pure Metals. II: Molybdenum, Palladium, Silver, Tantalum, Tungsten, Platinum, and Lead. *PhRv.* 61, 74–8.
- Nizhankovskii, V.I., 1994. Anisotropy of the thermal expansion of titanium due to proximity to an electronic topological transition. *Pis'ma Zh. Eksp. Teor. Fiz.* 59, 693–696.
- Novikov, D.L., 1999. Anisotropy of thermal expansion and electronic topological transitions in Zn and Cd under pressure. *Physical Review B* 59, 4557–4560.
- Nowak, J.W., Braithwaite, R.S.W., Nowak, J., Ostojski, K., Krystek, M., Buchowiecki, W., 2007. Formation of large synthetic zincite (ZnO) crystals during production of zinc white. *The Journal of Gemmology* 30, 257–267.
- Odier, P., Bassat, J.M., Loup, J.P., 1995. SrVO_3 and Sr_2VO_4 electrical properties below and above room T. *Solid state Communications* 93, 579–583.
- Oganov, A., Dorogokupets, P., 2004. Intrinsic anharmonicity in equations of state and thermodynamics of solids. *J Phys: Condens Matter.* 16, 1351–60.
- Ono, S., Oganov, a, Brodholt, J., Vocadlo, L., Wood, I., Lyakhov, a, Glass, C., Cote, a, Price, G., 2008. High-pressure phase transformations of FeS: Novel phases at conditions of planetary cores. *Earth and Planetary Science Letters* 272, 481–487.
- Ostanin, S., 2000. Calculation of the P–T phase diagram of hafnium. *Computational Materials Science* 17, 174–177.

- Overton, W., Gaffney, J., 1955. Temperature variation of the elastic constants of cubic elements. *PhRv.* 98, 969–77.
- Owen, E., Yates, E., 1934. Thermal Expansion of Crystal Lattices of Silver, Platinum and Zinc. *PMag.* 113–31.
- Panero, W.R., Jeanloz, R., 2001a. The effect of sample thickness and insulation layers on the temperature distribution in the laser-heated diamond cell. *Review of Scientific Instruments* 72, 1306.
- Panero, W.R., Jeanloz, R., 2001b. Temperature gradients in the laser-heated diamond anvil cell. *Journal of Geophysical Research* 106, 6493–6498.
- Parker, W.J., Jenkins, R.J., Butler, C.P., Abbot, G.L., 1961. Flash Method of Determining Thermal Diffusivity, Heat Capacity, and Thermal Conductivity. *Journal of Applied Physics* 32, 1679–1684.
- Pecker, S., Eliezer, S., Fisher, D., Henis, Z., Zinamon, Z., 2005. A multiphase equation of state of three solid phases, liquid, and gas for titanium. *Journal of Applied Physics* 98, 043516.
- Pialoux, A., Joyeux, M., Cizeron, G., 1982. Étude du comportement du niobium sous vide par diffraction des rayons X à haute température. *Journal of the Less Common Metals* 87, 1–19.
- Pérez-Prado, M., Zhilyaev, a., 2009. First Experimental Observation of Shear Induced hcp to bcc Transformation in Pure Zr. *Physical Review Letters* 102, 4–7.
- Rao, C., Rao, K., 1964. Effect of temperature on the lattice parameters of some silver-palladium alloys. *Can J Phys.* 42, 1336–42.
- Rao, R.R., 1974. Anderson-Gruneisen parameter d of some hexagonal metals and MgO from third-order elastic-constant data. *Physical Review B* 10, 4173–4177.
- Rao, R.R., Menon, C.S., 1973. Lattice specific heat and thermal expansion of titanium. *Physical Review B* 7, 644–650.
- Rayne, J., 1960. Elastic Constants of Palladium from 4. 2-300° K. *PhRv.* 118, 1545–9.
- Recio, J.M., Blanco, M.A., Luan, V., Pandey, R., Gerward, L., Olsen, J.S., 1998. Compressibility of the high-pressure rocksalt phase of ZnO. *Physical Review B* 58, 1–6.
- Rolfé, C., 1966. The Lattice Parameters of Pure Gold. *Journal Institute of Metals* 94, 148.

- Ross, M., Boehler, R., Errandonea, D., 2007. Melting of transition metals at high pressure and the influence of liquid frustration: The late metals Cu, Ni, and Fe. *PhRvB* 76, 184117.
- Ross, M., Yang, L., Boehler, R., 2004. Melting of aluminum, molybdenum, and the light actinides. *PhRvB* 70, 184112.
- Ross, R., Hume-Rothery, W., 1963. High Temperature X-Ray Metallography. *Journal of the Less-common Metals*. 5, 258.
- Ross, R.G., Andersson, P., Sundqvist, B., Bäckström, G., 1984. Thermal conductivity of solids and liquids under pressure. *Reports of Progress in Physics* 47, 1347–1402.
- Ruoff, A., Xia, H., Luo, H., Vohra, Y., 1990. Miniaturization techniques for obtaining static pressures comparable to the pressure at the center of the earth: X-ray diffraction at 416 GPa. *Rev Sci Instrum*. 61, 3830.
- Rupp, J., Birringer, R., 1987. Enhanced specific-heat-capacity (cp) measurements (150 - 300 K) of nanometer-sized crystalline materials. *PhRvB*. 36, 7888–90.
- Santamaria-Perez, D., Ross, M., Errandonea, D., Mukherjee, G., Mezouar, M., Boehler, R., 2009. X-ray diffraction measurements of Mo melting to 119 GPa and the high pressure phase diagram. *The Journal of Chemical Physics* 130, 124509–8.
- Saxena, S.K., 1996. Earth mineralogical model: Gibbs free energy minimization computation in the system MgO--FeO--SiO₂. *Geochim Cosmochim Acta*. 60, 2379–95.
- Saxena, S.K., Shen, G., Lazor, P., 1994. Temperatures in Earth's Core Based on Melting and Phase Transformation Experiments on Iron. *Science (New York, N.Y.)* 264, 405–7.
- Saxena, S.K., Zhang, J., 1990. Thermochemical and pressure-volume-temperature systematics of data on solids, examples: tungsten and MgO. *Phys Chem Miner.* 17, 45–51.
- Scheel, K., 1921. About the thermal expansion of some substances. I [in German]. *ZPhyA*. 5, 167–72.
- Schröder, R., Schmitz-Pranghe, N., Kohlhaas, R., 1972. Experimental determination of the lattice parameters of platinum metals in the temperature range of 190-1709 C [in German]. *Zeitschrift für Metallk* 63, 6.
- Sha, X., Cohen, R.E., 2010. First-principles thermal equation of state and thermoelasticity of hcp Fe at high pressures. *Physical Review B* 81, 1–10.

- Shen, G.Y., Rivers, M.L., Wang, Y.B., Sutton, S.R., 2001. Laser heated diamond cell system at the Advanced Photon Source for in situ x-ray measurements at high pressure and temperature. *Review of Scientific Instruments* 72, 1273.
- Shim, S., Duffy, T., Takemura, K., 2002. Equation of state of gold and its application to the phase boundaries near 660 km depth in Earth's mantle. *Earth Planet Sci Lett.* 203, 729–39.
- Shoemaker, G., Rayne, J., 1968. Specific heat of platinum from 1.4 to 100° K. *Phys Lett A.* 26, 222–3.
- Shuker, P., Melchior, a, Assor, Y., Belker, D., Sterer, E., 2008. IR pyrometry in diamond anvil cell above 400 K. *The Review of scientific instruments* 79, 073908.
- Sikka, S.K., Yohra, Y.K., Chidambaram, R., 1982. Omega phase in materials. *Progress in Materials Science* 27, 245–310.
- Simmons, R., Balluffi, R., 1960. Measurement of the Equilibrium Concentration of Lattice Vacancies in Silver Near the Melting Point. *PhRv.* 119, 600–5.
- Simmons, R., Balluffi, R., 1962. Measurement of Equilibrium Concentrations of Lattice Vacancies in Gold. *PhRv.* 125, 862–72.
- Simmons, R., Balluffi, R., 1963. Measurement of equilibrium concentrations of vacancies in copper. *PhRv.* 129, 1533–44.
- Singh, A., Mao, H., Shu, J., Hemley, R., 1998. Estimation of Single-Crystal Elastic Moduli from Polycrystalline X-Ray Diffraction at High Pressure: Application to FeO and Iron. *Physical Review Letters* 80, 2157–2160.
- Singh, A.K., 1993. The lattice strains in a specimen (cubic system) compressed nonhydrostatically in an opposed anvil device. *J. Appl. Phys.* 73, 4278–4286.
- Singh, A.K., Balasingh, C., 1994. The lattice strains in a specimen (hexagonal system) compressed nonhydrostatically in an opposed anvil high pressure setup. *J. Appl. Phys.* 75, 4956–4962.
- Singh, A.K., Kenichi, T., 2001. Measurement and analysis of nonhydrostatic lattice strain component in niobium to 145 GPa under various fluid pressure-transmitting media. *Journal of Applied Physics* 90, 3269.
- Singh, N., 1999. Structural phase transformation of Cu, Pd and Au using transition metal pair potential. *Physica B: Condensed Matter* 269, 211–220.

- Souvatzis, P., Eriksson, O., Katsnelson, M.I., 2008. Anomalous thermal expansion in alpha-titanium.
- Speirs, R.S., n.d. Crystal Structures of Titanium, Zirconium,. Young 140, 2–3.
- Spreadborough, J., Christian, J., 1959. High-temperature X-ray diffractometer. *JSci.* 36, 116–8.
- Stixrude, L., Lithgow-Bertelloni, C., 2005. Thermodynamics of mantle minerals - I. Physical properties. *Geophysical Journal International* 162, 610–632.
- Suchocki, A., Paszkowicz, W., Kaminska, A., Durygin, A., Saxena, S.K., Arizmendi, L., Bermudez, V., 2006. No Title. *Appl. Phys. Lett.* 89, 261908.
- Suh, I., Ohta, H., Waseda, Y., 1988. High-temperature thermal expansion of six metallic elements measured by dilatation method and X-ray diffraction. *JMatS.* 23, 757–60.
- Sun, T., Umemoto, K., Wu, Z., Zheng, J.-C., Wentzcovitch, R., 2008. Lattice dynamics and thermal equation of state of platinum. *PhRvB* 78, 024304.
- Söderlind, P., 2002. Comment on “Theoretical prediction of phase transition in gold”. *PhRvB.* 66, 176201.
- Taioli, S., Cazorla, C., Gillan, M., Alfe, D., 2008. Ab-initio melting curve and principal Hugoniot of tantalum. *Journal of Physics: Conference Series* 121, 012010.
- Takahashi, Y., Nakamura, J., 1996. The heat capacity of tantalum from 80 to 1000 K. *Thermochim Acta.* 282, 317–22.
- Takemura, K., 2001. Evaluation of the hydrostaticity of a helium-pressure medium with powder x-ray diffraction techniques. *J Appl Phys.* 89, 662–8.
- Takemura, K., Singh, A., 2006. High-pressure equation of state for Nb with a helium-pressure medium: Powder x-ray diffraction experiments. *PhRvB.* 73, 224119–28.
- The MathWorks Inc., 2007. MATLAB.
- Thiel, M., Kusubov, A., 1966. Compendium of shock wave data.
- Tian, R., Sun, J., Yang, W., Xue, X., Yu, F., 2008. An analytic equation of state based on analytic mean-field potential approach and application to three phases of metallic Zirconium. *Central European Journal of Physics* 6, 704–710.

- Tian, R., Sun, J., Zhang, C., Wang, F., 2008. Two equations of state considering the thermal effect for alpha, beta and omega phases of zirconium. *Modern Physics Letters B* 22, 167–180.
- Tolbert, S.H., Alivisatos, A.P., 1993. Size dependence of the solid-solid phase transition in CdSe nanocrystals 9 GPa. *Z. Phys. D: Atoms, Molecules and Clusters* 26, 56–58.
- Touloukian, Y.S., Kirby, R.K.R., Taylor, R.E.R., Desai, P.D., 1979a. Thermophysical Properties of Matter, in: *Metallic Elements and Alloys*.
- Touloukian, Y.S., Kirby, R.K.R., Taylor, R.E.R., Desai, P.D., 1979b. Thermal Expansion, *Metallic Elements and Alloys, Volume 12*, in: *Thermophysical Properties of Matter*.
- Uchida, T., Funamori, N., Yagi, T., 1996. Lattice strains in crystals under uniaxial stress field. *Journal of Applied Physics* 80, 739.
- Ueda, Y., 1998. Oxygen Nonstoichiometry, Structures, and Physical Properties of $\text{CaVO}_3-\delta$ I. A Series of New Oxygen-Deficient Phases. *Journal of Solid State Chemistry* 135, 36–42.
- Vasyutinskii, B., Kartmazov, G., Smirnov, Y., Finkel, V., 1966. Niobium and Vanadium Crystal Structure at High Temperature. *Phys Metals Metallogr.* 21, 134.
- Verma, A., 2004. Theoretical solid and liquid state shock Hugoniot of Al, Ta, Mo and W. *J Phys: Condens Matter* 16, 4799.
- Verma, A., Modak, P., 2008. Structural phase transitions in vanadium under high pressure. *Europhys Lett.* 81, 37003.
- Vermaak, J., Kuhlmann-Wilsdorf, D., 1968. Measurement of the average surface stress of gold as a function of temperature in the temperature range 50-985. deg. *J Phys Chem.* 72, 4150–4.
- Vinet, P., Ferrante, J., Smith, J., Rose, J., 1986. A universal equation of state for solids. *Journal of Physics C: Solid State Physics* L467–L73.
- Vinet, P., Rose, J., Ferrante, J., Smith, J., 1989. Universal features of the equation of state of solids. *J Phys: Condens Matter.* 1, 1941–63.
- Vohra, Y., Spencer, P., 2001. Novel γ -Phase of Titanium Metal at Megabar Pressures. *Physical Review Letters* 86, 3068–3071.
- Wallace, D., 1997. Statistical mechanics of monatomic liquids. *PhRvE.* 56, 4179.

- Walsh, J., Rice, M., McQueen, R., Yarger, F., 1957. Shock-wave compressions of twenty-seven metals. *PhRv.* 108, 196–216.
- Wang, K., Reeber, R., 1998. The role of defects on thermophysical properties: thermal expansion of V, Nb, Ta, Mo and W. *Materials Science and Engineering: R: Reports* 23, 101–37.
- Wang, Y., Zhang, J., Xu, H., Lin, Z., Daemen, L., Zhao, Y., 2009. Thermal equation of state of copper studied by high PT synchrotron x-ray diffraction. *Appl Phys Lett.* 94, 071904.
- Waseda, Y., Hirata, K., Ohtani, M., 1975. High-Temperature Thermal Expansion of Pt, Ta, Mo and W Measured by X-Ray Diffraction. *High Temperatures - High Pressures* 7, 221–6.
- Weinberger, M., Tolbert, S., Kavner, A., 2008. Osmium Metal Studied under High Pressure and Nonhydrostatic Stress. *Physical Review Letters* 100, 1–4.
- Weinmann, C., Steinemann, S., 1974. Lattice and electronic contributions to the elastic constants of palladium. *Solid State Commun.* 15, 281–5.
- Westlake, D., Ockers, S., 1970. Thermal expansion of vanadium and vanadium hydride at low temperature. *Journal of the Less Common Metals* 22, 225–30.
- White, G., Colloco, S., 1984. Heat Capacity of Reference Materials: Cu and W. *J Phys Chem Ref Data* 13.
- White, G.K., 1993. Solids: thermal expansion and contraction. *Contemporary Physics* 34, 193–204.
- Wojdyr, M., 2010. Fityk: a general-purpose peak fitting program. *Journal of Applied Crystallography* 43, 1126–1128.
- Xi, F., Cai, L., 2008. Theoretical study of melting curves on Ta, Mo, and W at high pressures. *Physica B: Condensed Matter* 403, 2065–70.
- Xia, H., Duclos, S.J., Ruoa, A.L., Vohra, Y.K., 1990. New High-Pressure Phase Transition in Zirconium Metal. *Physical Review Letters* 64, 204–207.
- Xia, H., Parthasarathy, G., Luo, H., Vohra, Y.K., Ruoff, A.L., 1990. Crystal structures of group IVa metals at ultrahigh pressures. *Physical Review B* 42, 6736–6738.
- Xiang, S., Cai, L., Bi, Y., Jing, F., Wang, S., 2005. Thermal equation of state for Pt. *PhRvB* 72, 184102.

- Xiu-Lu, Z., 2008. Melting Behaviour of Mo by Shock Wave Experiment. Chinese Physics Letters 25, 2969.
- Yamanaka, S., 2004. Thermophysical properties of SrHfO₃ and SrRuO₃. Journal of Solid State Chemistry 177, 3484–3489.
- Zha, C., Mibe, K., Bassett, W., Tschauner, O., Mao, H., Hemley, R., 2008. PVT equation of state of platinum to 80 GPa and 1900 K from internal resistive heating/x-ray diffraction measurements. Zha C, Mibe K, Bassett W, Tschauner O, Mao H, Hemley R 103, 4908.
- Zhang, J., Zhao, Y., Hixson, R.S., Iii, G.T.G., Wang, L., 2008. Thermal equations of state for titanium obtained by high pressure-temperature diffraction studies. Physicsl Review B 78, 054119.
- Zhang, J., Zhao, Y., Pantea, C., Qian, J., Daemen, L., Rigg, P., Hixson, R., Greeff, C., Grayiii, G., Yang, Y., 2005. Experimental constraints on the phase diagram of elemental zirconium. Journal of Physics and Chemistry of Solids 66, 1213–1219.
- Zhang, X., Liu, Z., Gu, Y., Cai, L., Jing, F., 2008. Temperature in molybdenum at high shock pressure: Experiment and theory. Physica B: Condensed Matter 403, 3261–5.
- Zhao, Y., Zhang, J., Pantea, C., Qian, J., Daemen, L., Rigg, P., Hixson, R., Gray, G., Yang, Y., Wang, L., Wang, Y., Uchida, T., 2005. Thermal equations of state of the α , β , and ω phases of zirconium. Physical Review B 71, 184119.

VITA

ROSTISLAV HRUBIAK

July 6, 1984 Born, Lviv, Ukraine

2002-2007 B.S., Electrical Engineering
Minor: Mathematics
Florida International University
Miami, Florida

2007-2012 Doctoral Candidate
Florida International University
Miami, Florida

Teaching Assistant
Mechanical and Materials Department

PUBLICATIONS

A. Duzynska, **R. Hrubia**k, V. Drozd, H. Teisseyre, W. Paszkowicz, A. Reszka, A. Kaminska, A. Durygin, S. Saxena, J.D. Fidelus, J. Grabis, C.J. Monty, A. Suchocki. (2012) The high-pressure structural properties of ZnO bulk and nano crystals. High Pressure Research: An International Journal.

R. Hrubiak, V. Drozd, Ali Karbasi, and S. K. Saxena. (2012) High P - T structure and P - V - T equation of state of Hafnium Journal of Applied Physics (111), 112612.

A. Karbasi, S. K. Saxena, **R. Hrubia**k. (2011) Thermodynamics of several elements at high pressures. CALPHAD: Computer Coupling of Phase Diagrams and Thermochemistry (35), 72-81.

L. George, **R. Hrubia**k, K. Rajan, S. K. Saxena. (2009) Principal component analysis on properties of binary and ternary hydrides and a comparison of metal versus metal hydride properties. Journal of Alloys and Compounds (478), 731-735.

R. Hrubiak, L. George, S. K. Saxena, K. Rajan. (2009) A Materials Database for Exploring Material Properties, Journal of Materials (JOM) (61), 59-62.